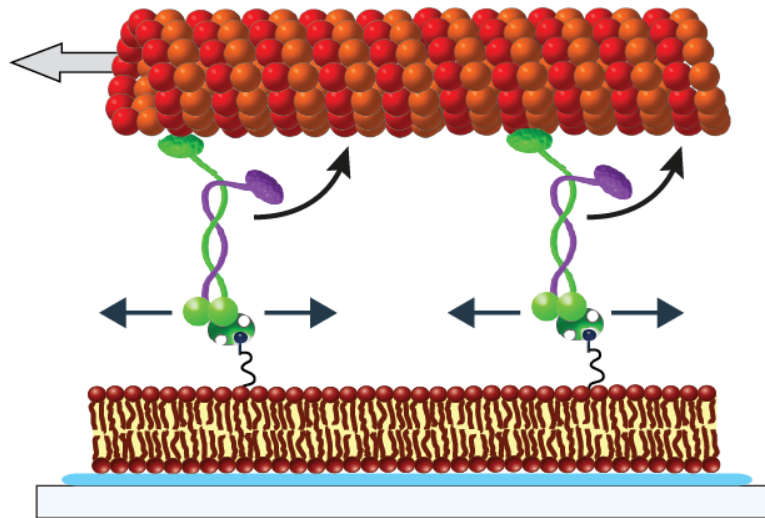


Transport by kinesin motors diffusing on a lipid bilayer



DISSERTATION

Submitted for the degree of

Doctor of Philosophy
(Ph. D.)

at the

Fakultät für Mathematik und Naturwissenschaften
Technische Universität Dresden

by

Rahul Grover
born on 24th April 1986

Thesis Submission: 23rd July 2015
Thesis Defense: 25th November 2015

List of reviewers:

Prof. Dr. Stefan Diez

B CUBE – Center for Molecular Bioengineering, Technische Universität Dresden,
Arnoldstraße 18, 01307 Dresden

Prof. Dr. Petra Schwille

Max Planck Institute of Biochemistry, Department of Cellular and Molecular
Biophysics, Am Klopferspitz 18, 82152, Martinsried

Doctoral Commission members:

Prof. Dr. Christian Dahmann

Prof. Dr. Anthony Hyman

Prof. Dr. Stephan Grill

Prof. Dr. Stefan Diez



The work described in this thesis was performed at the Max Planck Institute of Molecular Cell Biology and Genetics, Pfotenhauerstraße 108, and the B CUBE – Center for Molecular Bioengineering, Technische Universität Dresden, Arnoldstraße 18, both in 01307 Dresden, Germany.

Erklärung entsprechend §5.5 der Promotionsordnung

Hiermit versichere ich, dass ich die vorliegende Arbeit ohne unzulässige Hilfe Dritter und ohne Benutzung anderer als der angegebenen Hilfsmittel angefertigt habe; die aus fremden Quellen direkt oder indirekt übernommenen Gedanken sind als solche kenntlich gemacht. Die Arbeit wurde bisher weder im Inland noch im Ausland in gleicher oder ähnlicher Form einer anderen Prüfungsbehörde vorgelegt.

Die Dissertation wurde im Zeitraum vom 1st July 2011 bis 1st July 2015 verfasst und von Prof. Dr. Stefan Diez am B CUBE – Center for Molecular Bioengineering der Technischen Universität Dresden betreut.

Meine Person betreffend erkläre ich hiermit, dass keine früheren erfolglosen Promotionsverfahren stattgefunden haben.

Ich erkenne die Promotionsordnung der Fakultät für Mathematik und Naturwissenschaften, Technische Universität Dresden an.

Rahul Grover
Dresden 22nd July 2015

In loving memory of my grandmother, Smt. Ganga Devi, a kind-
hearted soul who always believed in me

"Measure what is measurable, and make measurable what is not so."
Galileo Galilei

Abstract

Intracellular transport of membrane-bound vesicles and organelles is a process fundamental for many cellular functions including cell morphogenesis and signaling. The transport is mediated by ensembles of motor proteins, such as kinesins, walking on microtubule tracks. When transporting membrane-bound cargo inside a cell, the motors are linked to diffusive lipid bilayers either directly or via adaptor molecules. The fluidity of the lipid bilayers induces loose inter-motor coupling which is likely to impact the collective motor dynamics and may induce cooperativity. Here, we investigate the influence of loose coupling of kinesin motors on its transport characteristics.

In the first part of this thesis, we used truncated kinesin-1 motors with a streptavidin-binding-peptide (SBP) tag and performed gliding motility assays on streptavidin-loaded biotinylated supported lipid bilayers (SLBs), so called 'membrane-anchored' gliding motility assays. We show that the membrane-anchored motors act cooperatively; the microtubule gliding velocity increases with increasing motor density. This is in contrast to the transport behavior of multiple motors rigidly bound to a substrate. There, the motility is either insensitive to the motor density or shows negative interference at higher motor density, depending on the structure of the motors.

The cooperativity in transport driven by membrane-anchored motors can be explained as following: while stepping on a microtubule, membrane-anchored motors slip backwards in the viscous membrane, thus propelling the microtubule in the solution at a velocity, given by the difference of the motor stepping velocity and the slipping velocity. The motor stepping on the microtubule occurs at maximal stepping velocity because the load on the membrane-anchored motors is minute. Thus, the slipping velocity of membrane-anchored motors determines the microtubule gliding velocity. At steady state, the drag force on the microtubule in the solution is equal to the collective drag force on the membrane-anchored motors slipping in the viscous membrane. As a consequence, at low motor density, membrane-anchored motors slip back faster to balance the drag force of the microtubule in the solution. This results in a microtubule gliding velocity significantly lower than the maximal stepping velocity of the individual motors. In contrast, at high motor density, the microtubules are propelled faster with velocities equal to the maximal stepping velocity of individual motors. Because, in this case, the collective drag force on the motors even at very low slipping velocity, is large enough to balance the microtubule drag in the solution. The theoretical model developed based on this explanation is in good agreement with the experimental data of gliding velocities

at different motor densities. The model gives information about the distance that the diffusing motors can isotropically reach to bind to a microtubule, which for membrane-anchored kinesin-1 is $\sim 0.3 \mu\text{m}$, an order of magnitude higher as compared to rigidly bound motors, owing to the lateral mobility of motors on the membrane. In addition, the model can be used to predict the number of motors involved in transport of a microtubule based on its gliding velocity.

In the second part of the thesis, we investigated the effect of loose inter-motor coupling on the transport behavior of KIF16B, a recently discovered kinesin motor with an inherent lipid-binding domain. Recent studies based on cell biological and cell extract experiments, have postulated that cargo binding of KIF16B is required to activate and dimerize the motor, making it a superprocessive motor. Here, we demonstrate that recombinant full-length KIF16B is a dimer even in the absence of cargo or additional proteins. The KIF16B dimers are active and processive, which demonstrates that the motors are not auto-inhibited in our experiments. Thus, in cells and cell extracts Kif16B may be inhibited by additional factors, which are removed upon cargo binding. Single molecule analysis of KIF16B-GFP reveals that the motors are not superprocessive but exhibit a processivity similar to kinesin-1 indicating that additional factors are most likely necessary to achieve superprocessivity. Transport on membrane-anchored KIF16B motors exhibited a similar cooperative behavior as membrane-anchored kinesin-1 where the microtubule gliding velocity increased with increasing motor density.

Taken together, our results demonstrate that the loose coupling of motors via lipid bilayers provides flexibility to cytoskeletal transport systems and induces cooperativity in multi-motor transport. Moreover, our 'membrane-anchored' gliding motility assays can be used to study the effects of lipid diffusivity (e.g. the presence of lipid micro-domains and rafts), lipid composition, and adaptor proteins on the collective dynamics of different motors.

Contents

Abstract.....	vii
1 Introduction	1
1.1 Intracellular transport driven by motor proteins.....	2
1.2 Attachment of motor proteins to cargo.....	13
1.3 <i>In vitro</i> approaches to study transport by motor proteins.....	16
1.4 Aim of this study.....	23
2 Transport by kinesin-1 anchored to supported lipid bilayers ...	24
2.1 Formation and characterization of biotinylated SLBs.....	26
2.2 Anchoring kinesin-1 to biotinylated SLBs.....	28
2.3 Gliding motility of microtubules by kinesin-1 linked to SLBs	34
2.4 Theoretical description of gliding motility on diffusing motor proteins..	40
2.5 Comparison of the gliding velocity between experiment and theory	46
2.6 Gliding motility on phase-separated SLBs	53
2.7 Discussion.....	55
3 Transport by KIF16B with an inherent lipid-binding domain	62
3.1 Expression and purification of KIF16B.....	63
3.2 Biophysical characterization of KIF16B	70
3.3 Gliding motility of microtubules by KIF16B linked to SLBs	78
3.4 Transport of SUVs and lipid-coated beads attached to KIF16B	87
3.5 Discussion.....	90
4 Conclusion and outlook.....	96
5 Materials and methods	99
5.1 Reagents and solutions	99
5.2 Molecular biology	100
5.3 Protein expression and purification.....	104
5.4 <i>In vitro</i> motility assays.....	110
5.5 Image acquisition and data analysis	118
References.....	126
List of figures.....	141

List of tables	143
Abbreviations and symbols	144
Acknowledgements	147

1 Introduction

Motion is a fundamental characteristic of life, encompassing movement of cells in their environment to find and absorb resources, and movement within a cell for effective distribution of the resources and removal of waste. For cells to grow, multiply and adapt to its environment, essential components such as lipids, proteins, carbohydrates and mRNAs, have to be continuously transported within and outside a cell. Prokaryotic cells, which are small and lack membranous compartments, can easily transport materials within a cell by diffusion, where the molecules are driven due to thermal agitation from areas of high concentration to areas of low concentration. The distance moved by a molecule due to diffusion depends on its size, the viscosity of the fluid, and the temperature. On an average a protein with a size of ~ 100 kDa (~ 3 nm radius) will only take half a second to travel $10\ \mu\text{m}$ in aqueous environment. Thus transport by diffusion is fast enough to distribute substances in small cells (Howard, 2001). However, this transport mechanism would be slow if the proteins or large complexes such as organelles ($\sim 1\ \mu\text{m}$) have to move longer distances in a viscous environment, and inefficient if the molecules have to be directed to specific locations, as is the case in a eukaryotic cell.

Eukaryotic cells are relatively big and complex containing numerous membrane-bound organelles such as the nucleus, endoplasmic reticulum (ER), Golgi apparatus, mitochondria etc. all of which fulfill distinct specialized functions and thus have different lipid composition and proteins. Continuous transfer of proteins, lipids and other molecules from one compartment to the other as well as plasma membrane is necessary, to maintain cell's structural and functional organization. At the same, the composition of various organelles has to be maintained for its functionality. Therefore, the exchange of materials is tightly regulated to ensure that the flow of membrane between compartments is balanced and selected proteins are brought back to the compartment of origin. The selective exchange of materials is accomplished by means of two complementary process, exocytosis or secretory pathways and endocytosis, in a

cell. Exocytosis is a process through which the newly synthesized proteins and lipids formed in the cell interior are delivered to different organelles and plasma membrane. Conversely, through the process of endocytosis cell takes up material from the environment and plasma membrane and deliver it to the different parts of the cell (Alberts et al., 2002). Both these processes involve segregating different membrane components and soluble molecules, referred to as cargo into functionally distinct membrane-enclosed compartments referred to as transport vesicles reviewed in (Gundelfinger et al., 2003; Haucke et al., 2011). These transport vesicles then move to specific locations in a cell where they unload their cargo. In recent years, advances in molecular genetics, biochemical analysis, electron microscopy and fluorescence imaging have enabled us to identify multitude of components involved in the complex biological process of vesicular trafficking. However, significant progress is still to be made in correlating the function of different components and understanding of molecular mechanism involved in formation of vesicles, sorting of cargo, and their delivery. In the following section few of the key components involved in intracellular transport and the approaches to study their molecular mechanisms are detailed.

1.1 Intracellular transport driven by motor proteins

The transport vesicles, which can have spherical or large irregular geometry, have to be transported in a crowded gel-like cytoplasm of a eukaryotic cell. Furthermore, they have to cover great distance in certain cells such as neurons, which can be several tens of centimeters long. These factors severely restrict the diffusion transport mechanism; therefore for fast and efficient transport of cargo in a bi-directional manner between different organelles, eukaryotic cells have evolved complex transport machinery for the inter-compartmental communications. Transport inside a cell, similar to physical world, requires extensive network of tracks on which a cargo can be carried from one location to another. Inside a cell the transportation network is composed of two classes of cytoskeletal filaments comprising of actin filaments and microtubules (fig. 1.1). The cytoskeletal filaments are composed of smaller protein subunits, which associate non-covalently to form higher order polar structures inside a cell. The

cytoskeletal filaments are highly dynamic, which assemble and disassemble with in a cytoplasm on a time scale of seconds to minutes and the kinetics of assembly is regulated by a large variety of associated proteins (Desai et al., 1997).

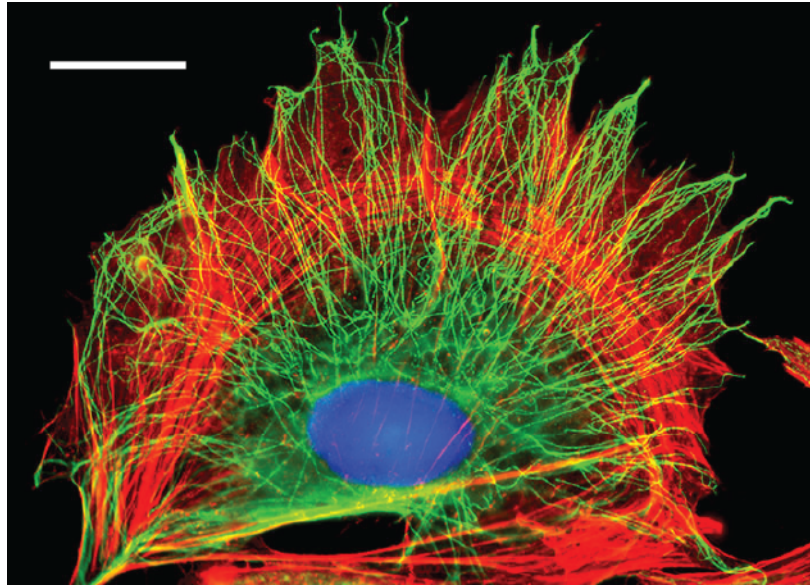


Figure 1.1 | Cytoskeletal network in eukaryotic cell. In the cultured hamster kidney cell two classes of cytoskeletal filaments are shown, actin (red) and microtubules (green). The DNA in the nucleus is labeled in blue. Scale bar: 10 μm . Adapted from (Alberts et al., 2002)

The vesicular cargo moves on a highly organized and directed routes formed by the cytoskeletal filaments. The transport is mediated by a special class of force generating enzymes called as 'motor proteins'. These fascinating molecular machines convert the chemical energy of adenosine-5'-triphosphate (ATP) into mechanical work, thereby generating motion. Over time molecular motors have evolved and diverged into repertoire of motor proteins classified into three families myosin, dynein and kinesin which differ in the type of filament they bind to, the direction in which they move along the filament and the cargo that they carry reviewed in (Vale, 2003). Myosin superfamily is large and diverse family of molecular motors (17 classes identified so far), which associate and move along actin filaments. They are present in almost all the eukaryotic cells and are involved in muscular contraction, cytokinesis, short-range vesicular transport and host of other cell processes reviewed in (Hartman et al., 2012). Motor proteins of dynein and kinesin superfamily binds and move along microtubules.

Dynein is divided into three major classes axonemal dyneins, which power the beating of cilia and flagella; interflagellar transport dyneins, which transport protein in axonemes; and cytoplasmic dynein, which the primary motor protein involved in retrograde transport (from cell boundary to cell interior) of cargo inside a cell (A. Carter et al., 2011), reviewed in (Roberts et al., 2013).

The work in this thesis focuses on microtubule-based transport by kinesin motor proteins thus in the following section an overview of microtubules and kinesin motor proteins is presented.

Microtubules

Microtubules are one of the key structural elements of eukaryotic cells, which provide mechanical strength to maintain and adapt the cell shape, depending on the cell's environment. Microtubules along with associated proteins such as motor proteins play a critical role in the spatio-temporal organization of various organelles during the cell cycle for example correct positioning of nucleus, and localization and dispersion of Golgi complex. In addition, they provide the tracks for molecular motors for intracellular transport.

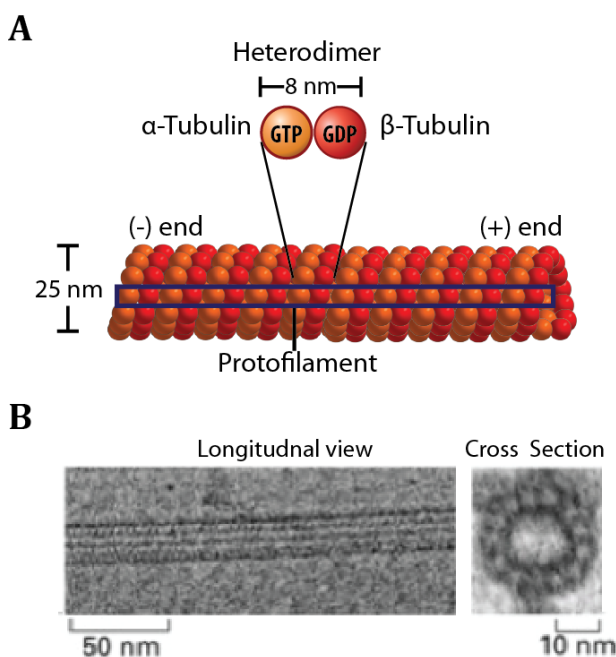


Figure 1.2 | Structure of a microtubule. A) Microtubules are composed of α/β -tubulin heterodimer subunits, size 8 nm, and the asymmetry of subunits give MT polarity. Several subunits are linked head to tail to organize into linear protofilaments. Thirteen linear protofilaments associate laterally to form a hollow cylindrical polymer of diameter 25 nm. A subunit and a protofilament are highlighted. Adapted from (Lodish et al., 2000) B) Electron micrographs showing longitudinal and cross sectional view of a microtubule. Adapted from (Alberts et al., 2002)

Microtubule polymers are composed of α and β -tubulin heterodimer subunits, which are attached non-covalently. The monomers are structurally similar with molecular weight 55 kDa and bind to one (guanosine-5'-triphosphate) GTP molecule. The GTP bound to α subunit is trapped at the interface and is never hydrolyzed, whereas the GTP bound to β -tubulin can be hydrolyzed and exchanged. These subunits attach in head to tail manner to form a protofilament. The protofilaments then associate laterally to form a sheet that closes to form a hollow cylindrical polymer with a diameter of 25 nm (fig. 1.2) (Desai et al., 1997). This structure allows the heterodimers to generate two new types of protein-protein interaction; the β -tubulin of a heterodimer interacts with the α tubulin of another heterodimer longitudinally and the lateral interaction between the heterodimers of neighboring protofilaments. As a consequence, the microtubules are stiff polymers with a persistence length of several millimeters (van Mameren et al., 2009). *In vivo* a typical microtubule is made of 13 protofilaments, which run parallel to the longitudinal axis. However, when formed *in vitro* the number of protofilament can vary from 9 to 17 (Wade et al., 1990).

Microtubules have a distinct structural polarity owing to the heterogeneous subunits arranging in head to tail manner to form a protofilament which associate parallel to each other. This polarity has profound effect on microtubule growth, where the subunits attach and dissociate faster at one end as compared to the other end. The more dynamic end of a microtubule is called the plus end and the other end is called the minus end. On a microtubule, β -tubulin monomer points toward the plus end and the α -tubulin towards the minus end. Inside cell microtubules originate from microtubule organizing centers (MTOC) typically localized at the center, where they self-organize into radial array protruding outwards from the center. The minus end is docked at the MTOC and the plus end points towards the cell boundary. The structural asymmetry of the microtubules is utilized by the motor proteins for directed movement.

Free tubulin heterodimers have β -tubulin bound to GTP, which upon attachment of another subunit is hydrolyzed over time. Therefore the microtubules are

composed mainly of guanosine-5'-diphosphate (GDP) β -tubulin, with a small cap of GTP at the growing end. The conformation of heterodimers when β -tubulin is bound to GTP is straight whereas GDP dimers have bent conformation reviewed in (Nogales et al., 2006).

The GTP cap at the end stabilizes the structure of microtubule and favors the growth of microtubule (Drechsel et al., 1994; Caplow et al., 1996). However, when free GTP- β -tubulin heterodimers are not available in sufficient concentration for growth, the GTP cap is lost owing to hydrolyzation of GTP- β -tubulin. This leads to switch from slow growth to rapid shrinkage referred to as 'catastrophe'. However, a depolymerizing microtubule can re-enter the growth phase, referred to as 'rescue' once the local free GTP- β -tubulin concentration is high enough to initialize growth. This transition of microtubule between slow growth and rapid shrinkage of a microtubule is termed as dynamic instability. The structural bases of microtubule dynamics have been revealed by cryoelectron microscopy showing that the polymerizing microtubule plus-ends adopts sheet like structure while depolymerizing plus-ends have curled peeling off protofilaments (Chrétien et al., 1995). The dynamic instability allows the rapid restructuring of the microtubule architecture inside the cell allowing them to generate pushing and pulling forces which facilitates critical functions such as segregation of chromosomes and remodeling cell shape in response to external environment reviewed in (Brouhard, 2015). However, for the *in vitro* motility assays (see chapter 1, page 16) stable and static microtubules are required, thus the dynamic instability is inhibited by growing microtubules in guanosine 5'-[α,β -methylene] triphosphate (GMP-CPP), a slowly hydrolyzable analog of GTP or by addition of cytostatic drugs, such as taxol (Schiff et al., 1979).

In summary, microtubules are stiff polar cytoskeleton filaments, which are made up of smaller protein subunits providing rigidity and stability to the cell. In addition they self organize to form cellular tracks for intracellular transport of cargo, mediated by motor proteins such as kinesins.

Kinesin superfamily

Kinesin was discovered in 1985 based on the motility of organelles observed in the giant axon of the squid (R. D. Allen et al., 1982; Brady, 1985; Vale et al., 1985). In the last 30 years advances in genetics, biological screening and bioinformatics have led to the discovery of a huge number of new kinesins genes in a variety of organisms. Currently, more than 600 kinesin sequences have been identified ranging across different species, out of which 45 genes are found in humans (Miki et al., 2001, 2005). At present, the kinesin superfamily, also referred to as KIFs, is divided into 14 sub families based on the phylogenetic analysis, where structurally and functionally related members in different cells or organisms are grouped together (fig. 1.3). The 14 subfamilies of Kinesin can be broadly grouped into three types, depending on the position of motor domain in the amino acid sequence of the proteins: First, N-kinesins, which have motor domain at the N-terminal region, this include all kinesin families except 13 and 14, they walk towards the plus-end of a microtubule. Second, M-kinesins, which have motor domain in the middle, kinesin subfamily 13 belongs to this class. Third, C-kinesins, which have motors domain at the C-terminal, kinesin subfamily 14 belongs to this class and they move towards the minus-end of the microtubule.

Kinesin superfamily members, as one of the key force producing enzymes, perform a wide range of functions essential for sustaining cell functionality and morphology. First, they are the primary motor proteins involved in the anterograde transport (from cell center to cell boundaries) of the organelles, vesicles and protein complexes inside different cells such as neurons, epithelial cells and fibroblasts. About half of the kinesin motors identified in humans have intracellular transport as their major function. For example kinesin-1 move on microtubule in neuronal axons to transport synaptic vesicles and mitochondria, and in non-neuronal cells to transport late endosome, lysosome, and Golgi-ER vesicles. Similarly, kinesin-3 members such as KIF16B are involved in the transport of early endosomes reviewed in (Hirokawa, 1998; Vale et al., 2003; Hirokawa et al., 2009).

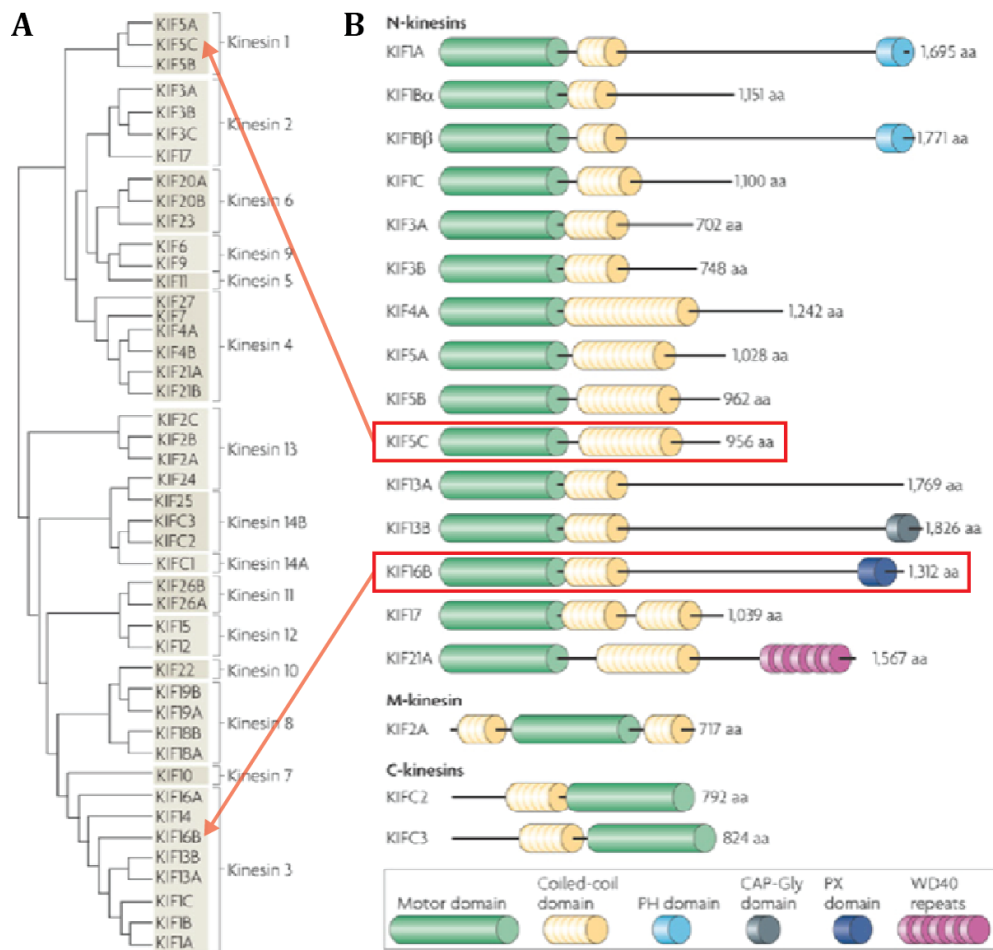


Figure 1.3 | Kinesin superfamily, structure and phylogeny of major mammalian kinesin. A) A phylogenetic tree of all 45 kinesin superfamily (also known as KIF) genes in the mouse genome, which are classified into 14 families. B) The domain structure of the major kinesins. In general, kinesins comprise a kinesin motor domain and a coiled-coil domain. There are also gene specific domains, such as the PH domain of KIF1A and KIF1 β , the CAP-Gly domain (a conserved, Gly-rich domain of cytoskeleton-associated proteins) of KIF13B, the WD40 repeats of KIF21A and PX domain of KIF16B. The 14 families of kinesins can be broadly grouped into N-kinesins, M-kinesins and C-kinesins, which contain their motor domain at the amino terminus, in the middle or at the carboxyl terminus, respectively. KIF5C and KIF16B motors are studied in this thesis, marked with red box. Adapted from (Hirokawa et al., 2009)

Second, they perform essential role in the chromosome transport and spindle formation during cell division reviewed in (Sharp et al., 2000a, 2000b). Members of kinesin sub-families 5, 6 and 14 are involved in sliding and crosslinking of microtubules in different zones of the mitotic spindle, whereas kinesin-7 and kinesin-4 members mediate spindle formation through binding to chromosomes. Third, they play a crucial role in the microtubule dynamics by regulating

assembly and disassembly kinetics, either stabilizing or destabilizing microtubules thus influencing the spindle formation and disassembly reviewed in (Endow et al., 2010; X. Su et al., 2012; Walczak et al., 2013).

All the members of kinesin superfamily share a conserved catalytic core, which hydrolyze ATP, referred to as 'motor domain'. The other domains are diversified based on the unique cellular functions, as detailed above, for different kinesin members. In this study, we investigate the transport characteristic of kinesin-1 member KIF5C and kinesin-3 member KIF16B, hence their structure are described in the following section.

Kinesin-1

Kinesin-1 is a heterotetramer composed of two identical heavy chains (~120 kDa) and light chains (~60 kDa). The kinesin heavy chain (KHC) dimers consist of three different domains: (i) two motor domains at N-terminal also called 'heads' which are connected via a short 'neck linker' (14 a.a) to (ii) the elongated coiled-coil (CC) domains called 'stalk' followed by (iii) two globular domains at the C-terminal called 'tail' (fig. 1.4). The head of the motor protein is large globular domain containing ATP binding pocket as well as microtubule binding site. The neck linker is a flexible region that changes its confirmation upon binding and hydrolysis of ATP. The elongated coiled-coil is required to keep the motors in dimeric state. The tail functions as cargo binding domain and associate with the kinesin light chain (KLC) dimers. It also plays a major role in regulating the motility of kinesin-1, when not bound to cargo (Vale, 2003). It is necessary that kinesin-1 motors are inactive when not bound to cargo, to prevent squandering of ATP. This is achieved by folding back of tail domain to bind to motor head (Coy et al., 1999). The tail domain cross-links both the motor heads, such that their movement is severely restricted due crosslinking at two positions, coiled-coil stalk and tail-motor head interface. This prevents the release of ADP from the binding pocket of the motor head, hence the ATPase activity and the motility is restricted (Kaan et al., 2011).

KLCs also contain three domains (i) N-terminal CC domain (ii) a tetratricopeptide repeat (TPR), and (iii) C-terminal domain. The N-terminal CC

domain is conserved and binds to KHC. The latter two domains are involved in protein-protein interaction and are proposed to interact with the receptor proteins present on cargo and thus providing a physical link between the KHC and cargo (Gunawardena et al., 2004; Zhu et al., 2012). Four different isoforms of KLC are present in humans KLC1-4. Recent studies demonstrate that KLC isoforms interact with different proteins such as jun-kinase interacting proteins (JIPs)(Verhey et al., 2001), and the amyloid precursor protein (APP) on the synaptic vesicles (Kamal et al., 2000). However, the distinctions between different isoforms, their binding partners and specific cargo to which they attach still need to be discovered and understood.

Three KHC genes present in humans along with four different isoforms of KLCs provide different permutation for 'conventional kinesin' to bind to specific cargos either via their tail domain or KLC domains.

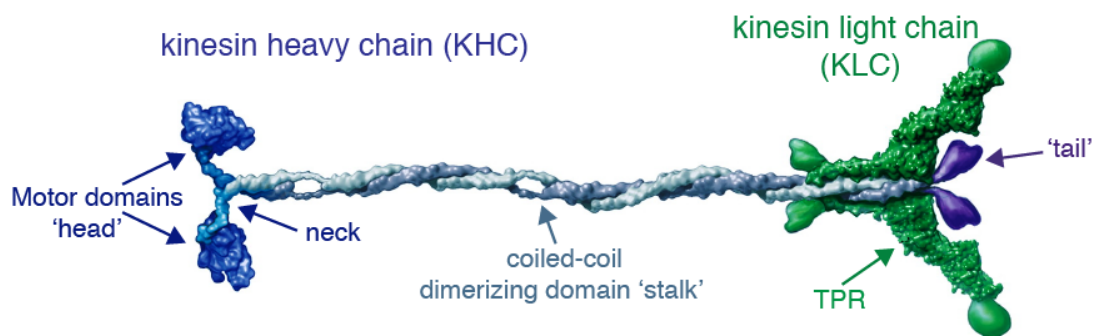


Figure 1.4 | Structure of kinesin-1 dimer. Kinesin-1 is a heterotetramer composed of two identical heavy chains KHC consisting of three domains – head, stalk and tail and light chains KLC consisting of coiled coil at N and C terminal, with tetratricopeptide repeat (TPR) motifs in middle. Adapted from (Vale, 2003)

Kinesin-3

The kinesin-3 family was first identified in a mutant screen in *C. elegans* where null mutations in UNC-104 gene caused severe defect in axonal transport of synaptic vesicles (Hall et al., 1991). This was soon followed by the discovery of the mouse homolog KIF1A (Yonekawa et al., 1998). Currently, the kinesin-3 subfamily is one of the largest among the kinesin superfamily and consists of five different KIFs (KIF1, KIF13, KIF14, KIF16, and KIF28). Kinesin-3 motors are involved in transport of endosomes, lysosomes, mitochondria and synaptic vesicles. Kinesin-3 family members have two class conserved features (i) conserved insert in loop 12 of motor domain. This insert contains a number of charged lysine residues and is therefore referred to as 'K-loop' (Okada et al., 2000) (ii) Fork head homology (FHA) domain which have been shown to recognize phosphothreonine epitopes on proteins, and thus might be involved in protein-protein interactions regulated by phosphorylation but their function in the motor protein is not very well understood (Westerholm-Parvinen et al., 2000; Durocher et al., 2002). The C-terminal of a few kinesin-3 family members contains a lipid-binding domain for example KIF1A and KIF1B have a pleckstrin homology (PH) domain and KIF16B has a phox homology (PX) domain.

Kinesin-3 family members are referred to as 'monomeric' kinesins, as they lack substantial coiled-coil regions in their structure. The initial characterization of KIF1A, the founding member of this family, suggested that it is a globular monomeric protein (fig. 1.5A), which transport synaptic vesicles towards the plus-end of a microtubule with a velocity of 1.2 $\mu\text{m/s}$ (Okada et al., 1995). However, more recently the oligomeric state of different kinesin-3 subfamily members has been a topic of debate. KIF1A and various other members of kinesin-3 family such as HsKIF13B, HsKIF1C, and DmKin73 have been shown to exist in dimeric state in cells (Dorner et al., 1999; Hammond et al., 2009; Huckaba et al., 2011).

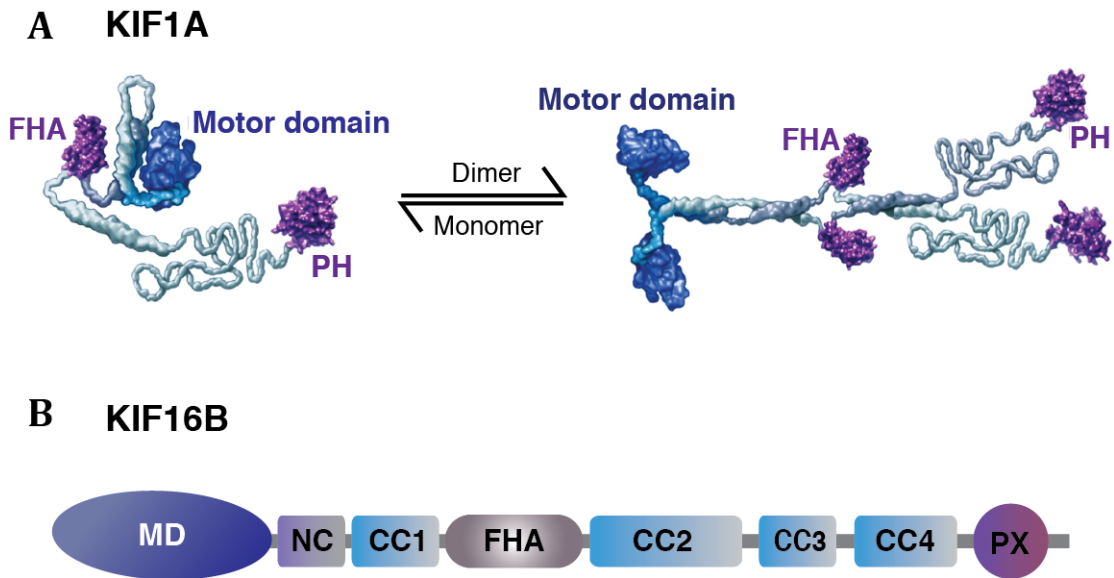


Figure 1.5 | Structure of kinesin-3 member, KIF1A and KIF16B. A) KIF1A is monomeric globular protein in solution with N-terminal motor domain (MD), forkhead-associated (FHA) domain and lipid-binding plekstrin homology (PH) domain at C-terminal. KIF1A might dimerize reversibly *in vivo* in a concentration-dependent manner. The mechanism of dimerization is not clear, to date. Adapted from (Vale, 2003) B) Schematic of the domain organization of KIF16B, which consist of N-terminal MD, followed by neck-coil (NC), coiled-coil 1 (CC1), FHA domain and three CC with C-terminal lipid-binding phox homology (PX) domain at c-terminal. Adapted from (Soppina et al., 2014)

KIF16B, a recently discovered motor protein through genomic screening, is classified in kinesin-3 subfamily among 14 kinesin motor families. It displays two characteristic properties of kinesin-3 K-loop and FHA domain in its stalk. It consists of 1318 amino acid residues with a molecular weight of 152 K.Da and has a lipid-binding domain at the C-terminal PX domain (fig. 1.5B). KIF16B is present in various organs in a human body e.g. brain, kidney, liver, intestine, placenta, leukocytes, heart and skeletal muscle (Hoepfner et al., 2005). KIF16B walks towards the plus-end of microtubule and is the primary motor employed for transport of early endosomes and its localization to somatodendritic region of neurons (Farkhondeh et al., 2015). KIF16B regulates the transport of different receptors such as EGF-receptors, FGF-receptors, transferrin receptors by controlling the localization and functions of early endosomes (Ueno et al., 2011; Skjeldal et al., 2012; Perez Bay et al., 2013).

1.2 Attachment of motor proteins to cargo

The function of many kinesin motors has been elucidated over the past several years, but the identity of membranous cargo carried by each motor and the characteristics of motor-cargo interaction are still poorly understood. In most of the cases, the interactions are composed of three players – the motor proteins, a cargo bound receptor and accessory components such as scaffolding proteins. Cargo interactions with motors, therefore, involve large multi-protein complexes including cargo specific Rab GTPases, a family of monomeric G proteins (guanine-nucleotide-binding proteins), which associate with various adaptor proteins to recruit motors to their specific cargo. Current knowledge of the different cargo transported by various motors and their specific binding partners have been summarized in a few excellent reviews (Gunawardena et al., 2004; Hirokawa et al., 2009; Akhmanova et al., 2010; Fu et al., 2014; Granger et al., 2014). Here, a brief overview of cargo associated with kinesin-1 and kinesin-3 and the accessory factors involved is listed

Table 1.1 | Cargo complexes transported by kinesin-1 and kinesin-3.

Motor	Organelle, cargo	Binding partners		References
		Small GTPase	Adaptors or scaffolds	
Kinesin-1	Mitochondria	Miro	Milton/TRAK, RanBP2	(Glater et al., 2006; Macaskill et al., 2009)
	TrkB carriers	Rab27b	TrkB, Slp1 CRMP-2	(Arimura et al., 2009)
	APP carriers	Rab3?	KLCs, APP, JIP1	(Kamal et al., 2000; Szodorai et al., 2009)
	GABA rec. carriers		HAP1 Huntington	(Twelvetrees et al., 2010)
	Syntaxin vesicles		Synatubulin	(Q. Su et al., 2004)
	R. endosomes	Rab4/11	Gadkin-AP1	(Schmidt et al., 2009)
	ApoER2 carriers		KLCs, JIPs	(Verhey et al., 2001)
	AMPA receptors		GRIP1	(Setou et al., 2002)
Kinesin-3				
KIF13B	Vesicles	ARF6	Centaurin- α -1, PIP ₃	(Venkateswarlu et al., 2005)
KIF1A/1B β	Synaptic vesicles	Rab3	DENN/MADD	(Niwa et al., 2008)
KIF1C	Secretory vesicles	Rab6	BICDR1	(Schlager et al., 2010)
KIF16B	Early endosomes	Rab14?	PI(3)P	(Hoepfner et al., 2005; Ueno et al., 2011)

Over 20 adaptor proteins have now been identified for kinesin-1 (fig. 1.6), which recruit the motor to the specific membranous cargo (F. Sun et al., 2011). The adaptor proteins either interact directly with the KHC tail and/or with the KLC of kinesin-1 motors. The growing number of identified adaptor proteins reflects the complexity of the intracellular-transport machinery.

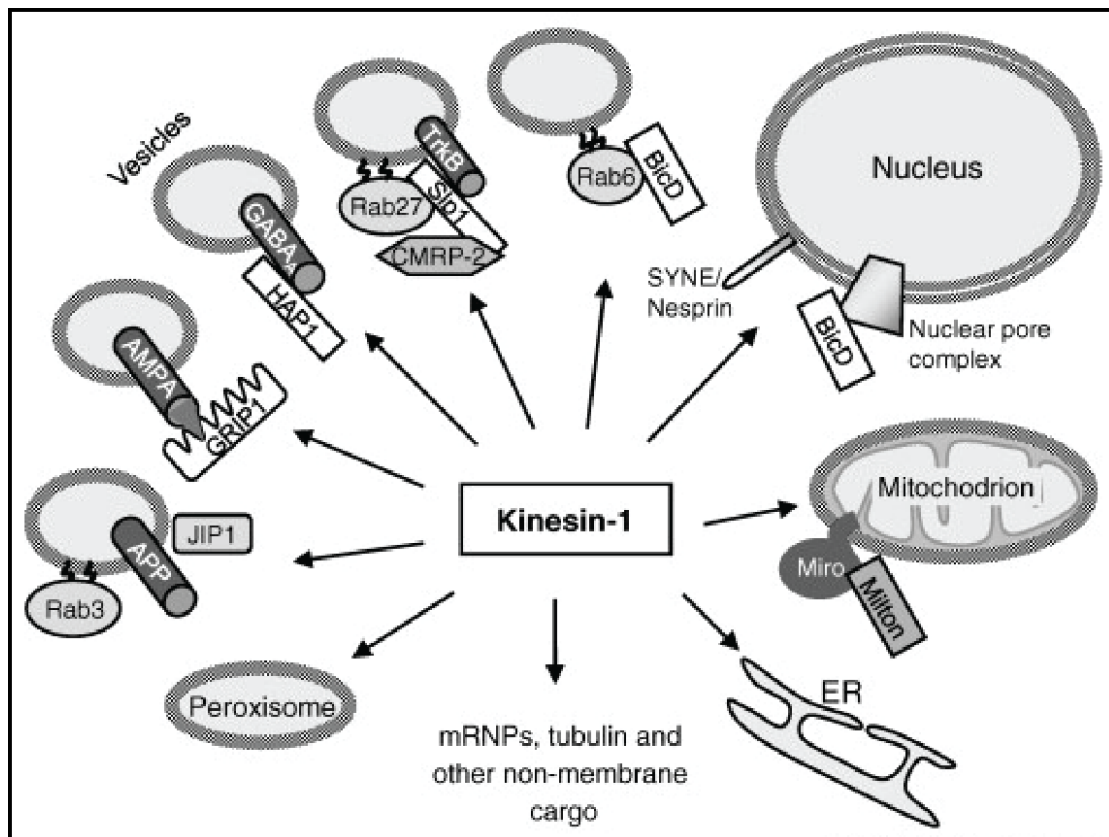


Figure 1.6 | Kinesin-1 attachment to cargo via various adaptor proteins. The scheme illustrates the multiplicity of cargoes transported by kinesin-1 in mammals. Membrane attachment often depends on lipid anchors, such as geranylgeranyl groups, which are linked to different Rabs (Rab3, Rab 27 and Rab6). Trans-membrane proteins such as the small GTPase Miro, Amyloid precursor protein (APP), and various receptors such as (α -amino-3-hydroxy-5-methyl-4-isoxazole propionic acid)-type receptors (AMPA), gamma-aminobutyric acid (GABA_A), Tropomyosin receptor kinase B (TrkB) can also serve as a part of the motor attachment complex, often in conjunction with adaptors. Kinesin-1 uses different binding sites for different cargo, with its KHC tail and KLC; adaptors such as Milton, huntingtin associated protein 1 (HAP1) and glutamate receptor-interacting protein 1 (GRIP1) interact with KHC, while others such as (JNK)-interacting proteins (JIP1) and collapsin response mediator protein 2 (CRMP-2) bind to the light chains. For some organelles, such as the ER, motor receptors still elusive. Adapted from (Akhmanova et al., 2010)

Role of lipids in motor recruitment to a cargo

Diversity in the lipid composition, of different membranous compartments of the cell, plays a crucial role in recruitment of specific motors to a cargo. Among the lipids that show significant degrees of specificity to different compartments are anionic lipids such as phosphoinositides (PIs), which are low in abundance ~1% of total cellular lipid pool (McLaughlin et al., 2005), yet play a critical role in recruitment of peripheral proteins to the membrane interface. For example phosphatidylinositol - (4,5) bis phosphate (PIP₂), is present in the cytoplasmic leaflet of the plasma membrane, and phosphatidylinositol - (3) monophosphate (PI(3)P) is present in the early endosomes and in the ER (Stahelin et al., 2014). These lipids can be recognized by special lipid-binding domains, present in the adaptor proteins or motors, for example PH domain at the tail of a few kinesin-3 family members such as KIF1A/1B and unconventional myosins such as myosin X and myosin Ic. PH domain specifically binds to the phosphoinositide PI(4,5)P₂ (Hirokawa, 1998; Berg et al., 2000; Tomishige et al., 2002; Hokanson et al., 2006). KIF16B, a kinesin-3 family member has PX domains at its tail, which have strong affinity for phosphoinositide PI(3)P (Blatner et al., 2007).

Other lipids such as cholesterol and sphingolipids, found in the Golgi complex and plasma membrane, are known to form two immiscible phases in the lipid-bilayer, liquid-ordered (L_o) domains rich in cholesterol/sphingolipids, which are densely packed resulting into low diffusivity and liquid-disordered (L_d) phase rich in unsaturated glycerolipids having higher diffusivity (Holthuis et al., 2009). These lipids can also play an important role in recruitment and segregation of motor proteins, enrichment of cholesterol in late endosome can regulate the architecture of dynein-dynactin binding complex through cholesterol sensor (Rocha et al., 2009) . Though lipids alone might not be the sole targeting factor, but they definitely have an important role in motor recruitment specificity.

Coupling motor activity with cargo binding

To avoid the useless expenditure of energy, when not bound to a cargo, motors are in an inactive state where they are self-inhibited by changing its conformation such as kinesin-1 (Coy et al., 1999; Hackney et al., 2009; Kaan et al., 2011). A self-inhibitory control mechanism has also been described for kinesin-3

motors, which involves interaction between the neck-coil (NC) and the first coiled coil (CC1) and between the FHA domain and CC2. The CC1 region folds to interact with NC region resulting in the monomeric state of KIF1A and the FHA-CC2 region prevent microtubule binding, thus inhibiting the motor activity (Lee et al., 2004; Hammond et al., 2009). A recent study has postulated the similar NC-CC1 interaction, self-inhibitory mechanism for different members of kinesin-3 such as KIF13A/B, KIF1A/B and KIF16B (Soppina et al., 2014). However, recent findings contradicting this self-inhibition mechanism have been proposed for KIF16B, which is shown to be inhibited by the interaction of its stalk with its motor domain rather than NC-CC1 interaction (Farkhondeh et al., 2015). The motor inhibition is usually released upon binding to a cargo, which can then be transported to the specific destinations in cells. Cargo dependent control of motor activity makes great sense – as it avoids wastage of energy, prevents motors to pile up at the end of cytoskeletal tracks where they won't serve any useful purpose, and promotes motor recycling.

In summary, the transport characteristics of motor domains are regulated by the lipid-composition of cargo and the complex protein machinery that physically link the motors to its cargo.

1.3 *In vitro* approaches to study transport by motor proteins

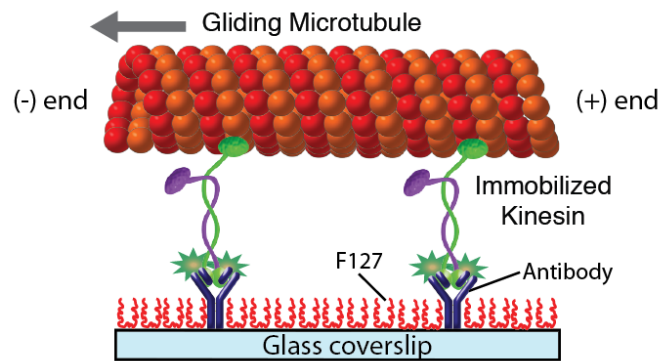
Since the discovery of Kinesin-1, several parallel approaches have been taken by scientists to study these fascinating molecular machines. For example molecular genetic techniques have been applied to assess the cellular function of different motors, by analyzing the phenotypes of cells due to different mutations (Gho et al., 1992; Hurd et al., 1996; Yonekawa et al., 1998). X-ray crystallography and electron microscopy have been used to resolve the structure of motor proteins and cytoskeletal filaments (Kull et al., 1996; Sack et al., 1997; Hirokawa, 1998; Kikkawa, 2008; A. Carter et al., 2011). Biochemical approaches have helped in ascertaining ATP binding affinity and rate constants for different motor proteins and identifying various interaction partners, and their role in motor regulation (Johnson et al., 1995; Moyer et al., 1998; Woźniak et al., 2006). However, our

understanding of the molecular mechanism of motor proteins have progressed tremendously by the development of *in vitro* or cell free assays, which gave us insights into the biophysics and working mechanism of various motors at molecular scale (Spudich et al., 1985; Vale et al., 1985; Gelles et al., 1988; McKenney et al., 2014). The recent technological progress made in the fields of the fluorescent probes and fluorescent microscopy, invention and development of highly sensitive charge-coupled device (CCD) cameras, accompanied with the advances in cell biology techniques such as recombineering have allowed us study these fascinating cellular machines at a single-molecule level, in well-controlled systems outside cell.

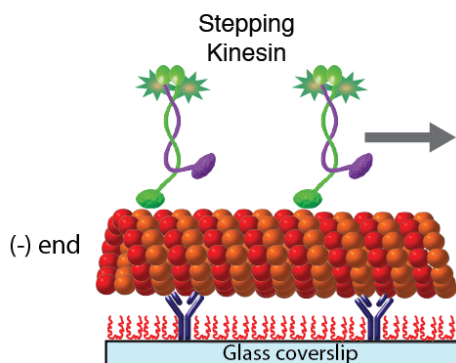
The *in vitro* motility assays can be performed in two different geometries gliding motility or stepping motility. In a conventional gliding motility assay motors are immobilized on a substrate either by adsorption or via antibodies and these surface bound motors can translocate cytoskeletal filaments such as microtubules or actin filaments, in presence of ATP (fig. 1.7A). Gliding motility assays are used for determining the gliding velocities of cytoskeletal filaments driven by multiple-motors (Paschal et al., 1987; Howard et al., 1989; Cheney et al., 1993; Hancock et al., 1998), studying dependence of motor activity on different nucleotide states (Coy et al., 1999; Hancock et al., 1999), and ascertaining the directionality of motor proteins (Walker et al., 1990).

Stepping motility assays involve inverse configuration, where the microtubules are immobilized on the surface via antibodies and the movement of individual motors or a bead coated with motors is monitored (fig. 1.7B). Furthermore, this configuration can be used in an optical tweezers set-up (fig. 1.7C), where the beads are trapped near the laser beam focus owing to interaction between the laser light and dielectric bead (Ashkin et al., 1986). The force experienced by the bead points towards the trap center and is proportional to the distance moved by the bead away from trap, for small distances. Therefore, optical trapping can be used to apply and measure forces on a bead coated with single or multiple motors interacting with microtubules, in the range of few tens of fN to 100 pN, reviewed in (Capitanio et al., 2013).

A Conventional Gliding Motility Assays



B Stepping Motility Assays



C Optical Trap Assays

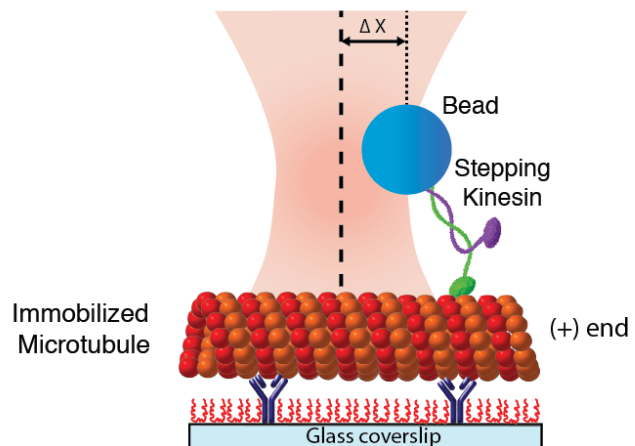


Figure 1.7 | *In vitro* motility assays. A) Conventional gliding motility assays, where surface-immobilized molecular motors propel the microtubules. B) Stepping motility assays, where molecular motors walk on surface-immobilized microtubules. C) Optical trap assays, where motors attached to a rigid bead walk on surface-immobilized microtubules. The bead can be trapped in the focus of laser beam and the displacement of bead from the focal point gives the stall force of motors.

***In vitro* studies on kinesin-1**

The above-mentioned *in vitro* assays have been applied to investigate the working mechanism of kinesin-1, and have revealed that a kinesin-1 motor, consisting of two motor domains, moves processively on a microtubule (Howard et al., 1989; Block et al., 1990). A processive motor can move continuously along the microtubule lattice, taking several steps before detaching. This requires that at least one of the head of a dimeric motor be always attached to the microtubule

(Hancock et al., 1998). It walks towards the plus-end of a microtubule in a stepwise hand-over-hand mechanism, with a discrete step-size of 8 nm, corresponding to the iteration distance of tubulin heterodimers within a protofilament in the microtubule lattice (Svoboda et al., 1993; Yildiz et al., 2004; Asbury, 2005; Kawaguchi, 2008). Kinesin-1 takes approximately 100 steps before detaching from a microtubule, hydrolyzing one ATP molecule for each step taken by the motor (Hua et al., 1997; Schnitzer et al., 1997). The ATPase activity follows Michaelis-Menten kinetics with saturation at around 100 μM ATP, at which it walks at a speed of 0.8 $\mu\text{m/s}$. The ATP hydrolysis cycle is coupled with the motor domain conformational change and the affinity to microtubules: The nucleotide-free, the ATP and the ADP.Pi states are tightly bound, while the ADP state is loosely bound to the microtubule (Crevel et al., 1996; Rosenfeld et al., 1996; Hancock et al., 1999). The current model of kinesin-1 mechano-chemical cycle is outlined below (fig 1.8)

Kinesin-1 motor heads in the solution are in ADP state, attachment of one of the motor head to a microtubule triggers the release of its ADP, and thus it changes to nucleotide-free strongly bound state to a microtubule, while the other head with ADP is in weakly bound state. The nucleotide free head then binds to ATP, causing the 'neck linker' to change its conformation from rearward pointing to forward pointing, thus introducing an internal strain into the molecule. This internal strain causes the rear motor head to undergo biased diffusional search towards the plus-end (forward direction) of microtubule. After hydrolysis of ATP into ADP.Pi, in the current rear head the diffusing head can attach to the next binding site, release its ADP to be in nucleotide-free strongly bound state. Upon the release of P_i , the rear head with ADP is in weakly bound state and the front head is in nucleotide-free strongly bound state. With the binding to ATP in the front head the mechano-chemical cycle can start again (Kawaguchi, 2008; Yildiz et al., 2008; Milic et al., 2014). This 16 nm step of one head, translocates the center of mass of kinesin motors by 8 nm.

During its stepping cycle, single kinesin-1 motor can pull a cargo against the viscous load of cellular cytoplasm, it has been shown that the kinesin-1 becomes slower with increasing resisting load, and comes to stall at ~ 6 pN (Svoboda et al., 1993; N. J. Carter et al., 2005). The magnitude of the stall force for kinesin-1

obtained from different approaches such as optical trapping, increasing the viscosity of environment, and studying the buckling of microtubule driven by single kinesin-1 motor was shown to be in the range of 4-8 pN (Hunt et al., 1994; Gittes et al., 1996; Visscher et al., 1999; Gagliano et al., 2010).

In summary, the *in vitro* studies performed on single kinesin-1 molecules have revealed that the tight coupling between ATP hydrolysis and stepping of motor domains ensure that the kinesin-1 dimer doesn't dissociate from the microtubule. It covers $\sim 1 \mu\text{m}$ at a speed of $\sim 0.8 \mu\text{m/s}$ and can take a maximum load of $\sim 6 \text{ pN}$. Therefore, kinesin-1 motor proteins are highly optimized for the fast long-ranged transport, where multiple motors can transport large membranous cargos inside a cell.

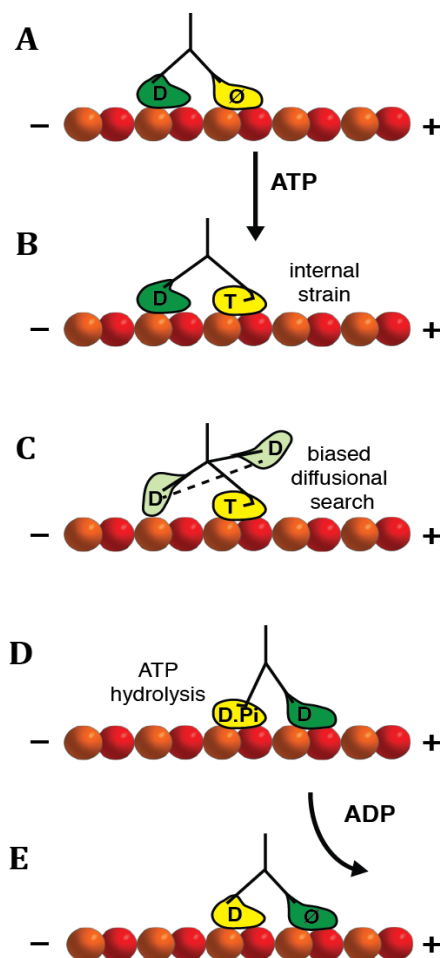


Figure 1.8 | Mechanochemical cycle of kinesin-1.

A) Forward head is in nucleotide-free (\emptyset), strongly bound state, while the rear head is bound to ADP (D), in a weakly bound state B) ATP binding to the forward head results in partial neck-linker docking, inducing internal strain between two heads. C) The strain causes weakly bound rear head to perform biased diffusional search for the next forward binding site. D) ATP hydrolysis occurs in the rear head such that it's now in ADP.Pi (D.Pi), strongly bound state, leading to complete neck-linker docking and E) ADP is then released from the forward head, which comes to nucleotide-free (\emptyset), strongly bound state and the Pi is released from the rear head, which comes to ADP (D), weakly bound state. One cycle is thus completed moving the center of mass of kinesin-1 by 8 nm towards the plus end of microtubule. Adapted from (Kawaguchi, 2008) with new findings from (Milic et al., 2014).

***In vitro* studies on kinesin-3**

Kinesin-3 motors, similar to kinesin-1, are involved in long-range cargo transport inside the cell with a velocity of $\sim 1.2 \mu\text{m/s}$. However, unlike kinesin-1, which is dimeric, kinesin-3 family members such as KIF1A are known to be monomeric – so the question arises how does a monomeric motor achieve processivity? Several *in vitro* approaches have been undertaken to reveal the transport mechanism of KIF1A. Single-molecule studies of wild-type recombinant KIF1A revealed that its moving monomeric motor head is weakly supported by an electrostatic interaction between its positively charged K-loop and the negatively charged C-terminal E-hook of the microtubule. It was proposed that the weak electrostatic interaction coupled with ATP hydrolysis conformational changes, enable KIF1A to search for next forward binding site on a microtubule through Brownian motion, without detaching from it. Brownian motion is biased so that the motor takes step towards the plus-end of a microtubule (Okada et al., 2000, 2003). However, the observed motion of the chimeric construct of KIF1A with kinesin-1 neck linker in the stepping motility assays was relatively oscillatory, where the motors took several forward and backward steps, and the stepping velocity was eight times less than the reported *in vivo* speeds of KIF1A (Zhou et al., 2001). Therefore, the biased-diffusion model did not support the smooth and rapid transport of cargo as observed inside cells. Another proposed mechanism is the concentration dependent dimerization of KIF1A, where it was shown that by increasing the number of attached recombinant wild-type KIF1A motors to the cargo, it was transported smoothly (Klopfenstein et al., 2002). Furthermore, the artificially created recombinant dimeric forms of KIF1A displayed smooth processive motion with the velocity similar to the observed *in vivo* velocities (Tomishige et al., 2002). However, what regulates the dimerization of KIF1A inside the cell is still controversial, as KIF1A was shown to exist in a self-inhibited dimeric form *in vivo* (Hammond et al., 2009). Currently, it is being proposed that the activation and dimerization of kinesin-3 members are regulated by its binding to a cargo (Soppina et al., 2014). Thus, the mechanism underlying the transport by kinesin-3 is still a topic of debate in the field, particularly in the light of recent studies, which have shown various other member of kinesin-3 such as HsKIF13B, HsKIF1C, and DmKin73

exist in dimeric state in cells (Dorner et al., 1999; Hammond et al., 2009; Huckaba et al., 2011). Therefore, unlike the kinesin-1 family members, having a unified functional mechanism, different kinesin-3 motors might have their own unique working mechanism. Until now, there has been only one single-molecule *in vitro* study reported in the literature for kinesin-3 member KIF16B (Soppina et al., 2014). In their work Soppina et al. have shown that the dimeric truncated construct of KIF16B, consisting of only motor domain are superprocessive with run-lengths of greater than 10 μm .

The single-molecule *in vitro* studies have vastly increased our understanding of the molecular mechanism of individual motors such as kinesin-1. However, there is an increasing amount of evidence that the intracellular cargo transport is mediated by teams of molecular motors and not single motors. The observations such as intracellular cargo cover much longer distances than what is measured for single motors, and many organelles display bi-directional movement indicate that a group of motors with different directionality are simultaneously moving a cargo (Hill et al., 2004; Kural et al., 2005; Shubeita et al., 2008; Ally et al., 2009; Soppina et al., 2009; Hirokawa et al., 2010; Hendricks et al., 2012). Therefore, there is a growing interest in the intracellular-transport research field to understand the mechanism of collective transport by motors. In recent past, several *in vitro* studies have been performed to investigate the transport mediated by teams of similar or different motors, where ensemble of motors are attached to cargos such as quantum dots (Conway et al., 2012), silica beads (A. R. Rogers et al., 2009), DNA scaffolds (Derr et al., 2012; Furuta et al., 2013) and glass substrates – conventional gliding motility assays (Leduc et al., 2007; Gagliano et al., 2010). Although, these approaches provide us with insights about the collective dynamics of multi-motor transport, they still are quite distant from mimicking the motor driven cargo transport inside cells. A key anomaly in these *in vitro* systems is the use of non-physiological cargo. Organelle transport driven by molecular motors entails their attachment to a membranous cargo. The motors while active, in contrast to being fixed to a rigid cargo such as solid substrate, are linked to a diffusive lipid bilayer. The anchoring of motors in a diffusive environment induce loose inter-motor coupling and increase the

flexibility of the system. Thereby, attachment to a diffusive cargo might result in a co-ordination in the transport by multiple motors.

1.4 Aim of this study

In a eukaryotic cell, membranous vesicles and organelles are transported by ensembles of motor proteins. Although many motor proteins have been well characterized at the single-molecule level, the effect of motor anchoring to a diffusive cargo on the collective dynamics of motors is poorly understood. In this study, we investigate the cooperative effects in transport system driven by multiple kinesin motors anchored to a diffusive lipid bilayer. To pursue our goal we aimed to establish gliding motility assays with kinesin motors linked to a supported lipid bilayer (SLB) so called 'membrane-anchored' gliding motility assay. Thereby, dependence of transport velocity on relevant biological parameters such as motor density, and lipid-bilayer diffusivity will be examined quantitatively.

Molecular motors attach to their cargo either indirectly by adaptor proteins or directly with their lipid binding domains. To mimic both the scenarios we plan to use two different systems (i) kinesin-1 tagged SBP, which is indirectly linked to biotinylated SLBs via streptavidin and (ii) full-length (FL) KIF16B, which is directly attached to PI(3)P SLBs.

FL KIF16B motor has not been characterized at the single-molecule level, to date. Thus, biophysical properties of purified recombinant FL KIF16B motors will be characterized, using single-molecule fluorescence microscopy.

2 Transport by kinesin-1 anchored to supported lipid bilayers (SLBs)

In vitro gliding motility assays, where several motors immobilized on surface propel microtubules, can be utilized to get mechanistic insight into the multi-motor transport. In traditional gliding motility assays it was found out that the microtubule gliding velocity, for full-length drosophila KHC, is mostly independent of the surface motor densities as well as the length of microtubules, (Howard et al., 1989; Hunt et al., 1994). This is because the microtubule motility in the aqueous environment results in a very low drag force on the motors, much less than stall force for kinesin-1. This enables even a single motor to propel microtubule at maximum velocity. However, if there are multiple motors propelling a microtubule, a certain degree of co-ordination is required so as to avoid the motors to start impeding each other, where one motor is stepping but others are not. This phenomenon was illustrated for the truncated constructs of KHC where the microtubule gliding velocities were lower than the single motor stepping velocity and the gliding velocities decrease with increasing motor densities (Bieling et al., 2008; Crevenna et al., 2008). In another study, utilizing the approach of traditional gliding assay, it was demonstrated that multiple kinesin-1 motors step asynchronously on a microtubule (Leduc et al., 2007). In addition, from the optical trap studies on single kinesin-1 motor it is established that most of the time in a stepping cycle of the motor (\sim ms) is spent waiting on the microtubule, where the actual stepping is almost instantaneous (\sim μ s) (N. J. Carter et al., 2005). All these studies put together illustrate that the flexibility in the transport system is critical for its efficiency; otherwise increase in number of motors driving transport would produce a counterintuitive effect of opposing each other resulting into lower velocities. Intracellular transport of membranous cargo by motors involves implicit flexibility by virtue of attachment to a diffusive lipid bilayer.

Few studies have used the lipid bilayer as a cargo to investigate the biophysical characteristics of actin filaments based motor proteins. Liposomes consisting of 1,2-dioleoyl- sn-glycero-3-phosphocholine (DOPC) were utilized to demonstrate that the collection of myosin Va could drive the transport of diffusive cargo at velocities greater than the single motor velocity, due to preferential detachment of trailing motors (Nelson et al., 2014). Supported lipid bilayers on glass have been employed to demonstrate that the membrane bound myo1C, propels actin filaments in a counter clockwise direction indicating asymmetry in its stepping (Pyrpassopoulos et al., 2012). A recent study from our group reported the long-range transport of giant vesicles (1-4 μm) driven by kinesin-1 motors as a proof of concept that model membrane systems can be utilized to study microtubule based motors such as kinesin-1 (Herold et al., 2012). However, the assays to quantitatively determine the effect of anchoring to a lipid bilayer on collective transport velocities and forces remain to be established.

In this study we investigate the transport dynamics of multiple kinesin motors in conjunction with a diffusive cargo. To realize this goal we aimed to

- Reconstitute, microtubule gliding driven by multiple-motors anchored to a diffusive supported lipid bilayer
- Determine quantitatively the effect of biologically relevant factors such as motor density, microtubule length and diffusivity of the membrane on the collective transport dynamics
- Develop a theoretical model to understand the biophysical characteristics of transport by membrane-anchored motors and reconcile our experimental findings with the model

The first two sections of this chapter describe the steps involved in reconstitution of gliding motility assay on kinesin-1 motors attached to a lipid bilayer namely (i) generation of planar SLBs on glass substrate and (ii) attachment of kinesin motors to the SLBs. The next section demonstrates the results for transport velocities of microtubules propelled by lipid bilayer anchored kinesin-1 as a function of surface density of motors and how are they distinct from the conventional gliding motility. The subsequent section then

explains the theoretical description of the *in vitro* gliding motility on lipid bilayer anchored motors, based on the physical characteristics of the components. The final two sections compare the predictions of theoretical model with the experimental findings.

2.1 Formation and characterization of biotinylated SLBs

Model membrane systems such as liposomes, GUVs, SLBs and lipid monolayers provide us with an excellent tool to investigate the protein-membrane interactions with a desired lipid composition. The key characteristic of such a system is the fluidity, where the components associated with the membrane are free to diffuse in the plane of lipid bilayer. In recent years, a few studies have employed membrane systems such as GUVs, and liposomes to mimic the cargo transport *in vitro* (Herold et al., 2012; Nelson et al., 2014). However, the quantification of the number of motors involved in transport for such systems is not straightforward because of the spherical geometry, which limits the imaging of individual motor proteins with high spatial resolution. This problem can be tackled by using planar SLBs that can be imaged with single molecule sensitivity using TIRF or confocal microscopy while retaining the fluidity of the system. The process of a SLB formation, depending on the lipid composition, on a solid support can be complex. But once the critical parameters such as buffer, vesicle size, and hydrophilicity of the substrate are optimized they are straightforward to generate.

In our experiments, SLBs were prepared with the lipid composition DOPC:DSPE-PEG (2000)-Biotin in the molar ratio 99:1. DOPC with its low transition temperature of -17 °C is fluid at room temperature making it one of the most extensively used and studied phospholipid (Richter et al., 2006; Chan et al., 2007). Biotin functionalized PEG lipids were used to attach the motor proteins to the SLBs. 20 mM HEPES supplemented with 75 mM NaCl (H20S75) was found to be the buffer in which the motor proteins as well as the SLBs were stable. Hence, all the experiments were performed in this buffer.

To check for the quality of SLBs we monitored its homogeneity, diffusivity and mobile fraction. Lipids were doped with 0.05 % DOPE-Atto647n as a fluorescent

lipid marker. The uniformly spread lipid marker indicated that the SLBs formed were homogenous (fig. 2.1A). To determine the diffusivity and mobile fraction of lipids in SLBs, fluorescence recovery after photobleaching (FRAP) experiments were performed. FRAP analysis, after correcting the images for fixed pattern noise, was performed according to methodology described by (Goehring et al., 2010) (see FRAP analysis, chapter 5, page 118 for details). The diffusion coefficient of SLBs was obtained to be $2.97 \pm 0.29 \mu\text{m}^2/\text{s}$ ($n = 16$, 4 independent experiments) from fitting the fluorescence recovery curves. All the SLBs formed had greater than 95% mobile fraction (fig. 2.1 B). Hence, these results demonstrate that homogenous, diffusive and entirely mobile biotinylated SLBs were formed on glass substrate.

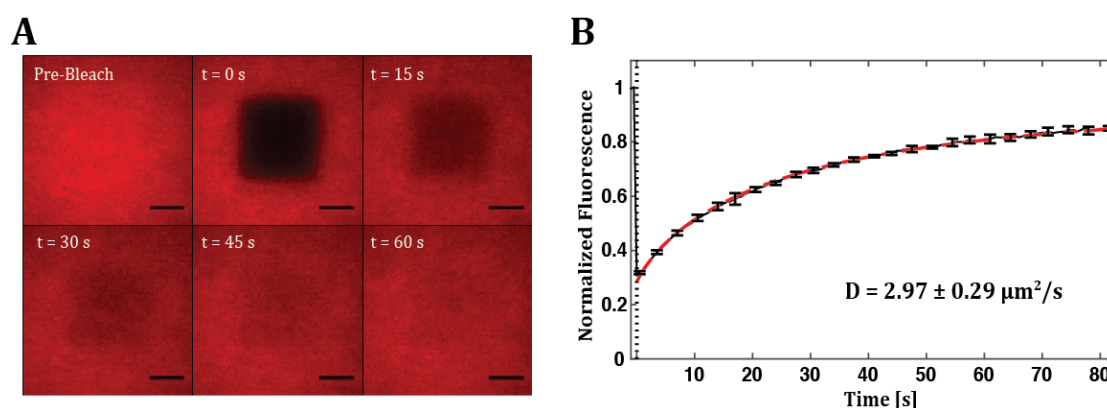


Figure 2.1 | Biotinylated SLBs formed on glass were homogenous and diffusive.

A) Time lapse fluorescence images of FRAP for 1% biotinylated SLBs with B) Representative normalized intensity plots vs time for a set of photobleached regions. Mean FRAP recovery curves (black line \pm s.d.) are shown along with the best fit (dashed red line). 4 different regions on a SLBs were bleached to get the mean FRAP recovery curve. Mean diffusion coefficient (mean \pm s.d.) is obtained from 4 independent SLB preparations. Scale bar: 10 μm .

2.2 Anchoring kinesin-1 to biotinylated SLBs

The next step was to anchor a motor protein to the diffusive SLBs. Our motor of choice for this study was kinesin-1 as it is the most extensively studied kinesin motor protein. To attach kinesin-1 motors to the SLBs, we prepared a construct of kinesin-1 having a streptavidin binding peptide (SBP) tag at its tail, which can be linked to the biotinylated SLBs via streptavidin. We expressed a rat kinesin-1 heavy chain isoform KIF5C, truncated to first 430 a.a. with 8xHis and an SBP tag at the C-terminal (rKin430-SBP). To perform single molecule studies and determine the motor density we need to visualize the motor, hence we prepared a fluorescent rKin430-SBP construct labeled with multifunctional GFP tag (rKin430-SBP-GFP) (fig. 2.2A), such that the SBP tag is on the opposite end of N- and C- terminal of GFP (Kobayashi et al., 2008). This would ensure that the motors attach to the SLBs in a correct orientation with the motor heads facing away from the SLBs. SBP tagged kinesin-1 constructs were expressed in *E. coli* and purified with His affinity chromatography (fig. 2.2B) (see chapter 5, page 105 for details).

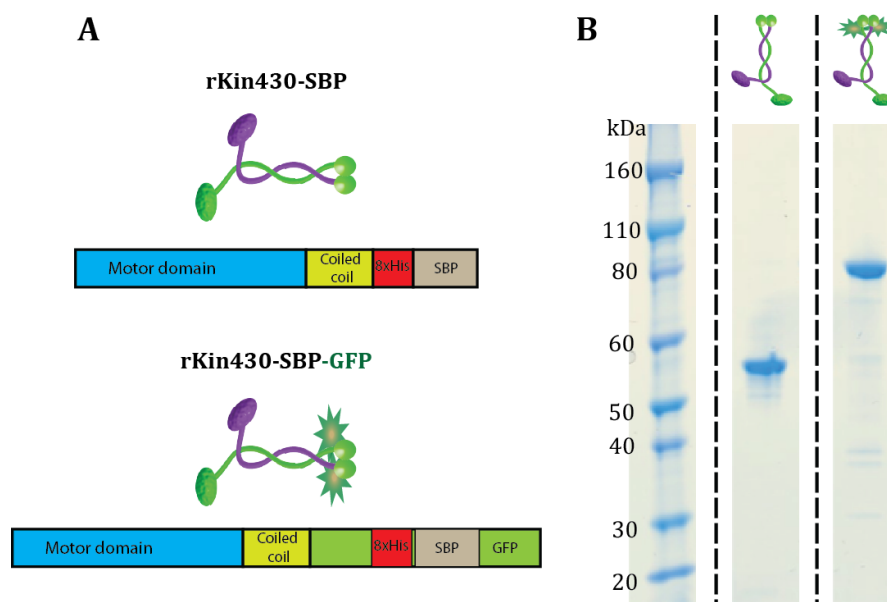


Figure 2.2 | Truncated rat kinesin-1 constructs with SBP tag were purified with His tag affinity chromatography. A) Schematics showing kinesin-1 SBP constructs rKin430-SBP and GFP labeled rKin430-SBP-GFP B) Coomassie stained gel showing the purified fractions for both the constructs. The expected molecular weight for rKin430-SBP and rKin430-SBP-GFP is 54.1 and 82.9 kDa respectively.

The addition of SBP tag at the C-terminal might have altered the functionality of kinesin-1. To characterize the activity of the purified SBP tagged kinesin-1 constructs we performed *in vitro* stepping and gliding motility assays. Interaction of individual rKin430-SBP-GFP motors with the microtubules, surface-immobilized via antibodies, was recorded in TIRF microscopy (see Stepping motility assay, chapter 5, page 112). The mean velocity and run length of motors were determined by evaluating the space-time plots 'kymographs' of the motors on microtubule path (fig 2.3A) (see Data analysis, chapter 5, page 124). The mean velocity of $0.662 \pm 0.143 \mu\text{m/s}$ (mean \pm s.d., $n = 545$) with a run length of $1.05 \pm 0.05 \mu\text{m}$ (mean \pm 95% c.i., $n = 545$) was obtained from the evaluation (fig. 2.3B-C). The reported values for rKin430-GFP motors mean velocity and run length is $0.8 \mu\text{m/s}$ and $0.9 \mu\text{m}$, respectively (Schneider et al., 2015). From our evaluation we find a lower velocity and higher run length for rKin430-SBP-GFP as compared to the reported values. This can be due to the low ionic strength (IS) of H20S75 buffer (IS 80 mM) as compared to BRB 80 buffer (IS 160 mM), which is the common buffer used for most of the kinesin-1 studies. As the motor head binds to a microtubule via electrostatic interaction, the salt concentration and the IS of the buffer can impact the interaction. Previous studies have also shown the similar effects for Kinesin-1 (Böhm et al., 2000). Our results demonstrate that the rKin430-SBP-GFP construct is active and the SBP tag does not alter its interaction with the microtubule.

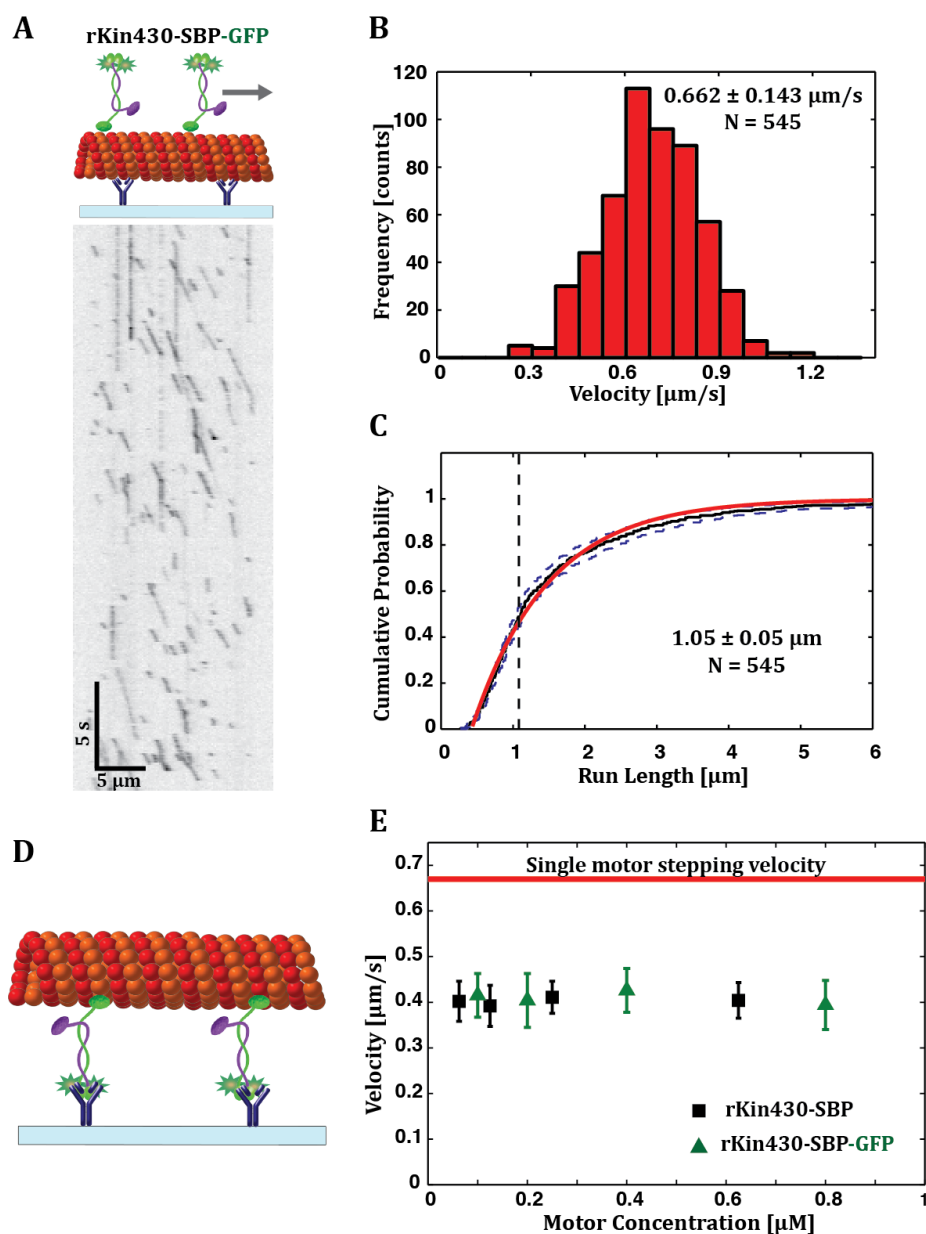


Figure 2.3 | SM stepping velocity of rKin430-SBP-GFP is higher than the MT gliding velocity on surface-immobilized motors. A) Representative kymograph of single rKin430-SBP-GFP molecules moving on a surface-immobilized microtubule. Time is progressing from top to bottom, while the motors (dark signals) move along a microtubule from left to right. B) Histogram of single molecule velocities with ensemble average (mean \pm s.d.). C) ECDF (black solid line, with 95% c.i. bounds dotted blue lines) with a single exponential fit (red) of the run lengths (mean \pm 95% c.i.). N is the number of molecules analyzed, from 3 independent experiments. D) Schematic of the microtubule gliding motility assay on motors immobilized on glass substrate via antibodies. E) Gliding velocities (mean \pm s.d.) obtained for rKin430-SBP (black) and rKin430-SBP-GFP (green) at different motor concentrations. Solid red line indicates the mean single molecule velocity. More than 70 microtubule tracks were analyzed in at least two independent experiments for each concentration.

To check for the activity of unlabeled rKin430-SBP and to compare it with rKin430-SBP-GFP we performed conventional gliding motility assays, whereby motors were immobilized on a glass surface via antibodies against the his tag present at the tail of motors. Rhodamine labeled microtubules were then flushed in and their motility was recorded by imaging in fluorescent microscope (see Gliding motility assay, chapter 5, page 113). The mean gliding velocity was then evaluated from the histograms of instantaneous velocity of microtubule center using FIESTA (see Data analysis Chapter 5, page 121). The mean gliding velocity of microtubules were similar for both the constructs with $0.402 \pm 0.029 \mu\text{m/s}$ and $0.409 \pm 0.034 \mu\text{m/s}$ (mean \pm s.d., $n = 3$, with > 60 microtubules for each experiment) for rKin-SBP and rKin-SBP-GFP, respectively. The results suggest that both the constructs were functionally similar.

However, the mean microtubule gliding velocity in multi-motor assays is much lower than the mean stepping velocity of individual motors. This can be attributed to the fact that the truncated constructs of kinesin-1 rKin430 attached rigidly to a substrate are torsionally stiff as compared to the full length KHC. The lack of flexibility would thus make motors impede each other in a multi-motor assay. Since the motors step asynchronously, at any instance only a few motors are stepping and the rest of the motors hinder the active motors generating enough load to slow down the gliding velocity (Bieling et al., 2008). Another reason could be inactivation or clustering of a few motors due to antibody binding. Some of these non-functional motors, which bind to microtubules in a rigor state, would also increase the hindering load on the stepping motors, leading to a lower velocity. The impediment of motors scales with the motor densities, such that lowering the motor density would increase the gliding speed. To test the effect of motor density on the gliding velocity of microtubules, we performed the gliding assays for a range of concentration of motors, keeping the concentration of antibodies, to which the motors are bound, constant. We did not observe any significant effect of motor density on gliding velocity for both the rKin430-SBP constructs as we obtained a constant value of around $\sim 0.4 \mu\text{m/s}$, over a range of motor concentration (fig. 2.3E). There could be two possible reasons for the above observation, (i) rKin430-SBP is torsionally compliant but binding to the antibodies might have affected the functionality of motors, such

that they could not fully attain its force-producing conformation, (ii) the actual density of the motors on the surface might be set by the antibody concentration, which was not varied. Experiments with different antibodies and at different concentration of antibodies could be performed to test for the above reasons. However, the important finding for our system is that both the constructs were functionally similar.

The next checkpoint for rKin-SBP constructs was to investigate their binding to the SLBs. To attach motors to the biotinylated SLBs we first incubated the SLBs with excess streptavidin (~100 folds higher than the number of biotinylated lipids) so that the SLBs are saturated with streptavidin. This would ensure that the surface density of motors is regulated by the bulk concentration of motors applied to the SLB and not by the number of binding sites available.

To test whether the SBP tagged kinesin-1 binds to the biotinylated SLBs, saturated with streptavidin, we used rKin430-SBP-GFP motors. The GFP labeled motors were incubated with SLBs after washing off the unbound streptavidin. By imaging the labeled rKin430-SBP-GFP in TIRF microscopy, we observed the diffusing molecules on the surface of SLBs, indicating binding of rKin430-SBP-GFP on the SLBs.

To investigate the molecular information on motor-lipid interaction we determined the diffusivity of rKin430-SBP-GFP attached to SLB by single particle tracking (SPT) experiments using TIRF microscopy (see Image acquisition, chapter 5, page 118). For single molecule sensitivity, SLBs were either incubated with very low concentration of rKin430-SBP-GFP or spiking experiments were performed, where the concentration of rKin430-SBP-GFP were kept low but overall concentration was increased by addition of unlabeled rKin430-SBP. The single molecules were tracked using FIESTA. Displacement data for all the single molecule trajectories (fig. 2.4A) were calculated for discrete time points, defined by the image acquisition rate (50 ms) and the displacement data were cumulated to calculate the average mean square displacement (MSD) for every discrete time point. The first 8 points (based on the estimation published in Michalet, 2010) of the MSD thus obtained was then fitted with a linear curve using the error bars as weights (fig. 2.4B) (see Data analysis, chapter 5, page 123) The ensemble average

diffusion coefficient of rKin430-SBP-GFP was obtained to be $3.11 \pm 0.24 \mu\text{m}^2/\text{s}$ (mean \pm 95% c.i., $n = 40$). The diffusivity of rKin430-SBP for different concentration of motors were similar, with no significant difference. The diffusion coefficient of rKin430-SBP from SPT analysis matches well with the diffusion coefficient of the lipids in SLBs $2.97 \pm 0.29 \mu\text{m}^2/\text{s}$ obtained from FRAP analysis. This indicates that diffusivity of rKin-SBP-GFP is governed by the diffusivity of lipids and the surface density of motors does not affect its diffusivity. The fact that the diffusion coefficient of motors is similar to the SLBs reveals that the rKin430-SBP on an average binds to single biotinylated functional lipid (Knight et al., 2010). In conclusion, our diffusion studies confirm the diffusive binding of rKin430-SBP motors to the SLBs.

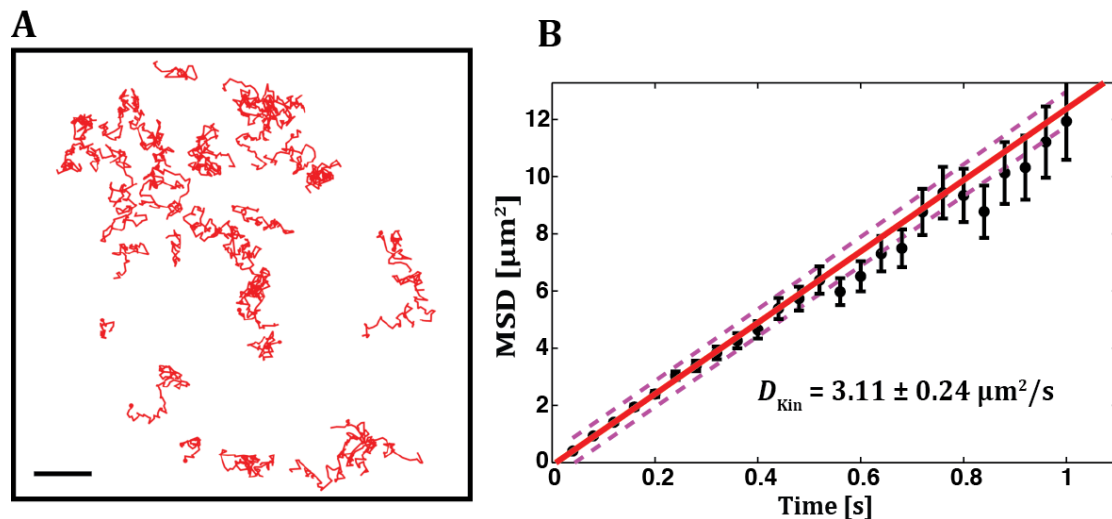


Figure 2.4 | SBP tagged kinesin-1 constructs were diffusive, when anchored to biotinylated SLBs. A) Trajectories of freely diffusing rKin430-SBP-GFP attached to 1% biotinylated SLBs. B) Cumulative mean squared displacement (MSD) data (black, mean \pm s.d.) of diffusing rKin430-SBP-GFP molecules with a linear fit (red line) to first eight points, and 95 % c.i. of the fit is shown (dashed magenta line). The diffusion coefficient (mean with 95 % CI, $n = 40$) of rKin430-SBP-GFP was determined from the linear fit. Scale bar: 10 μm .

2.3 Gliding motility of microtubules by kinesin-1 linked to SLBs

After ensuring that the SBP tagged kinesin-1 constructs were functional and diffusively anchored to the biotinylated SLBs, we performed the microtubule gliding motility on membrane-anchored kinesin-1 (fig. 2.5A). The unbound motors were washed off and fluorescently labeled microtubules were applied to the membrane-anchored motors. The microtubule gliding were then imaged with fluorescent microscopy (see Image acquisition, chapter 5, page 118).

One of the striking observations, for microtubule gliding on membrane-anchored kinesin-1, was that the microtubules on collision did not cross each other (fig. 2.5 B-C). Whereas, in a traditional gliding assay the microtubules propelled by surface-immobilized kinesin-1, cross over each other without any noticeable effect upon collision (fig. 2.5D). The microtubules can be considered as hollow rigid rods with a persistence length of several hundred micrometers (Clemmens et al., 2003; Nitta et al., 2005; Van den Heuvel et al., 2007). Due to such high stiffness the microtubules trajectories in a traditional gliding assays are rather straight. The stiffness of the microtubule is also a critical factor in determining the fluctuation of its leading end. The stiffer microtubules would fluctuate less as compared flexible microtubules. In a traditional gliding assays even the stiffer microtubules cross each other without any hindrance.

To test the role of microtubule stiffness on the crossing behavior in membrane-anchored gliding assays we used taxol-stabilized microtubules (Tx-MT), which have a persistence length of about 0.2 – 0.5 mm and microtubules which are polymerized with GMP-CPP and then stabilized with taxol – double stabilized microtubules (DS-MT) which are more stiffer with a persistence length of ~1.9 mm (Hawkins et al., 2013). Here, we didn't observe any crossing of Tx-MT as well as DS-MT in the membrane-anchored gliding motility assays (fig. 2.5B,C). Tx-MT always aligned with a passing microtubule. In comparison, DS-MT were aligned or stalled depending on the colliding angle with a passing microtubule. This could be attributed to the low force output of membrane-anchored rKin430-SBP, where the motors themselves slip backwards in the lipid-bilayer rather than pushing the microtubules forwards in the solution.

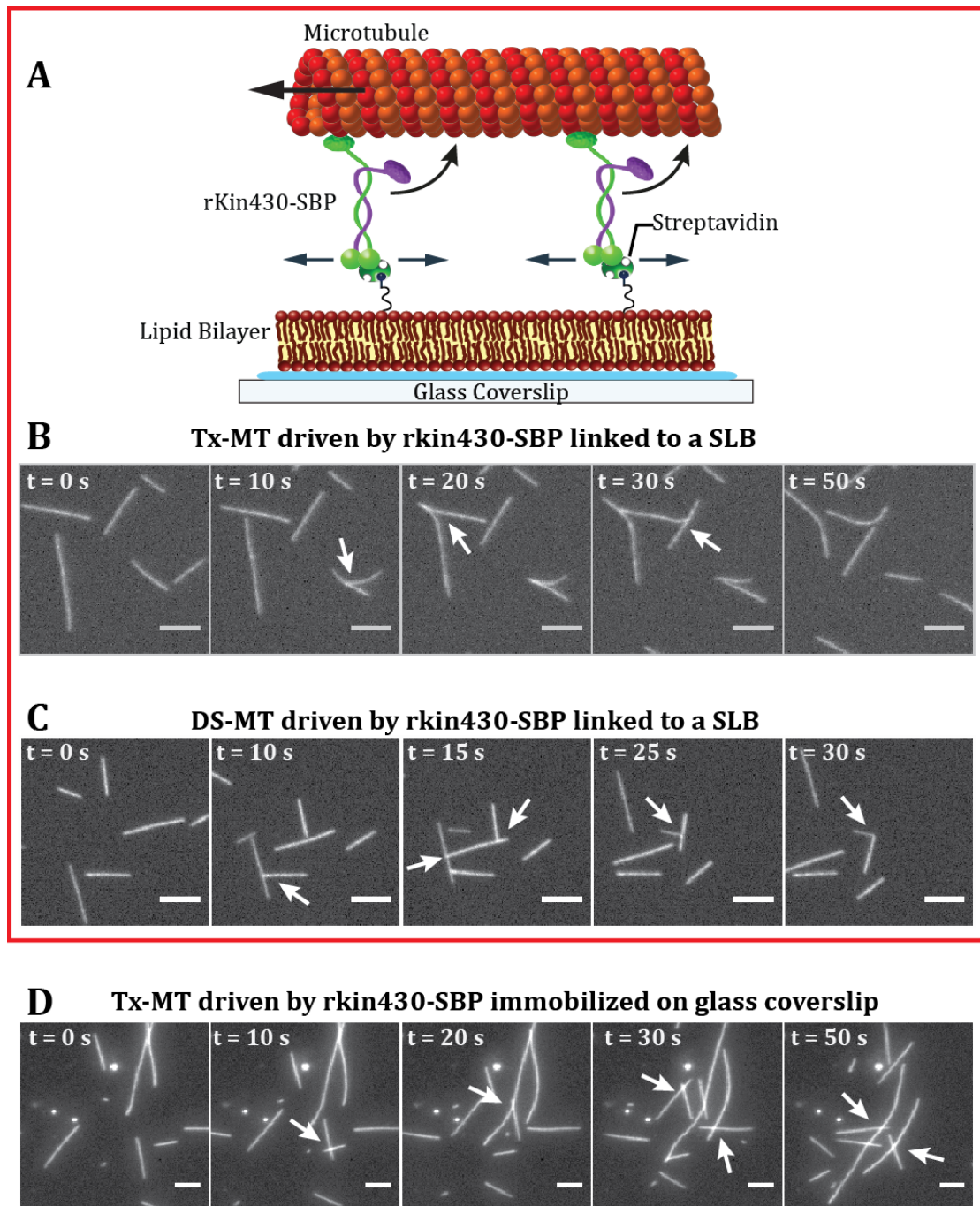


Figure 2.5 | Gliding microtubules do not cross each other when propelled by membrane-anchored kinesin-1. A) Schematic cartoon (not drawn to scale) of the experimental set-up, rKin430-SBP is attached, via streptavidin, to 1% biotinylated SLB. Microtubules are driven by membrane-anchored motors. Time-lapse images for microtubules driven by rKin430-SBP attached to SLB B) Microtubules grown in GTP and stabilized with Taxol, Tx-MT and C) Stiffer microtubules, grown in GMP-CPP and stabilized with Taxol, DS-MT. D) Time-lapse images for Tx-MT driven by rKin430-SBP rigidly bound to substrate via antibodies. Scale bar: 5 μ m.

The gliding assays on surface-immobilized rKin430-SBP did not show any dependence on surface motor densities (fig. 2.3 E). However, does the number of motors propelling the microtubule in membrane-anchored gliding affect the collective transport dynamics? To address this question, we performed gliding motility assays on membrane-anchored motors, at different motor densities. The surface motor density was varied by incubating the streptavidin bound biotinylated SLBs with different concentration of motors ranging from (0.8 μM – 0.04 μM), for a period of 6 minutes following which the unbound motors were washed off from the reaction chamber.

At higher motor concentrations many microtubules landed on the surface indicative of higher motor density. Furthermore, microtubule gliding was fast and smooth with many microtubules entering and leaving the field of view (FoV). In contrast, at lower motor concentrations only a few microtubules landed on the surface and the microtubules glided slowly with their trajectories becoming wigglier. This behavior was identical for unlabeled as well as GFP labeled rKin430-SBP. Thus, it can be concluded that in membrane-anchored gliding motility assays microtubule gliding behavior was dependent on the surface motor density of membrane-anchored kinesin-1 (fig. 2.6A).

To quantify the observed behavior and calculate the microtubule gliding velocity, translocation of microtubules was divided into two components (i) translational component due to active transport by the motors and (ii) diffusion component due to attachment to a diffusive lipid bilayer via motors. The contribution of second component is low at high motor density, as a microtubule is pinned to the diffusive lipid bilayer by many motors at any instance. Thus they experience high drag force and their mobility due to diffusion is reduced. However, at low motor density a microtubule is pinned by very few motors and hence it's mobility due to diffusion increases and its trajectory gets wigglier. The mobility of microtubules due to diffusion also depends on its length, as can be seen in the maximum projections (see fig. 2.6A), the shorter microtubules wiggles much more than the longer ones. This is expected, as the drag coefficient for a cylindrical object such as a microtubule scales linearly with its length hence the shorter microtubules are more diffusive than the longer ones. As a consequence,

the microtubules motility driven by membrane-anchored motors can be interpreted as objects diffusing in a constant flow.

The translocation of a microtubule propelled by membrane-anchored motors was quantified by determining the MSD of the microtubule center over time. Translational and diffusive component were separated by fitting the MSD plot with the following equation as described in (Qian et al., 1991)

$$MSD(n\Delta t) = \underbrace{(v \cdot n\Delta t)^2}_{\text{Translational}} + \underbrace{4D \cdot n\Delta t}_{\text{Diffusive}} + c \quad (2.1)$$

where v is the translational velocity of a microtubule, D is the diffusion component and c is the offset accounting for the localization uncertainty and the dynamic error due to finite camera acquisition time (Michalet, 2010). Due to the imaging of discrete frames the time t is given as multiples n of the acquisition time interval such that $t = n\Delta t$. ($\Delta t = 1$ s for our experiments). The MSD data of microtubule center, for all the different motor concentrations, fitted well to equation 2.1 (fig. 2.6B). From equation 2.1 we can deduce that if the motors are not actively propelling a microtubule the MSD of microtubule center should be linear. To examine this we performed gliding assay in presence of 0.1 mM adenylyl imidodiphosphate tetralithium salt (AMP-PNP), a non-hydrolysable analog of ATP where the motors are bound to the microtubules in a rigor state without stepping. The plot of cumulated MSD over time for such microtubules was linear (fig. 2.6B, dashed brown line) indicating only diffusive component in its translocation. This validated our assumption of considering microtubules, driven by membrane-anchored motors, as objects diffusing in a constant flow. Thus the ensemble average gliding velocity of microtubules at different motor concentrations were obtained by fitting the cumulated MSD, calculated from all the individual microtubule trajectories (see Data analysis, chapter 5, page 121 for details).

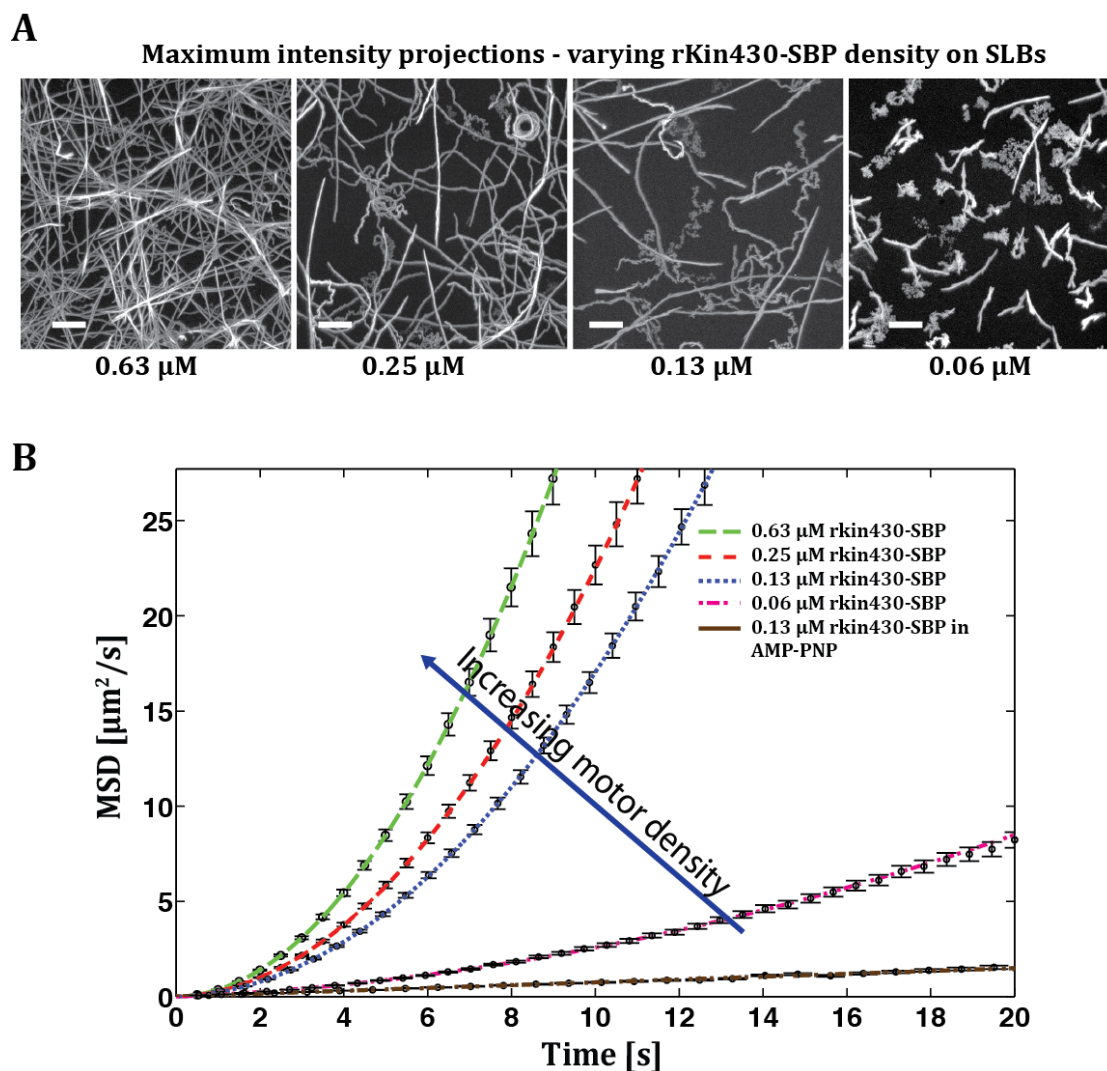


Figure 2.6 | Ensemble average microtubule velocity and diffusivity on SLBs were determined by fitting their MSD as a function of time. A) Maximum projections of 200 frames, 1s/frame time-lapse movie for microtubules driven by membrane-anchored rKin430-SBP, at four different motor densities decreasing from left to right with bulk motor concentrations 0.63 μM , 0.25 μM , 0.13 μM and 0.06 μM respectively. Scale bar: 10 μm . B) Cumulative MSD vs. time plots for the center of microtubules are shown (mean \pm s.e.m.) with the fit (dashed lines) for varying motor densities (0.63 – 0.06 μM) in ATP and for 0.13 μM in AMP-PNP. The data was fitted to the equation (2.1).

For membrane-anchored gliding motility assays, we found that the gliding velocity determined from the fit, increased with the increasing motor concentration (fig. 2.7) and reached almost as high as the single motor stepping velocity of 0.662 $\mu\text{m}/\text{s}$. This is in contrast to the gliding velocities for surface-immobilized motors, which were independent of the motor surface density with a value \sim 0.40 $\mu\text{m}/\text{s}$. This exhibits that the negative interference of static motors,

observed in multi-motor transport for rigidly bound motors is reduced due to the fluidity of the bilayer. Instead the velocity increases with the increasing motor concentration, indicating the co-operative interference of motors. To understand the underlying principles behind the co-operative effects seen in the transport systems driven by membrane-anchored motors, we developed a theoretical model described in the following section.

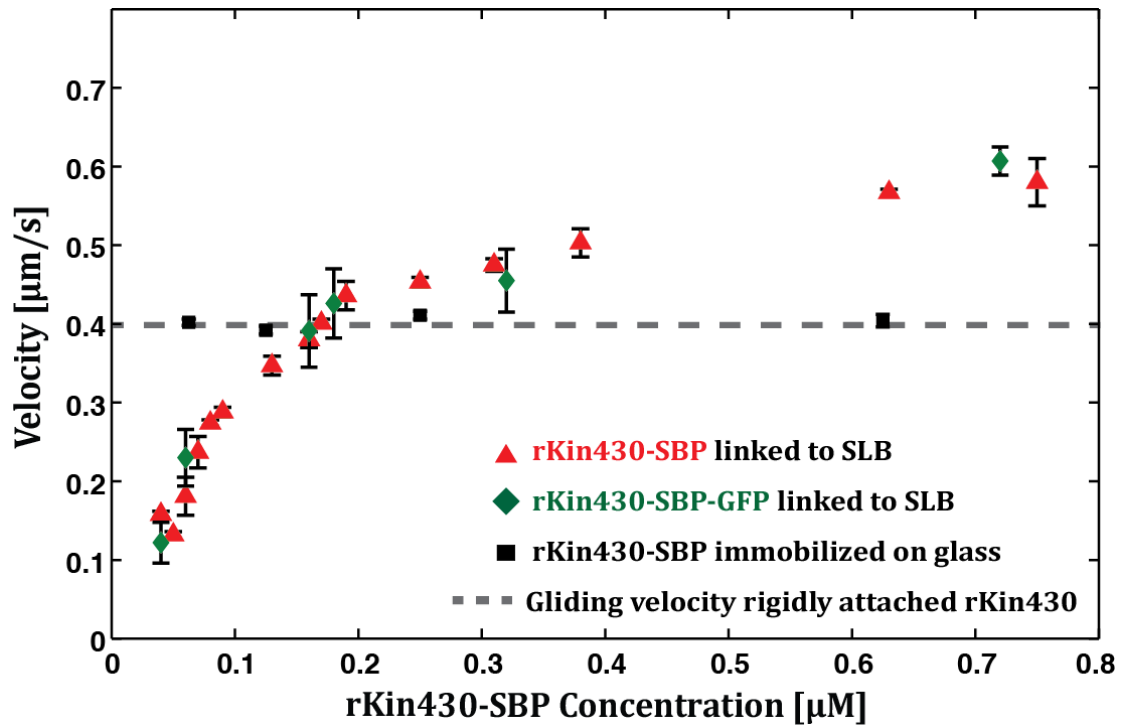


Figure 2.7 | Microtubule gliding velocity, for membrane-anchored kinesin-1, increased with motor density attaining velocities higher than for surface-immobilized motors. A) Averaged microtubule gliding velocities at different motor concentrations of rKin-SBP (red) and rKin-SBP-GFP (green), for membrane-anchored gliding assays. Microtubule gliding velocities for rKin430-SBP, immobilized on glass via antibodies, at different concentrations are also shown (black). Dashed grey line is drawn as a guide to eye, to indicate the microtubule gliding velocity for surface-immobilized rKin430-SBP over a wide range of motor concentration, which was found to be constant. Error bar represents 95 % c.i. for the velocities obtained from the fit.

2.4 Theoretical description of gliding motility on diffusing motor proteins

To understand our observations of increase in gliding velocity with the increasing motor density, we developed a theoretical description of gliding motility driven by membrane-anchored motor. From the gliding assays on surface-immobilized motors we know that the ensemble of kinesin-1 motors does not step synchronously (Leduc et al., 2007) and at any instance static motors generate counterforce to oppose the motility by active motors. To examine how is the negative interference negated for an ensemble of membrane-anchored motors we determine the forces encountered by a microtubule and membrane-anchored motor proteins in the nanoscopic set-up.

For estimation of forces experienced by the individual components in the gliding set-up it is important to understand the alignment and geometry of the set-up (fig. 2.8 A). The phospholipids in the SLB cover the two-dimensional space on a glass coverslip with the height of approximately 5 nm. SLBs on a solid substrate have a thin aqueous layer of about 1 nm thickness, which is established between the substrate and the hydrophilic head groups of phospholipids due to electrostatic interaction (Nagle et al., 2000). The SLBs are functionalized with 1 % DSPE-PEG (2000)-Biotin. At this low density of functional lipids, the PEG (2000) linker would be in mushroom form with a radius of about ~ 3.5 nm, pointing towards the solvent as it is not attracted to the lipid bilayer (C. Allen et al., 2002). Biotin from the functional lipid will then attach to streptavidin, a homo-tetrameric protein having molecular weight of 52.8 kDa and a size of about 5 nm (Kuzuya et al., 2008). Streptavidin with its four binding pockets has 3 of its binding pockets vacant even after binding to a biotin molecule. It binds to a SBP tag of rKin430-SBP by simultaneously interacting with two of its biotin binding pockets, implying that any instant only one of the SBP tag of the dimeric rKin430-SBP can bind to a streptavidin attached to a biotin. SBP tag binds to streptavidin with a K_d of ~ 2.7 nM (Barrette-Ng et al., 2013). It has been shown that a surface immobilized kinesin-1 propels a microtubule with a height ~ 20 nm above the surface (Kerssemakers et al., 2006).

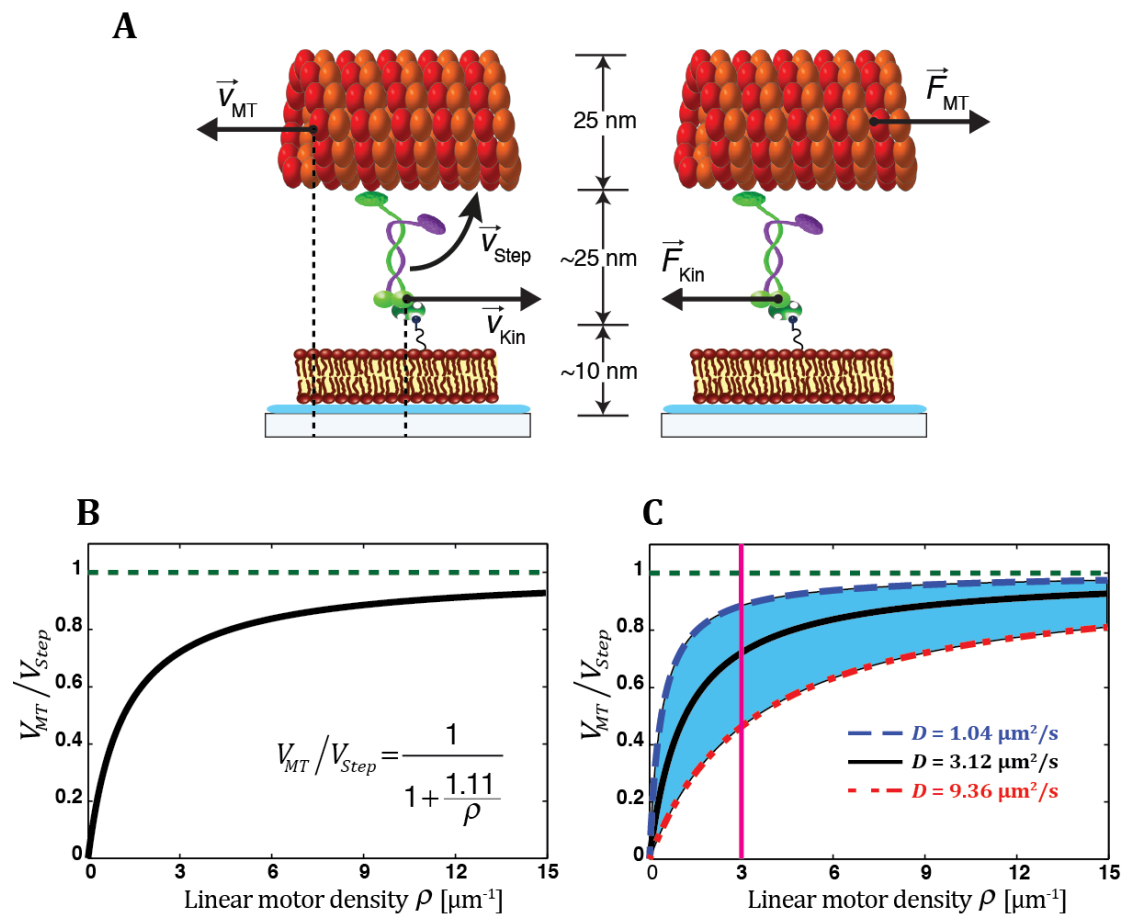


Figure 2.8 | Theoretical model for membrane-anchored gliding predicts dependence of gliding velocity on motor density and motor diffusivity. A) Nanoscopic view of the experimental set-up with the physical parameters, which are used in the model, in vectorial notations B) Model curve showing the dependence of relative microtubule gliding velocity on linear density ρ of the motors C) Model curves showing the effect of diffusivity of motors in the bilayer on the relative gliding velocity of microtubules, for three different D_{Kin} $1.04 \mu\text{m}^2/\text{s}$ (dashed blue line), $3.11 \mu\text{m}^2/\text{s}$ (solid black line) and $9.36 \mu\text{m}^2/\text{s}$ (dashed red line). Vertical line (magenta) is drawn as a guide to eye to see the effect of diffusivity on gliding velocity at a moderate density of 3 motors per unit length of a microtubule.

The following theoretical description is based on the Diploma work of Janine Fischer in our lab, which was completed in 2010 (Fischer, 2010).

Three main assumptions were made to resolve the dynamics of membrane-anchored gliding assays:

- (i) The microtubule is propelled by a motor stepping on it with a velocity \vec{v}_{Step} . Due to which the microtubule glides with a velocity \vec{v}_{MT} relative to the substrate in a direction opposite to the stepping motor. As the motor is not rigidly bound but attached to a fluid bilayer it moves on the SLB under the gliding microtubule with a reduced velocity \vec{v}_{Kin} relative to the substrate.

$$\vec{v}_{MT} = -(\vec{v}_{Step} - \vec{v}_{Kin}) \text{ or } \vec{v}_{Step} = |-\vec{v}_{Kin}| + |\vec{v}_{MT}| = \vec{v}_{Kin} + \vec{v}_{MT} \quad (2.2)$$

- (ii) The kinesin steps on the microtubule at maximum stepping velocity \vec{v}_{Step} . The stepping velocity for kinesin-1 is dependent on the external force against the motor, with a single kinesin-1 completely stalling at an external force of ~ 6 pN (Visscher et al., 1999). By estimating the maximum drag force on kinesin-1, based on the measurement of its diffusivity in the lipids, we can verify this assumption.
- (iii) The microtubule – motor system is investigated at the equilibrium of forces. This implies that the velocity of microtubule \vec{v}_{MT} and that of motor \vec{v}_{Kin} with respect to the substrate are constant and the net force acting on system is zero. The external force acting on a microtubule \vec{F}_{MT} is hydrodynamic drag caused due to its motion in the aqueous solution. The external force acting on a kinesin motor \vec{F}_{Kin} would be sum of the drag forces from the aqueous solution and from the fluid bilayer. At any instance there would be several motors interacting with a microtubule. Thus N motors stepping in an uncorrelated manner with the velocity \vec{v}_{Step} on a microtubule would experience equal drag force. The force balance equation would yield the relation:

$$N \cdot \vec{F}_{Kin} + \vec{F}_{MT} = 0 \quad (2.3)$$

To estimate the upper bound of the frictional force on microtubule as well as for the motors we take the upper limit of stepping velocity \vec{v}_{Step} as $1 \mu\text{m/s}$.

Frictional force on a gliding microtubule can be estimated by considering it as a long rigid cylinder with its length much greater than its radius $L_{MT} \gg r_{MT}$. Length of microtubules used in the experiments is more than 100 fold higher than its radius of 12.5 nm. The drag coefficient for cylindrical objects moving parallel to the surface is

$$\gamma = \frac{2\pi\eta L_{MT}}{\ln(2h/r_{MT})} \quad (2.4)$$

The magnitude of the force on the microtubule can be determined by Stokes' Law:

$$\vec{F}_{MT} = \gamma \cdot \vec{v}_{MT} = \frac{2\pi\eta L_{MT}}{\ln(2h/r_{MT})} \cdot \vec{v}_{MT} \quad (2.5)$$

A microtubule would experience maximum drag force when its moving at highest velocity which is $\vec{v}_{MT}^{max} = 1 \mu\text{m/s}$ calculated from equation (2.2) considering \vec{v}_{Step} as $1 \mu\text{m/s}$ and $\vec{v}_{Kin} = 0$. Thus for $\eta = 10^{-3} \text{ Pa}\cdot\text{s}$ (water), $L_{MT} = 10 \mu\text{m}$, $h = 50 \text{ nm}$ and $r_{MT} = 12.5 \text{ nm}$. The maximum force on a microtubule would be $|\vec{F}_{MT}^{max}| = 30 \text{ fN}$. The magnitude of maximum drag force on a microtubule in aqueous environment is 200-folds less than the stall force of single kinesin-1 motor. This is the reason, why the microtubule gliding velocity is independent of motor density for surface-immobilized motors with torsion compliance. Even a single motor can drive a microtubule at maximum velocity.

Frictional force on a membrane-anchored motor can be estimated by using the Einstein-Smoluchowski-relation where the drag coefficient is related to the diffusivity of a molecule by

$$\gamma = \frac{k_B T}{D_{Kin}} \quad (2.6)$$

The magnitude of the force then can be determined by

$$\vec{F}_{Kin} = \gamma \cdot \vec{v}_{Kin} = \frac{k_B T}{D_{Kin}} \cdot \vec{v}_{Kin} \quad (2.7)$$

Single membrane-anchored kinesin would experience a maximum drag force when its slipping under a stationary microtubule at its maximum stepping velocity, which is $\vec{v}_{Kin}^{max} = 1 \mu\text{m/s}$ calculated from equation (2.2) considering \vec{v}_{Step} as $1 \mu\text{m/s}$ and $\vec{v}_{MT} = 0$. For $k_B = 1.38 \times 10^{-23} \text{ J/K}$, $T = 295 \text{ K}$ and the $D_{Kin} = 3.11 \mu\text{m}^2/\text{s}$, as calculated previously from the SPT measurements of rKin430-SBP-GFP on SLBs. However, when interacting with a microtubule, the mobility of motor is reduced to only one dimension since the truncated construct rKin430-SBP is torsionally rigid and the motor heads walk on a single protofilament of a microtubule. Hence, the drag on a motor would double reducing the diffusion coefficient to half $1.56 \mu\text{m}^2/\text{s}$. The maximum force on such a motor would be $|\vec{F}_{Kin}^{max}| = 2.6 \text{ fN}$.

The maximum force experienced by a membrane-anchored motor is 250 times smaller than a stall force for a single kinesin-1 motor. This validates our second assumption that the motors will be driving a microtubule by stepping on it at a maximum velocity, similar to no external load condition.

By substituting the expression of forces for microtubule and kinesin motor in the equation (2.3) we get a relation

$$N \cdot \frac{k_B T}{D_{Kin}} \cdot \vec{v}_{Kin} + \frac{2\pi\eta L_{MT}}{\ln(2h/r_{MT})} \cdot \vec{v}_{MT} = 0 \quad (2.8)$$

which can be simplified as

$$\vec{v}_{MT} = -N \cdot \frac{\frac{k_B \cdot T}{D_{Kin}}}{\frac{2\pi\eta L_{MT}}{\ln(2h/r_{MT})}} \cdot \vec{v}_{Kin} \quad (2.9)$$

\vec{v}_{Kin} can be substituted in the above equation as $\vec{v}_{Step} - \vec{v}_{MT}$ from equation (2.2), yielding a relation

$$\frac{\vec{v}_{MT}}{\vec{v}_{Step}} = -\frac{1}{1 + \frac{f}{\rho}} \quad (2.10)$$

where $\rho = N/L_{MT}$ is the number of motors interacting with a microtubule per unit length or linear motor density, and

$$f = \frac{2\pi\eta \cdot D_{Kin}}{\ln(2h/r_{MT}) \cdot k_B T} = 1.11 \mu\text{m}^{-1} \quad (2.11)$$

From the force-balance consideration between a microtubule and the motors we could derive a relationship between the microtubule gliding velocity and the linear motor density. From the above relation we can deduce the following:

- (i) Microtubule gliding velocity, for a membrane-anchored motility, would increase with increasing motor density to an asymptotic value of velocity equal to \vec{v}_{Step} (fig. 2.8 B). At higher motor density, several motors will share the load to counterbalance the drag force of a microtubule. Therefore, even at very low value of \vec{v}_{Kin} of individual motors the collective drag force of several motors will be large enough to counterbalance the drag force of microtubule in the solution. As a consequence \vec{v}_{MT} would be high since the sum of their velocities is equal to a constant value of \vec{v}_{Step} in our set-up (see equation 2.2).
- (ii) At a certain motor density the microtubule gliding velocity is independent of its length. The drag force for a microtubule would increase with its length but since the number of motors counterbalancing the drag would also increase in the same proportion, for a constant motor density, the effect would cancel each other. This implies that for membrane-anchored gliding motility experiments with a uniform distribution of motors on a SLB all the microtubules will glide at same velocity independent of their length.
- (iii) Diffusivity of membrane affects the microtubule gliding velocity. The fluidity of membrane is inversely proportional to the drag coefficient. For a

constant number of motors, the membrane-anchored motors would slip faster on a highly diffusive lipid bilayer as compared to less diffusive bilayers. Thus \vec{v}_{Kin} would be high for highly diffusive membrane, resulting in a low microtubule gliding velocity \vec{v}_{MT} . In comparison, if the same number of motors are anchored in less diffusive membrane, they would slip back slowly thus resulting in a high \vec{v}_{MT} . The extreme situation is when the substrate is not diffusive at all, which is the case for a rigidly bound motors. Here, even a single motor can propel a microtubule at a velocity equal to maximum stepping velocity of individual motors. This is the reason for microtubule gliding velocity independent of motor density for rigidly bound motors.

The dependence of microtubule gliding velocity on linear motor density, for three distinct diffusion coefficients 1.04, 3.11, and 9.36 $\mu\text{m}^2/\text{s}$ of motors is shown in (fig. 2.8C). The lower diffusion coefficient corresponds to diffusivity of membrane in L_o phase and the higher value corresponds to diffusivity of membrane in liquid disordered (L_d) phase at physiological temperature of 310 K (Ries et al., 2009). Thus *in vivo* a cargo by modulating the fluidity of lipids, by varying lipid composition, can regulate its transport velocity.

2.5 Comparison of the gliding velocity between experiment and theory

Experimental data from gliding motility assays on membrane-anchored motors show the same trend for the velocity as obtained from the theoretical description. The theoretical model predicts that at any fixed motor density the gliding velocity will be independent of microtubule length. To analyze the effect of microtubule length on its velocity, we determined the mean velocity of microtubules, binned at the interval of 1 μm , for different motor concentrations (fig. 2.9A). The mean velocity and the mean diffusion coefficient of microtubule for each bin were calculated as described earlier, by fitting the cumulated MSD of microtubule trajectories with equation (2.1) (see Data analysis, chapter 5, page 121).

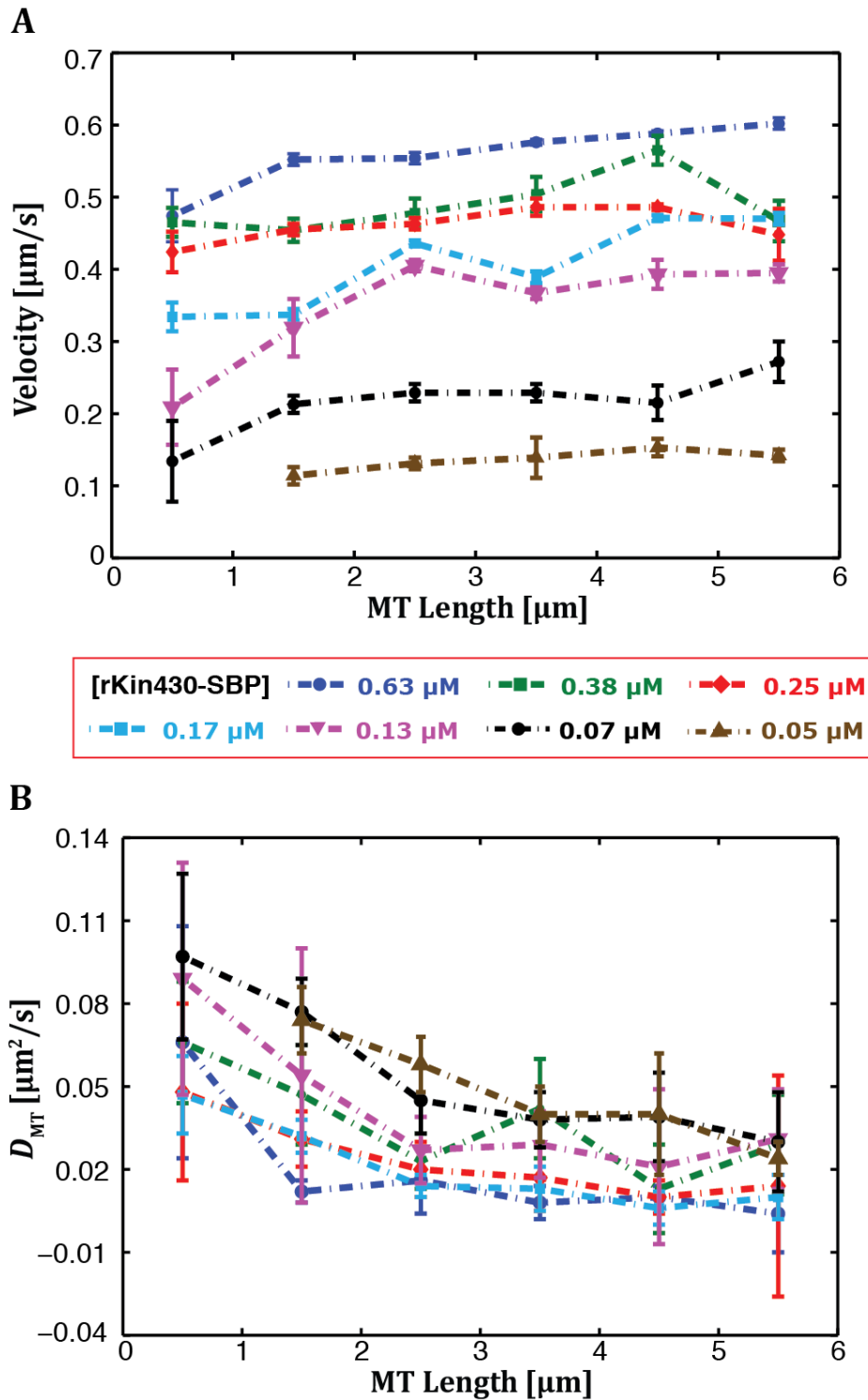


Figure 2.9 | Microtubule gliding velocities were independent of length and microtubule diffusivity decreased with increasing length, for all of the motor densities. A) Averaged microtubule gliding velocities B) Averaged microtubule diffusivity, for different microtubule lengths, binned into 1 μm intervals, at different motor concentrations 0.63 μM (blue), 0.38 μM (green), 0.17 μM (cyan), 0.25 μM (red), 0.13 μM (magenta), 0.07 μM (black), and 0.05 μM (brown). Error bar represents 95 % c.i. obtained from the fit. Dashed lines are drawn as a guide to the eye.

As predicted from the model, we did not observe a dependence of microtubule velocity on its length. However, for microtubules with length between 0-1 μm , first bin, the mean velocity was lower as compared to the longer microtubules.

At experimental time scales a longer microtubule reaches equilibrium, in contrast to the shorter microtubules, which have much wider spread of velocity indicated by the error bars for mean velocities for different microtubule lengths (fig. 2.9A). This can be explained by considering that for a particular motor density, the number of motors driving a microtubule at any instance would be determined by their binding kinetics with microtubules. A longer microtubule, having many binding sites, interacts with several motors at any instance and thus the stochasticity of a single motor binding/unbinding does not affect its motility very strongly. In contrast a shorter microtubule, which is driven by a less number of motors, would be strongly affected by the fluctuation in the number of motors interacting with a microtubule. The effect is more pronounced at lower motor densities for short microtubules. If we consider a simplistic scenario of a microtubule propelled by 5 motors and if 1 out of 5 motors unbinds, the drag on each motor increases by 25 % of the initial drag. In comparison if 2 motors drive a microtubule out of which 1 unbinds the drag on the motors increases 100 % of the initial drag. This stark increase in the drag force of motor would result in large fluctuations in the microtubule gliding velocity before the equilibrium is achieved again. Hence, from this analysis we can conclude that the shorter microtubules do not reach equilibrium at the experimental time scale. Since for our theoretical model we assumed an equilibrium condition, for further analysis we only took into consideration microtubules longer than 1 μm in length.

Diffusivity of microtubule (D_{MT}), decreases at higher motor concentration. This is because at higher motor density microtubule interacts with many motors, which reduces its mobility. The same effect can also be seen for D_{MT} as a function of length of microtubule (fig. 2.9B) for all the different motor concentrations. This is because of two factors (i) the longer microtubules would have more anchor points to pin it to the surface thereby decreasing its mobility (ii) the drag coefficient for a cylindrical object scales linearly with its length. This implies that

the ensemble average D_{MT} at different motor concentration would depend upon the length distribution as well as the motor concentration.

The theoretical model developed for the membrane-anchored gliding motility predicts the relative velocity of microtubule as a function of linear motor density and not the motor concentration. However, from the experiments we determined the gliding velocity as a function of amount of motors applied (bulk motor concentrations) to load them on the streptavidin bound functionalized lipids. Although, the trend and shape of the curve for gliding velocity obtained from model reflects well the experimental findings, it can be hypothesized that the bulk motor concentration is directly proportional to the motor density. But to examine how well does our theoretical model fit to the experimental data we have to make the independent variable - motor density, consistent between the theory and the experiment.

In order to extract actual surface density of motors we performed gliding motility assays on SLBs with a mix of labeled as well as unlabeled rKin430-SBP so called 'spiking assays'. The advantage of spiking experiments in comparison to using only labeled motors is the capability to resolve single molecule behavior over a wide range of motor densities. This is not possible by using rKin430-SBP-GFP at high concentrations. With the single molecule sensitivity of our imaging set-up we could determine the actual number of diffusing motors directly by counting. As compared to the indirect measurement based on total fluorescence intensity of GFP molecules, which can be skewed by several factors such as TIRF angle, optical aberrations, GFP clusters in the sample etc.; direct measurement is more convenient and robust.

From the gliding motility experiments for surface immobilized motors, and for membrane-anchored motors we could deduce that both the kinesin-1 constructs rKin430-SBP and rKin430-SBP-GFP are functionally similar. Thus rKin430-SBP spiked with rKin430-SBP-GFP could be used in the spiking experiments. We incubated streptavidin bound SLBs, with rKin430-SBP mixed with rKin430-SBP-GFP, in a fixed molar ratio of 150:1 at different bulk concentrations. The images

of the rKin430-SBP-GFP diffusing on the SLBs were recorded. Average number of GFP molecules diffusing on SLBs per unit area, was determined by counting the number of diffusing particles in first three frames to avoid errors in counting due to photobleaching (see Determination of motor density, chapter 5, page 125). Gliding motility assays were also performed on the same samples to obtain the microtubule gliding velocity, for a directly measured surface density. Therefore, we could avoid influence of random errors such as uncertainty in the protein concentration, total sample volume, sample inhomogeneity and systematic errors such as non-functional motor protein in our measurements.

Membrane-anchored gliding assays performed with rKin430-SBP spiked with rKin430-SBP-GFP, enabled us to observe single motors slipping under a microtubule while propelling them forward. At high motor density a microtubule, driven by several motors, moves fast while the motors propelling it slip backwards slowly (fig. 2.10A). However, at lower motor density, when only a few motors are propelling a microtubule, they slip backwards at higher velocity while the microtubule moves forward slowly (fig. 2.10B). This situation is more distinguishable when a fast moving microtubule encounters an obstacle; in our experiments another passing microtubule acts as an obstacle. When a propelling microtubule is obstructed leading to a low gliding velocity, the motors underneath the microtubule start slipping backwards at high velocity (fig. 2.10C). This direct observation of motor slippage validates our first assumption, formulated as equation (2.2), used for developing the theoretical description of membrane-anchored gliding motility assay.

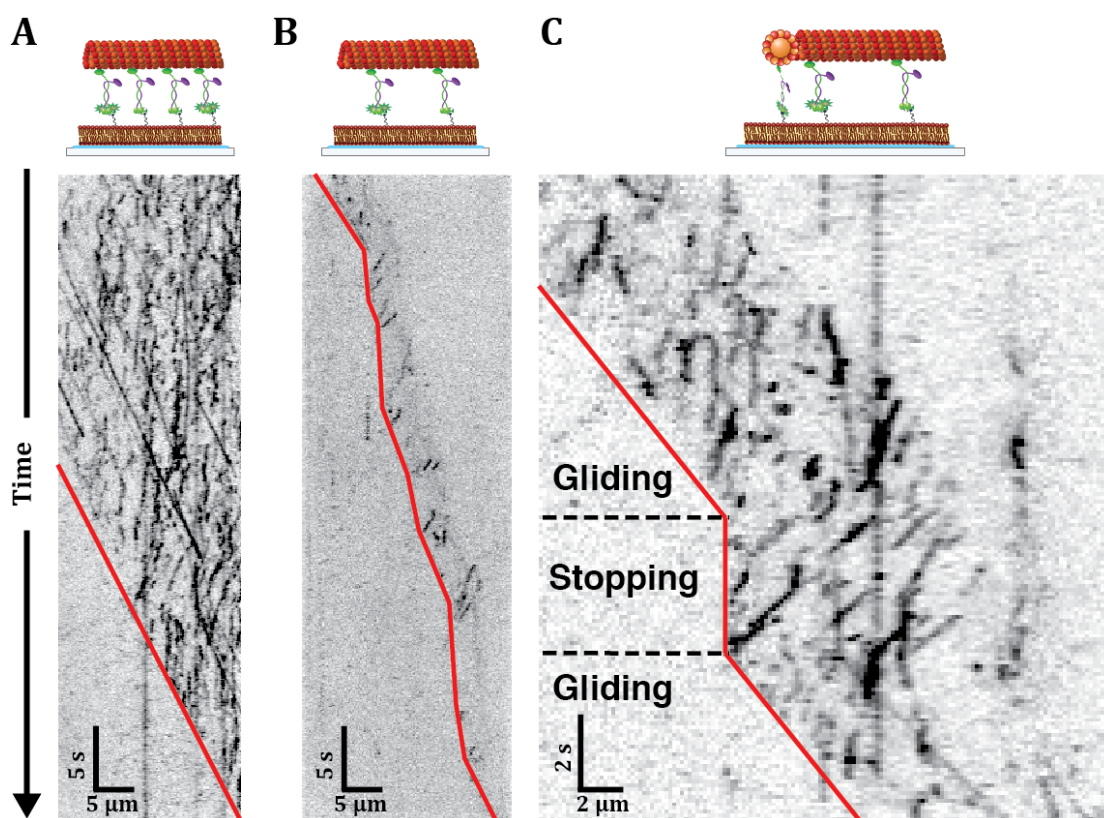


Figure 2.10 | Membrane-anchored kinesin-1 motors slip backwards, while propelling a microtubule forward. Representative kymographs of membrane bound rKin430-SBP-GFP (dark signals) while driving a microtubule forward in the spiking experiments. Three different scenarios of microtubule gliding are shown with schematic of event, on top of the kymographs. A) High motor density. B) Low motor density C) A gliding microtubule collides with another passing microtubule and stops until the other microtubule glide away. The red solid lines mark the trailing end of the microtubule as a guide to the eye.

Microtubule gliding velocity obtained from the spiking assays, for a measured motor density, followed the same trend as observed for the bulk motor concentration. We found out that the actual surface density of rKin430-SBP on the streptavidin loaded SLBs are sensitive to many factors such as the number of washing steps, waiting times after washing. Therefore, varying surface density could be obtained with the same bulk concentration by tuning these parameters. Nye et al. also reported similar results, where they investigated the kinetics of 6xHis and nickel-chelating lipids binding in an SLB. They demonstrated that the equilibrium between the His-tagged proteins and SLB is not reached at the experimental time scales (Nye et al., 2008). However, the K_d for SBP tag and

streptavidin is 1000-fold smaller than for His tag and Ni-NTA lipids, so we believe that equilibrium is reached in our experiments. Moreover, for further analysis, we used the data from spiking experiments where the surface density of motors was directly measured.

Gliding velocity, as a function of surface motor density was fitted with the modified equation (2.10)

$$\frac{\vec{v}_{MT}}{\vec{v}_{Step}} = -\frac{1}{1 + \frac{1.11}{\sigma \cdot \omega}} \quad (2.12)$$

Here, we assumed a linear relationship between the surface motor density on SLBs and the linear motor density, given by a relation (Duke et al., 1995)

$$\rho = \sigma \cdot \omega \quad (2.13)$$

where ω is the interaction reach of the motor to bind to a microtubule filament. The theoretical model, with only one free parameter, fitted well to our experimental data with the $R^2 = 0.999$ (fig. 2.11). From the fit we obtained the value of ω to be $0.31 \pm 0.07 \mu\text{m}$ (mean \pm 95% c.i.). The value of ω for kinesin motors immobilized on the surface is $\sim 20 \text{ nm}$. However, the reach of a diffusing kinesin motor would be much higher, as a kinesin-1 motor diffusing on a SLB with a D of $3.11 \mu\text{m}^2/\text{s}$ can explore a circle of radius $0.45 \mu\text{m}$ in 50 ms. Thus for our system the obtained value of ω is reasonable.

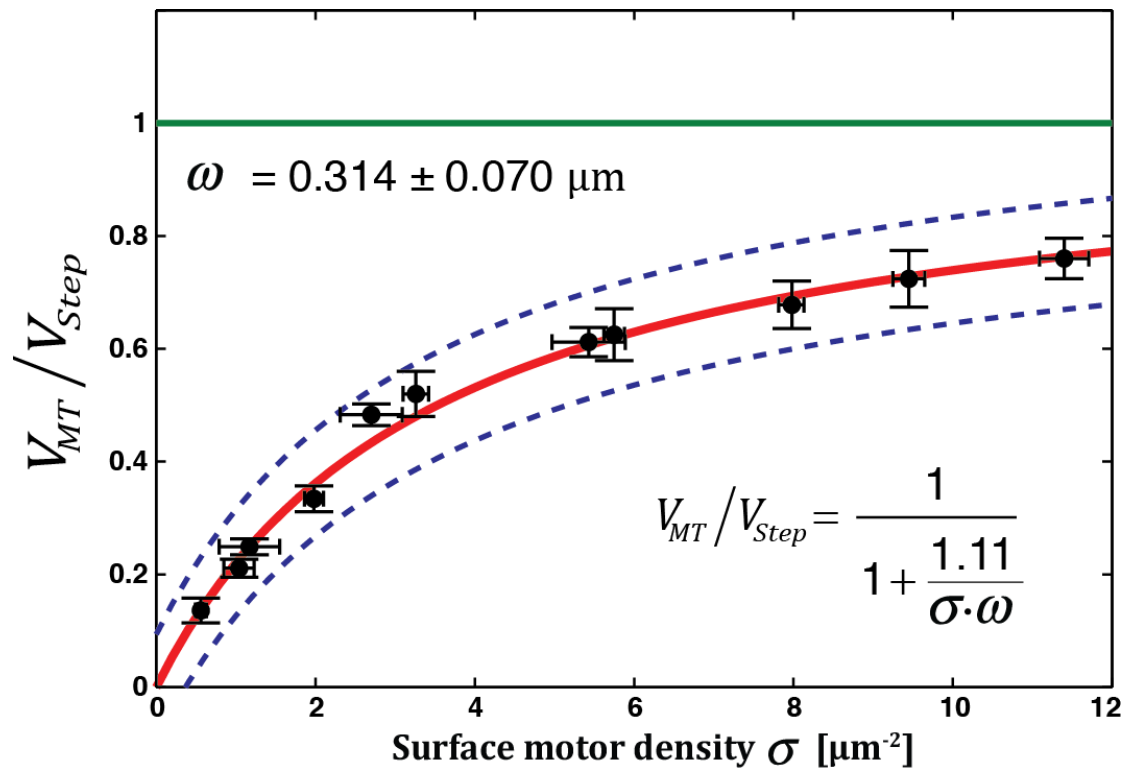


Figure 2.11 | Theoretical model, based on the frictional forces on microtubule and membrane-anchored motors, fits the experimental data well. Averaged microtubule gliding velocities as a function of measured surface motor densities in the spiking experiments are shown (solid black circles, mean \pm 95% c.i.). The data was fitted to the equation, with one free parameter ω , displayed at the bottom right. The fit (solid red line) and the 95% c.i of the fit (dashed blue line) are shown.

2.6 Gliding motility on phase-separated SLBs

The theoretical model predicts that at one motor density, the microtubule gliding velocity increases with decreasing substrate diffusivity.

We investigated the effect of lipid bilayer diffusivity on gliding microtubule velocity, by linking motors to the phase-separated SLBs. DOPC:Spingomyelin (SM):Cholesterol lipid mixture have been widely used for the formation of phase-separated domains in the model membrane systems such as SLBs. Whereby, SM and cholesterol partition into liquid-ordered (L_o) domains which are distinct from the fluid liquid-disordered (L_d) domains consisting of unsaturated lipids. The diffusivity of lipids in the L_o phase is 10 folds lower than that of L_d phase (Chiantia et al., 2006; Ries et al., 2009). Occurrence of two distinct domains with

such marked difference in diffusivity on the same surface provided us with a system to investigate the effect of microtubule gliding velocity on the diffusion of kinesin motors. Gliding motility experiments were performed on 1 % biotinylated phase separated SLBs (see SLB formation, chapter 5, page 116). The phase separation in the SLBs formed was confirmed by the partition of DOPE Atto647n dye in the L_d phase. The lipid marker is excluded from the L_o phase, as it has unsaturated acyl chains. Thus with the lipid marker we could clearly distinguish between the two phases, which was important for separating the microtubule trajectories as gliding over less fluid L_o and fluid L_d phase.

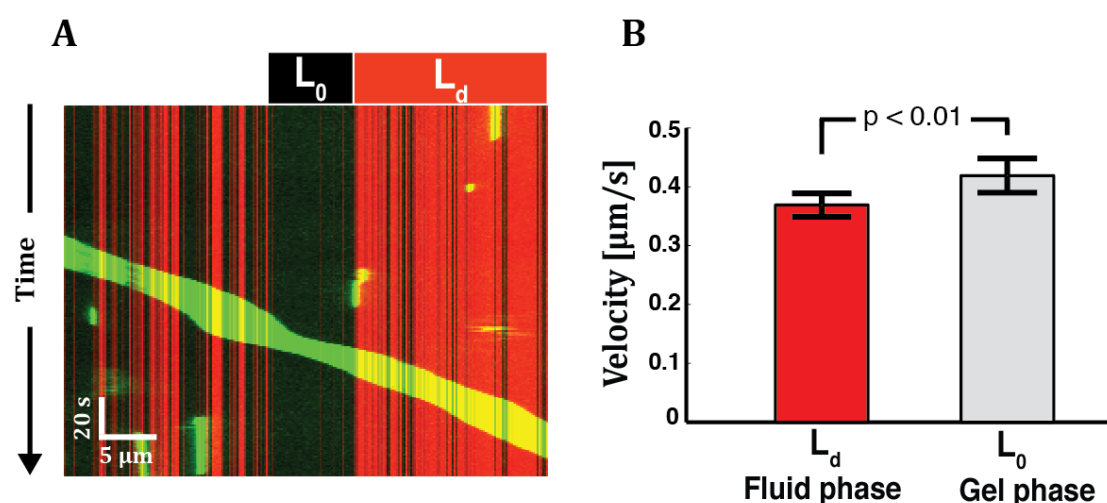


Figure 2.12 | Microtubules are propelled faster on L_o phase as compared to L_d phase, by motors bound to a phase-separated SLB. A) Representative multichannel kymograph of rhodamine labeled microtubule (green) gliding over gel L_o (black) and fluid L_d (red) domains of a phase separated 1% biotinylated SLB. DOPE-Atto647n is used as a lipid marker. B) Bar graph showing the averaged gliding velocity (mean \pm s.e.m.), for microtubules gliding over L_d (red, $n = 58$) and L_o (grey, $n = 35$) phase. The difference in the gliding velocity obtained for the two phases was statistically significant with a p value < 0.01 , determined from unpaired two-tailed t-test.

A gliding microtubule traversed over both the phases, indicating that the biotinylated functional lipids, to which the motors were attached, doesn't partition completely into any particular phase. We could observe an increase in the velocity of microtubule when it crossed from an L_d phase to L_o phase (fig. 2.12A).

The gliding velocity while microtubule traversed over the L_o phase 0.42 ± 0.03 (mean \pm s.e.m., $n = 35$) was significantly higher than on the L_d phase $0.37 \pm .02$ (mean \pm s.e.m., $n = 58$) (fig. 2.12B). However, the increase in the velocity was not as high as predicted from our theoretical model for a 10-fold decrease in the diffusivity. This could possibly be attributed to differential motor density in each phase due to unequal partitioning of biotinylated lipid in two phases, although they were subjected to same motor concentration. Since the experiments were performed with the unlabeled rKin430-SBP, so actual surface motor density for two phases could not be resolved. We know from our experiments on fluid SLBs that motor density plays a critical role in determining the gliding velocity of microtubule. Higher density in the L_o phase can compensate for its higher diffusivity, resulting in higher gliding velocity. Therefore, the next step would be to obtain the surface density of motors in two phases. In our initial experiments, we could show that gliding motility assays can be reconstituted even on the phase separated lipid bilayers. This opens up an interesting avenue to investigate the motility behavior of collection of different motors, which might have a preference for one phase or the other depending upon their lipid binding domains or scaffold proteins by which the motors attach to a cargo.

2.7 Discussion

In this chapter, we investigated the transport characteristics of multiple kinesin-1 motors linked to diffusive lipid bilayers, by performing gliding motility assays on kinesin-1 attached to SLBs. For this purpose, diffusive and homogenous DOPC SLBs, functionalized with biotinylated lipids were formed on a glass substrate. The diffusion coefficient of lipids in SLBs was obtained to be $\sim 3 \mu\text{m}^2/\text{s}$. This value matches well with the reported values of diffusion coefficient for SLBs formed on glass, with similar lipid compositions, in literature (Machan et al., 2010; Braunger et al., 2013). By single molecule imaging of rKin430-SBP-GFP in TIRF microscopy, we confirmed that the motors bind to SLBs and diffuse with diffusion coefficient $3.11 \mu\text{m}^2/\text{s}$, similar to that of lipids in SLBs. In addition, the diffusivity of motors was independent of the motor concentration on SLBs, confirmed by the spiking assays (data not shown). rKin430-SBP is linked to the

head group of lipids, via a long PEG chain, and not integrated in the lipid bilayer. Thus, motors do not affect the lipid diffusivity and the diffusivity of rKin430-SBP is governed by the diffusivity of lipids in the SLB. This is consistent with the theoretical framework of Saffman and Delbrück, and the experimental evidence indicating that the lateral mobility of peripheral proteins on lipid bilayer is insensitive to their dimensions (Saffman et al., 1975; Knight et al., 2010). Thus, by linking SBP tagged kinesin-1 motors to biotinylated SLBs via streptavidin, we were able to reconstitute microtubule gliding driven by diffusive motors.

Slippage of membrane-anchored motors: We observed membrane-anchored kinesin-1 motors slip backwards, while propelling a microtubule forward. Thus of the total distance that a motor head moves relative to a microtubule, a part of the distance is translated into movement of microtubule in the solution and the rest is translated into movement of anchor point in the viscous membrane, in the reference frame of solid substrate. Thereby, as kinesin-1 steps towards the plus-end of microtubule, it will drag its membrane-anchor along with it through the viscous membrane, at the same time pushing the microtubule in the opposite direction (fig. 2.13). Thus, the microtubule gliding velocity is given by the difference of the motor stepping velocity and the slipping velocity. For instance, if the motor slipping velocity is zero, as in the gliding motility assays on rigidly bound motors, the microtubule velocity is equal to the stepping velocity of motor. In other case, if the microtubule velocity is zero, as is the case for stepping motility assay where the microtubules are fixed on the surface, the motor slipping/walking velocity is equal to the stepping velocity.

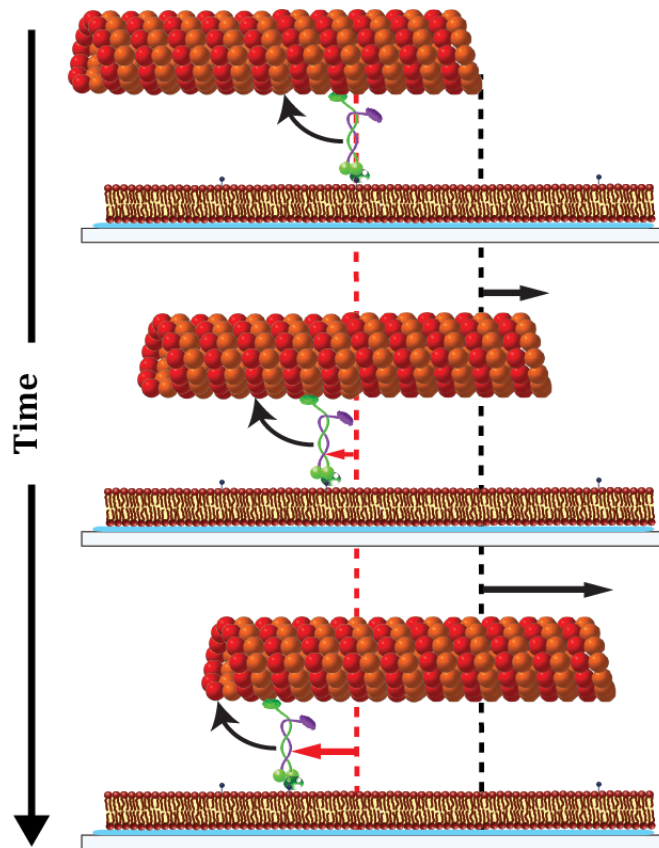


Figure 2.13 | Schematic diagram of membrane-anchored motor slipping while propelling a microtubule. Membrane-anchored motors move their anchor points in the membrane while stepping on a microtubule. As a consequence, the microtubule is propelled in the opposite direction at a velocity lower than the maximal stepping velocity of individual motors. Time is progressing from top to bottom, while the motor moves from right to left, microtubule is propelled in the opposite direction.

Frictional forces: By analyzing the frictional forces on microtubules and membrane-anchored motors, we could obtain their corresponding transport velocity. The motor stepping velocity and the slipping velocity determine microtubule gliding velocity, for motility on membrane-anchored motors. The stepping velocity of a kinesin-1 motor is dependent on the external load, with decreasing velocity at higher loads (Visscher et al., 1999). The movement of motor anchor point in the lipid bilayer and the motility of microtubule in the solution are resisted by the frictional drag, which is proportional to their velocity in the medium according to the Stoke's law. For membrane-anchored motors the external load is the frictional drag exerted due to movement of the anchor point in the viscous lipid bilayer. The maximum drag force experienced by individual membrane-anchored rKin430-SBP, moving at $0.67 \mu\text{m/s}$ in a lipid bilayer with

1-D diffusivity $1.56 \mu\text{m}^2/\text{s}$, is $\sim 1.7 \text{ fN}$. As the drag force is three order of magnitudes lower than the stall force (6 pN) of single kinesin-1, the motor stepping velocity in our system is constant equal to the maximal stepping velocity of rKin430-SBP (Hunt et al., 1994). The maximum drag force experienced by a microtubule (length = $10 \mu\text{m}$) in the solution, assuming it moves at the maximal velocity of $0.67 \mu\text{m}/\text{s}$, is $\sim 20 \text{ fN}$. Therefore, the maximal drag exerted on a microtubule is ~ 10 times higher than the maximal drag on a single motor, hence it is easier to drag an anchor point in the lipid bilayer as compared to move the microtubule through the solution. However, if we consider several membrane-anchored motors propelling a microtubule, there collective drag force could be as high as a microtubule. Thus the velocity at which microtubule is propelled in comparison to the slipping velocity of membrane-anchored motors, depends on the ratio of frictional forces incurred by their movement. And at steady state, these forces will balance each other, which give us the basis of cooperativity for membrane-anchored gliding motility assays.

Non-crossing of microtubules: In the membrane-anchored gliding motility assays for kinesin-1, the microtubules upon collision do not cross each other. In contrast, the microtubules, propelled by kinesin-1 immobilized on glass, cross over each other without any noticeable effect. The mechanism for crossing of microtubules over an obstacle, in gliding motility assays on surface-immobilized kinesin-1, has been very well explained in the study by (Kerssemakers et al., 2009). In brief, leading tip of a microtubule, which is not fixated to the surface by motor, is free to fluctuate due to thermal agitation. In the z-plane the fluctuations have an upward bias because of the surface constraints. Thereby, the microtubules are pushed over another passing microtubule by the force of propelling motors.

The non-crossing of microtubules upon collision, for membrane-anchored gliding could be due to following reasons (i) the fluctuation of the leading end is curtailed due to unspecific interaction with the surface, i.e. with the SLBs or streptavidin, (ii) kinesin-1, linked to a lipid bilayer, can't propel microtubules with a force high enough to push over another microtubule. We found out that the microtubules attached to the streptavidin-loaded biotinylated SLBs in

unspecific manner. However, the unspecific interaction between the microtubules and streptavidin was shielded when rKin430-SBP was bound to the streptavidin-loaded biotinylated SLBs, as we didn't observe any stuck microtubules in membrane-anchored gliding motility assays, for all the different motor densities. In addition, we didn't observe buckling of microtubule when colliding with another passing microtubule. It has been shown that even a single kinesin-1 can generate enough force to buckle a microtubule, which is stuck at its leading end (Gittes et al., 1996). However, in membrane-anchored gliding assay when the leading tip of a microtubule is stuck, for example when colliding with another passing microtubule, the motors slip backwards due to low drag in the lipid bilayer and doesn't generate enough compressive force to buckle a microtubule. From the frictional force analysis, we know that the maximum external load on the motor to move its anchor in the lipid is only 2.7 fN. This force is probably much less than what would be required to push a microtubule over another passing microtubule. Considering we did not observe microtubule crossing even at high motor density of $4 \mu\text{m}^{-1}$, even for 15 μm long microtubule, the force required for pushing a microtubule over another microtubule is greater than 0.16 pN, which is still much less than maximum stall force of a single kinesin-1 motor. Thus even a single surface-immobilized kinesin-1 motor can push over a microtubule over another microtubule, however it would require a very high number of membrane-anchored kinesin-1. Non-crossing microtubule gliding behavior has been demonstrated for axonemal dynein (dynein c from *Chlamydomonas* flagella) (Sumino et al., 2012) but has not been reported for kinesin driven gliding motility assays. However, Sumino et al. did not explain the reason for non-crossing of the microtubule upon collision.

We postulate that the non-crossing of microtubules gliding over membrane-anchored rKin430-SBP attached to biotinylated SLB via streptavidin is primarily because of the low force output of kinesin-1 to push a microtubule over another microtubule, which could be assisted by an added interaction of the microtubule with the substrate, such that the fluctuation of the tip is restricted. This hypothesis can be tested in the future by measuring the maximum force, using an optical trap, that is required to stall a gliding microtubule, propelled at different densities of membrane-anchored motors.

Cooperative effects in transport by membrane-anchored motors: For the membrane-anchored gliding motility assays, microtubule gliding velocity increases with increasing motor density. Both surface motor density and corresponding microtubule gliding velocity were experimentally measured, by performing spiking membrane-anchored motility assay. The experimental data is in agreement with the theoretical model, which was formulated based on the fact that at steady state the net force on the transport system, comprising of microtubule and membrane-anchored motors driving the microtubule, is zero. Thereby, the collective drag force exerted on several motors, due to movement of their anchor in the viscous lipid bilayer, balances the drag force on the microtubule, due to its movement in the solution. At low motor density, the motors have to move their anchor points in the lipid bilayer faster to balance the drag force of the microtubule in the solution. This results in a higher slipping velocity and thus microtubule gliding velocity, significantly lower than the stepping velocity of the individual motors. However, at high motor density, even at lower slipping velocity the collective drag force exerted on the motors is high enough, to balance the drag force on a microtubule moving at higher velocity. As a result of lower slipping velocity, microtubules are propelled at higher velocity close to the maximal stepping velocity of individual motor. For surface immobilized rKin430-SBP, we observed gliding velocity much lower than the maximal stepping velocity of individual motor, which can be attributed to the negative interference of multiple motors that step asynchronously and hence inhibit each other at higher density when collectively transporting a microtubule (Bieling et al., 2008; Crevenna et al., 2008). In contrast, anchoring of motors to a lipid bilayer provides flexibility to the system such that the multiple motors don't impede each other and rather induces cooperative behavior, where high motor density is required to transport a microtubule at maximal velocity.

Diffusivity of lipid-bilayer: The gliding behavior of microtubules is dependent on the frictional forces, hence, the diffusivity of the lipid bilayer and thus the anchored motors is crucial in determining the transport velocity. Motors anchored to a less diffusive lipid bilayer encounter more drag while moving their

anchor point in the lipid bilayer. Thus, the drag force on a small number of motors slipping at low velocity is sufficient to balance the drag of the microtubule moving in the solution. As a consequence, for the same motor density, microtubules glide faster on motors anchored to less diffusive lipid bilayer as compared to more diffusive lipid bilayer. This effect was exhibited for gliding motility on motors anchored to phase separated SLBs, where gliding velocity was faster when microtubules passed over lipid-ordered phase as compared to lipid-disordered phase.

Our theoretical model quantitatively describes the co-operative effects in the transport system driven by membrane-anchored motors. By fitting the experimental data of microtubule gliding velocity and surface motor density to the model, we could determine the isotropic reach of diffusing motors to interact with a microtubule. For rKin430-SBP diffusing on SLBs with a diffusivity of $3 \mu\text{m}^2/\text{s}$, we obtained the value of $0.3 \mu\text{m}$, which is 10 folds higher than what is assumed for rigidly bound kinesin-1 (Duke et al., 1995; Van den Heuvel et al., 2007). In addition, the model can be used to predict the number of motors involved in transport of a microtubule based on its gliding velocity.

In this chapter, a novel *in vitro* approach was developed to understand the collective transport behavior of membrane-anchored motors. We used chimeric construct of kinesin-1 motors with SBP tag that can be synthetically linked to a biotinylated SLB via streptavidin. This approach mimics the recruitment of kinesin-1 (KHC) motors to its cargo inside a cell, where motors are linked to various cargos via membrane associated adaptor proteins, which attach to its tail or the accessory light chain KLC.

In the following chapter, we focus on investigation of transport characteristics of a motor protein KIF16B, which binds directly to its cargo with its inherent lipid-binding domain. The direct binding to cargo might influence the local lipid composition of a vesicle, whereby the specific lipids to which the motors are attached are not homogeneously distributed but clustered, forming microdomains due to their attachment to motors.

3 Transport by KIF16B with an inherent lipid-binding domain

KIF16B, a kinesin-3 subfamily motor, is a membrane associated motor protein. It has a phox-homology (PX) domain at its tail, which binds to PI(3)P with a K_d of 27 nM. It specifically attaches to early endosomes (EE), rich in the PI(3)P phospholipids, and move the receptor molecules endocytosed at cell periphery, where they are sorted to be either recycled back to the plasma-membrane or moved to lysosomes for degradation. Overexpression of KIF16B causes the relocation of EE to the cell periphery, while expression of dominant negative KIF16B or RNAi-mediated knockdown causes EE to cluster in the perinuclear region (Hoepfner et al., 2005; Blatner et al., 2007).

In recent *in vivo* studies, KIF16B transport characteristics have been investigated. Soppina et al. showed that in the wild type cells full-length (FL) KIF16B localize at the axon tip. However, a mutation in the PX domain of FL KIF16B, such that it can not bind to PI(3)P and hence EE, leads to a diffused localization of the KIF16B motors in a cell cytosol. This suggests that the cargo binding is essential for motor activity. They also performed single-molecule (SM) fluorescence studies with the cell extracts to show that KIF16B motors truncated to first coiled-coil (CC1) (1-455 a.a.) were monomeric and non-processive but motors truncated to neck coil (NC) (1-400 a.a), were dimeric and superprocessive with run-lengths of $\sim 10 \mu\text{m}$ on microtubules. These high processivity have not been reported thus far for any family of Kinesin motors (Soppina et al., 2014). Based on their findings they postulate that FL KIF16B is activated and dimerized upon binding to its cargo. Furthermore, the dimeric motor domains are intrinsically superprocessive. In another study performed with hippocampal neuron cell, Farkhondeh et al. demonstrated that KIF16B construct (1-810 a.a), lacking a part of its stalk and PX domain, localized at the axonal tip. This suggests that the motors are active and processive without binding to cargo via its PX domains. However, KIF16B construct (1-1096 a.a),

lacking only PX domain, showed diffused localization in the cell cytosol. This phenotype was similar to what is observed for FL KIF16B with a mutation in PX domain. They further performed biochemical assays to show that the amino acid (a.a.) sequence (810-1074) - 'stalk' binds to the motor domain of KIF16B to inhibit motor activity, in an ATP dependent manner. Taken together, their findings demonstrate that the KIF16B motors are auto-inhibited but processive without binding to cargo (Farkhondeh et al., 2015), which contradicts the mechanism of KIF16B activity proposed in the study by Soppina et al.

KIF16B mediated transport, thus far, has been studied *in vivo* or using cell extract, which elucidate the overall effect in the transport. However, the observations recorded in different experiments are contrary so they could be influenced by additional factors present in the complex environment of cell. To investigate the molecular mechanism of KIF16B transport, specifically the role of cargo attachment on transport behavior of motors, we followed the *in vitro* approach, where reconstituted purified KIF16B motors was characterized at SM level and multi-motor transport, in conjunction with membrane, was studied in a controlled environment.

The first section of this chapter details the expression and purification of different KIF16B motor proteins constructs that were used for the *in vitro* assays. The second section focuses on investigation of the transport characteristics of an individual KIF16B motor using SM stepping motility assays and multi-motor transport of KIF16B using conventional gliding motility assays. In the final two sections of this chapter we explore the collective effects in transport by KIF16B motors attached to a diffusive lipid bilayer via its inherent lipid-binding domain. To this effect we utilize different model membrane systems such as planar SLBs, SUVs and lipid coated silica beads (LCBs).

3.1 Expression and purification of KIF16B

To study the molecular mechanism of KIF16B transport, we purified various constructs of the human KIF16B motors. GFP tagged constructs were purified to

probe the motor-microtubule interactions at SM scale using TIRF microscopy. The truncated constructs, consisting of only motor domain, were prepared to study the biophysical characteristics of motor domain in isolation. Also chimeric constructs with PX domain of KIF16B were prepared to understand the effect of its lipid binding on the working of KIF16B. Full length (FL) KIF16B, GFP tagged FL KIF16B (KIF16b-GFP) and GFP tagged truncated KIF16B constructs motor head domain 1-400 a.a (16B-400-GFP) and 1-429 a.a, (16B-439-GFP) and chimeric constructs also tagged with GFP e.g. motor head with PX domain (16B-400-PX) and (16B-429-PX) were expressed and purified from the insect cells using baculoviral expression plasmids (pOCC) developed at the Protein expression and purification facility at MPI-CBG. KIF16B is a large protein and thus is not expressed well in the bacterial expression system; instead insect cell expression system was used to express different KIF16B constructs (see Protein expression and purification, chapter 5, page 105 for details)

Human KIF16B gene insert with 6xHis tag and enhanced GFP (eGFP) both on N-terminal (6xHis-eGFP-KIF16B) in pFastBac plasmid, a gift from Zerial lab MPI-CBG, was expressed in insect cells and purified with His tag affinity purification. However, SDS PAGE analysis of the cell extract as well as the purified fraction showed a lot of smaller molecular weight bands than the expected molecular weight of 182.7 kDa (fig. 3.1A). The western blot analysis using the antibodies against GFP also showed many bands of lower molecular weight than expected. This suggested that the protein was either partially expressed or was getting proteolytically degraded *in vivo* after expression. Even though, the lysis buffer was always supplemented with cocktail of protease inhibitors to minimize the proteolytic degradation after lysis. The problem persisted even after using freshly prepared virus stocks.

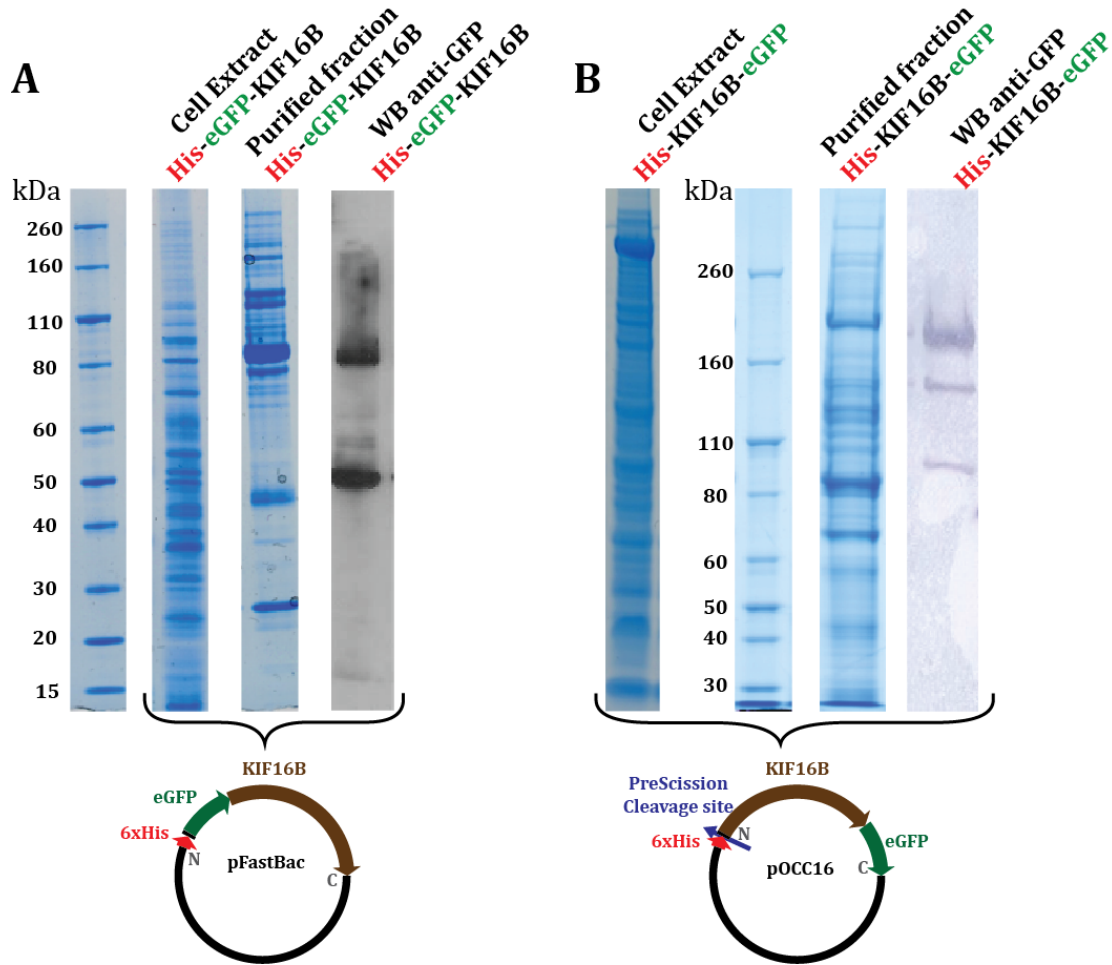


Figure 3.1 | Recombinant His tag FL KIF16B is degraded in the insect cell expression system. Whole cell extract and purified protein fraction on Coomassie stained gels for 6xHis FL KIF16B expressed in insect cells with two different vectors A) His-eGFP-KIF16B in pFastBac B) His-PreScission-KIF16B-eGFP in pOCC16. The last lane shows the western blot corresponding to the purified fraction for FL KIF16B, probed with an anti-GFP antibody. The expected molecular weight of FL KIF16B tagged with GFP and 6xHis tag is 182.5 kDa. The schematics of plasmids with inserts are shown below the gels.

To determine whether FL KIF16B was partially expressed or getting degraded after expression, the gene sequence was cloned into another vector backbone pOCC16 having an N-terminal 6xHis tag and a C-terminal eGFP tag (fig. 3.1B). The proteins are transcribed and translated from 5' to 3' end of DNA and respective mRNA, thus the N-terminal of the proteins are formed first and the C terminal is translated last. Two different tags at N and C terminal, allowed us to determine whether the protein is being expressed partially or fully, by performing western blot against 6xhis tag and GFP tag.

The insect cells expressing FL His-KIF16B-eGFP when seen under fluorescence microscope 48 hours post infection were green indicating that the FL KIF16B was fully expressed because GFP is present at the C terminal. By performing the SDS PAGE analysis of the purification we obtained a protein band corresponding to the molecular weight of FL KIF16B but considerable amount of FL KIF16B was still degraded, which could be seen in the SDS PAGE gel as well as in the western blot against GFP tag (fig. 3.1B).

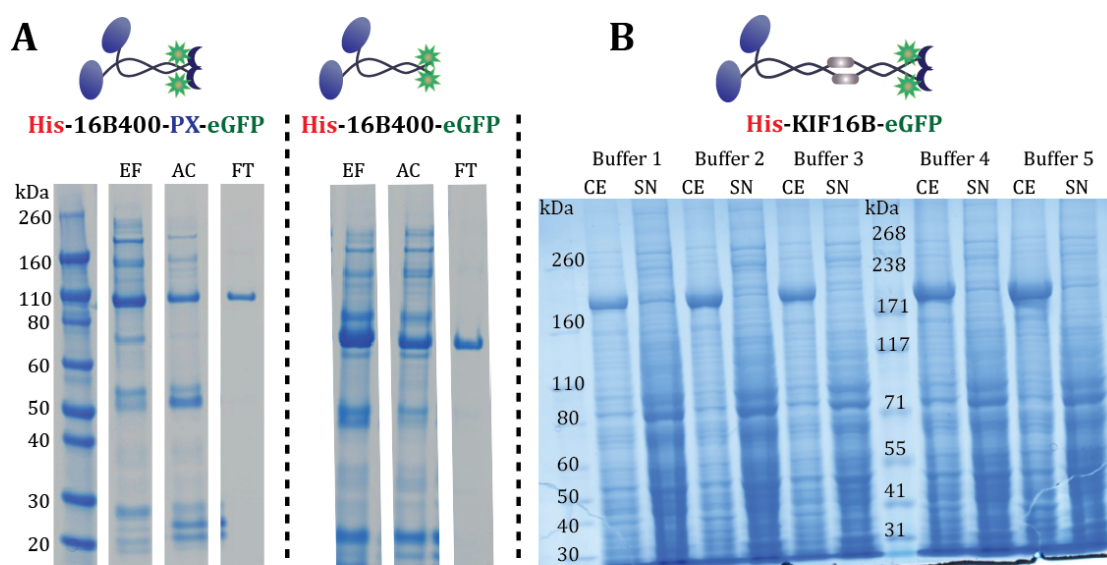


Figure 3.2 | Truncated KIF16B constructs were purified via His tag but FL KIF16B with His tag has low solubility. A) Purification of His tagged KIF16B shorter constructs. Coomassie stained gel showing eluted fraction (EF) from Ni-NTA column after affinity purification, fraction after cleaving (AC) the His tag with PreScission protease, and the flow through (FT) after re-binding the cleaved protein fraction to Ni-NTA resin. The expected molecular weight of 16B-400-PX and 16B-400 is 90 kDa and 72.1 kDa respectively. B) Coomassie stained gel showing whole cell extract (CE) and supernatant (SN) after ultra-centrifugation of cell lysate, in different lysis buffers 1: 100 mM Na₂PO₄, 300 mM NaCl; 2: 50 mM HEPES, 150 mM NaCl; 3: 50 mM HEPES, 300 mM NaCl; 4: 25mM HEPES, 600 mM NaCl; 5: 25 mM HEPES, 75 mM NaCl.

From the SDS PAGE analysis, we also found that amount of FL KIF16B in the cell extract was much higher than in the supernatant after the ultra-centrifugation of cell lysate, even at similar sample loadings, implying most of the protein was insoluble and getting pelleted with the cell debris. KIF16B is a membrane associating protein, because of its lipid-binding domain. Inside a cell there could be various factors, which stabilize the protein. In contrast affinity purified

KIF16B was insoluble, thus, buffer conditions have to be optimized to obtain functional motors. The purified proteins can form aggregates due to various factors, such as salt concentration, pH, which causes the proteins to fold incorrectly and attain conformation that are not functional. To check the solubility of 6xHis-KIF16B-eGFP we performed the cell lysis in different buffers varying the buffering agent and ionic strength (IS) of buffer by changing the salt concentration but we did not see any increase in the solubility of the His-KIF16B-GFP (fig. 3.2B). The pH of all the buffers used was set to 7.2, which is well above the theoretical isoelectric point (pI) 5.8 of His-KIF16B-eGFP based on its amino acid sequence, at which its net charge is neutral and the protein has higher probability to aggregate due to Vander wall interactions. This indicated that the salt concentration and IS of the buffer didn't influence KIF16B solubility. KIF16B with its lipid binding domains might be strongly attached to a membranous cargo via some ancillary proteins integrated in the membrane resulting in a low solubility of KIF16B after lysis. Hence, it might not be released in the solution as other cytoplasmic proteins and a considerable amount of KIF16B is pelleted along the cell debris on ultra-centrifugation. Thus, FL KIF16B in active form could not be purified with His tag affinity purification.

The gene sequence of shorter constructs was inserted in pOCC16 and they were expressed in insect cells, with a cleavable His tag at N-terminal. They were purified in two steps, first His affinity purification (see chapter 5, page 105 for details) was performed to remove major chunk of unspecific soluble proteins from the cell lysate; however, there were still a lot of other proteins that co-eluted with the protein of interest (fig. 3.2A). This could be due to naturally occurring two or three adjacent histadine residues in their structure, which is sufficient to bind to the His affinity column. To remove the protein fractions other than the protein of interest, a second purification step was performed in which the eluted fraction from the His affinity purification was first incubated with 6xHis-PreScission protease to cleave off the 6xHis tag from protein of interest. The solution with the protease, protein of interest and cleaved 6xHis tag was then incubated with Ni-NTA resin. This allowed re-binding of the other impurities, which were co-eluted with the protein of interest in addition 6xHis-

PreScission protease and the cleaved His tag would also bind to to the resin. This two-step purification resulted in a purified protein of interest with minimal impurities (fig. 3.2A).

To enhance the solubility of FL KIF16B and make it less averse to proteolytic degradation after its expression other tags were explored for its purification. A strategy often used in purification of insoluble proteins is their fusion to other soluble proteins such as maltose binding protein (MBP) or glutathione s transferase (GST). These highly soluble proteins help in solubilizing their fusion partners. The MBP tag fusion holds many advantages as compared to his tag as it makes the protein more soluble, stabilizes the protein from poteolytic degradation and usually provides higher yields and purity of the protein of interest (Kapust et al., 1999).

Thus, for the above-mentioned reasons FL KIF16B was cloned into another vector backbone pOCC112 having an eGFP followed by a maltose binding protein (MBP) at the C-terminal, with a PreScission cleavage site in between the two (fig. 3.3A) to remove the MBP after purification. MBP is a 42 kDa protein responsible for regulation of maltodextrins in *E. coli*. It has a natural affinity to the amylose resin, which can be used for one-step affinity purification. The MPB tagged proteins bind to a cross linked amylose resin and can be eluted thereafter with maltose in the elution buffer (P. Sun et al., 2011).

FL KIF16B, gene sequence inserted in pOCC112, was expressed in insect cells and purified with MBP affinity purification (see MBP affinity purification, chapter 5, page 107 for details). The fusion of FL KIF16B with an MPB tag increased its solubility and the protein could be purified with minimal impurities. The MBP tag was then cleaved off from the FL KIF16B using 6xHis-PreScission protease. It is often observed that after the cleavage of MBP tag the fusion partner aggregates, as the solubility is reduced. To circumvent the problem of protein aggregation we performed the cleavage reaction in high salt buffer 1 M NaCl, in presence of 0.5 M arginine. High salt helps in minimizing the unspecific protein-protein electrostatic interactions that might lead to aggregation. Arginine is one of the common additives used to prevent aggregation of purified recombinant

proteins (Arakawa et al., 2007). The cleaved protein fraction was further purified by gel filtration, using Superose 6 column, to separate KIF16B from MBP and PreScission protease. The column was calibrated with thyroglobulin 660 kDa and bovine serum albumin monomer 67 kDa. We observed four distinct peaks in the elution profile with absorption at 280 nm A_{280} and one distinct peak at 488 nm A_{488} the initial two peaks at 7 ml and 8 ml might correspond to some aggregates of proteins. The low molecular weight peak when analyzed with an SDS PAGE gel corresponded to the cleaved MBP.

FL KIF16b-eGFP started eluting after 11 ml with a peak at around 12 ml, this peak corresponded to the thyroglobulin peak of the standard so the apparent molecular weight for FL KIF16B was determined to be ~ 660 kDa (fig. 3.3 B). The absorbance peak A_{488} matches well to the A_{280} peak confirming that the protein eluted in these fractions was FL KIF16B-eGFP. When all the fractions under this peak were denatured and analyzed with an SDS-PAGE gel we observed a single protein band at around 180 kDa (fig. 3.3C) corresponding to the expected molecular weight of KIF16B-eGFP monomer. The higher apparent molecular weight of KIF16B dimer ~660 kDa as compared to the expected molecular weight for KIF16B-eGFP dimer ~360 kDa can be explained by the fact that the proteins elute from gel filtration chromatography based on their size as well as shape (Erickson, 2009). FL KIF16B is not a globular protein and has large coiled-coil regions (Hoepfner et al., 2005) whereas the calibration curve is prepared using the globular proteins. Because of the large coiled-coil regions the FL KIF16B is expected to have an elongated conformation and thus elute corresponding to higher molecular weight. In conclusion, KIF16B fusion to MBP proved to be an effective strategy to purify FL KIF16B motor, whereby the MBP tag can be cleaved after purification and removed with gel-filtration chromatography.

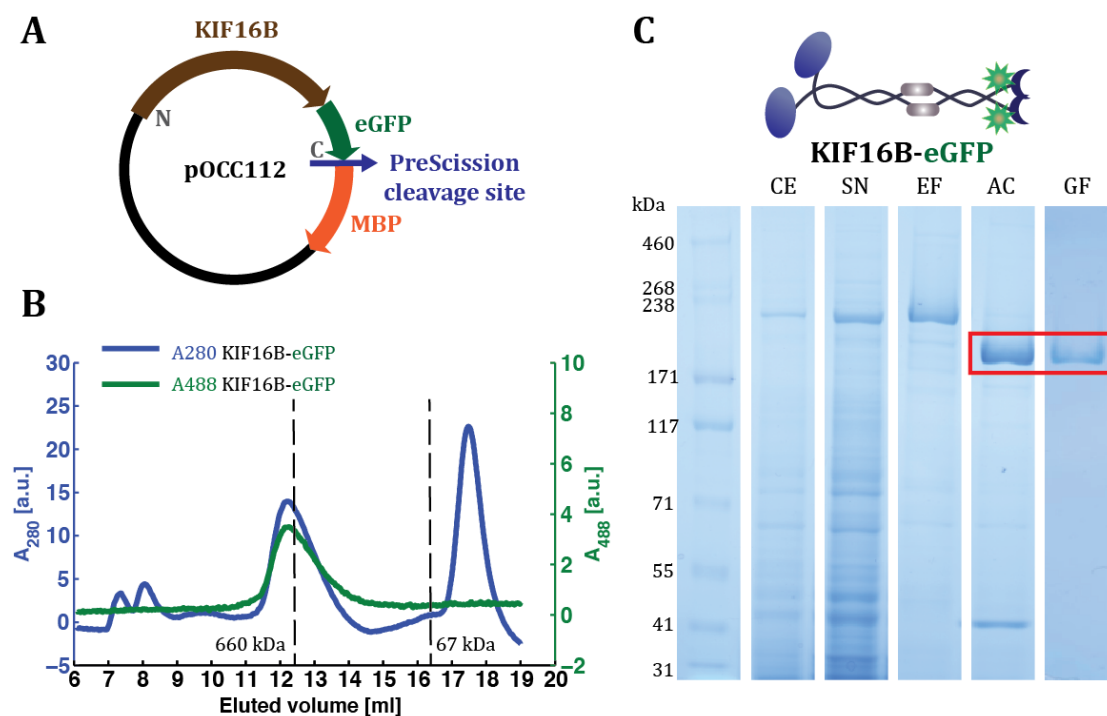


Figure 3.3 | Recombinant FL KIF16B was purified as a dimer by fusing it with a cleavable MBP tag. A) Schematic of the expression vector for MBP tagged FL KIF16B in pOCC112 B) Elution profile from gel-filtration chromatography for FL KIF16B showing absorbance at 280 nm A_{280} (blue) and 488 nm A_{488} (green). Dashed black line represents the peak for molecular-weight markers *Thyroglobulin* (660 kDa) and *BSA* (67 kDa). C) Coomassie stained gel showing the whole cell extract (CE), supernatant (SN) after ultra-centrifugation of cell lysate, eluted fraction (EF) after affinity purification, fraction after cleaving (AC) off the MBP tag with PreScission protease, and fractions from gel filtration (GF), containing FL KIF16B protein. The expected molecular weight of FL KIF16B tagged with GFP and MBP is 223.1 kDa and after cleaving off the MBP tag is 179.7 kDa marked with the red box in last two lanes

3.2 Biophysical characterization of KIF16B

The purified recombinant KIF16B constructs were then applied to *in vitro* assays such as stepping motility and gliding motility assay to characterize their biophysical properties.

Stepping motility assays

In order to observe the interaction of individual KIF16B motor with microtubules, stepping motility experiments (see Stepping motility assays, Chapter 5, page 112) were performed with FL KIF16B as well as shorter KIF16B constructs tagged with GFP. TIRF microscopy was applied to resolve the

molecular interactions between the motor proteins and microtubules at a high spatial and temporal resolution. A substantial number of single motor motility events were analyzed with the kymograph evaluation tool of FIESTA. The mean stepping velocity, the run length and the dwell time of single motors on microtubules was determined from the kymographs (see Data analysis, Chapter 5, page 124). All experiments were performed at room temperature in H2OS150 buffer.

From SM fluorescence experiments with KIF16B constructs we found out that all the KIF16B constructs were active and interacted with microtubules. We observed processive motility on a microtubule for FL KIF16B under saturating ATP conditions (fig. 3.4A). The mean velocity and run length for FL KIF16B was determined to be $0.92 \pm 0.11 \mu\text{m/s}$ (mean \pm s.d) and $1.66 \pm 0.08 \mu\text{m}$ (mean \pm 95% c.i.).

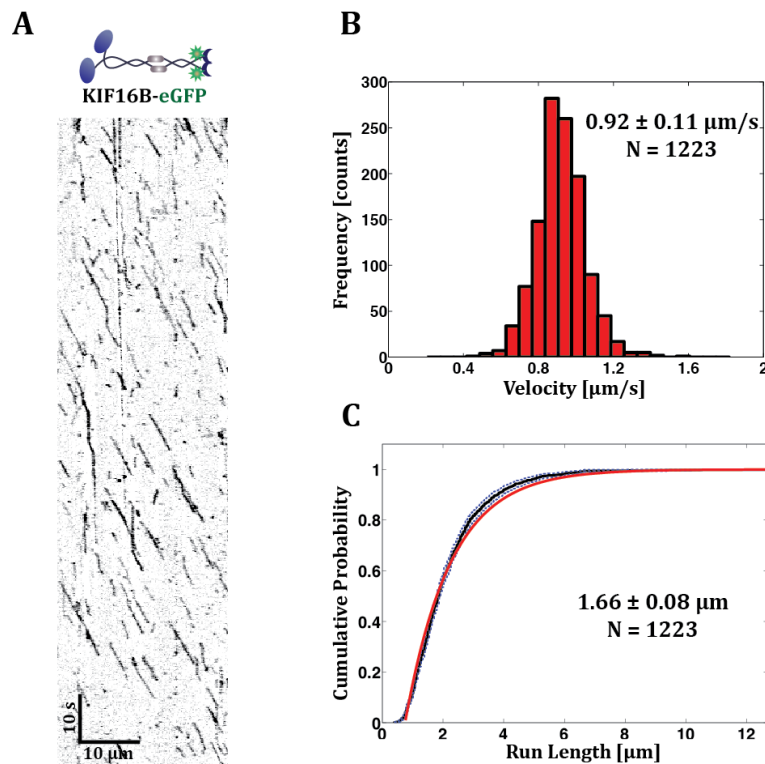


Figure 3.4 | FL KIF16B is active and moves on a microtubule with a moderate processivity. A) Representative kymograph showing individual KIF16B-eGFP motors moving along a microtubule. B) Histogram of SM velocities with ensemble average (mean \pm s.d), and C) Empirical cumulative distribution function (black solid line, dotted blue lines are the lower and upper bound of the ECDF) with a single exponential fit (red) of the run lengths (mean \pm 95% c.i.) obtained from the kymograph evaluation. Data are averages from more than 3 independent experiments. N is the number of molecules analyzed.

The truncated constructs of KIF16B with motor head domain, 16B-400 and 16B-400-PX also showed processive motility on a microtubule under saturating ATP conditions. The mean velocity and run length for 16B-400 was determined to be $0.947 \pm 0.148 \mu\text{m/s}$ (mean \pm 95% c.i.) and $0.79 \pm 0.08 \mu\text{m}$ (mean \pm 95% c.i.) (fig. 3.5A-C) and for 16B-400-PX as $0.493 \pm 0.091 \mu\text{m/s}$ (mean \pm 95% c.i.) and $1.41 \pm 0.16 \mu\text{m}$ (mean \pm 95% c.i.) (fig. 3.5D-F).

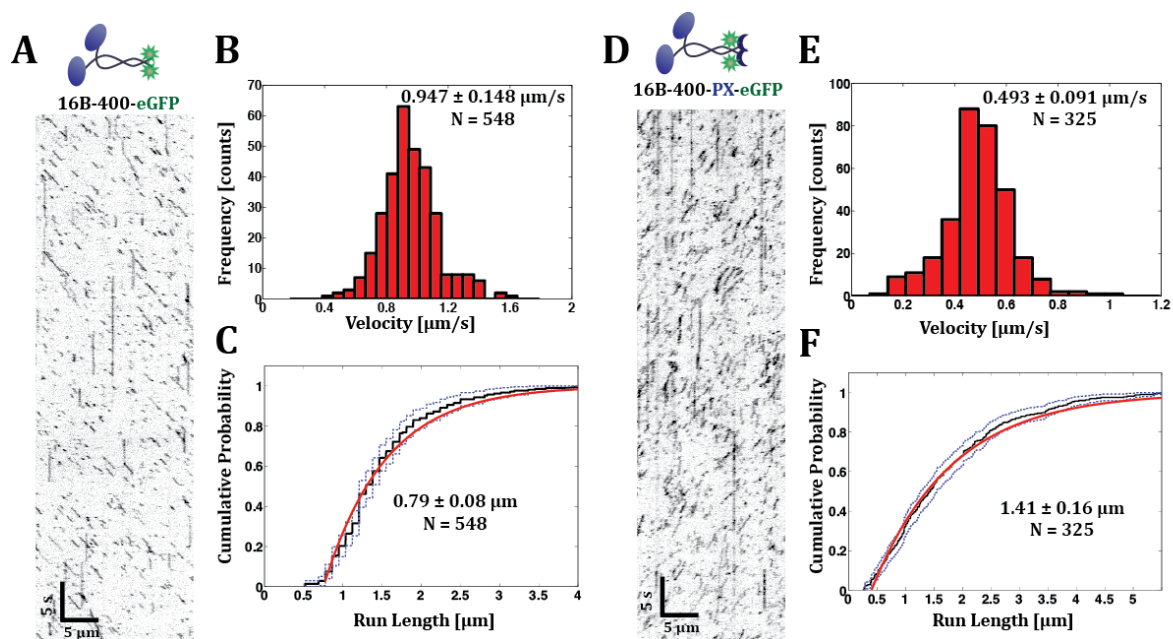


Figure 3.5 | 16B-400 and 16B-400-PX are both processive, but show different motility behavior. A, D) Representative kymograph showing shorter construct 16B-400 and chimeric construct 16B-400-PX moving along a microtubule. B, E) Histogram of SM velocities with ensemble average (mean \pm s.d), and C) ECDF (black solid line, dotted blue lines are the lower and upper bound of the ECDF) with a single exponential fit (red) of the run lengths (mean \pm 95% c.i.). Data are averages from more than 3 independent experiments. N is the number of molecules analyzed.

We found out that the mean stepping velocity for 16B-400 motor head and FL KIF16B motor were same, but the FL KIF16B had longer run length as compared to just the motor domain. These data suggests that the amino acid residues after the motor domain play a role in increasing the affinity of motor with microtubule, making it more processive but does not affect the ATPase rate of motor domain since the stepping velocity does not change.

The shorter chimeric construct with PX domain at the C-terminal moves at almost half the velocity observed for motor domain but the run length is twice as much as compared to only motor domain 16B-400. This suggests that the addition of a PX domain after 400 a.a alters the conformation of motor, which lower the ATPase rate of the motor domain when interacting with a microtubule but increases its dwell time on a microtubule.

KIF16B constructs with 1-429 a.a. i.e. 16B-429 and 16B-429-PX did not show processive motility on microtubules. 16B-429 interacted with microtubules for short duration while 16B-429-PX showed diffusive interaction with a microtubule under saturating ATP conditions (fig. 3.6).

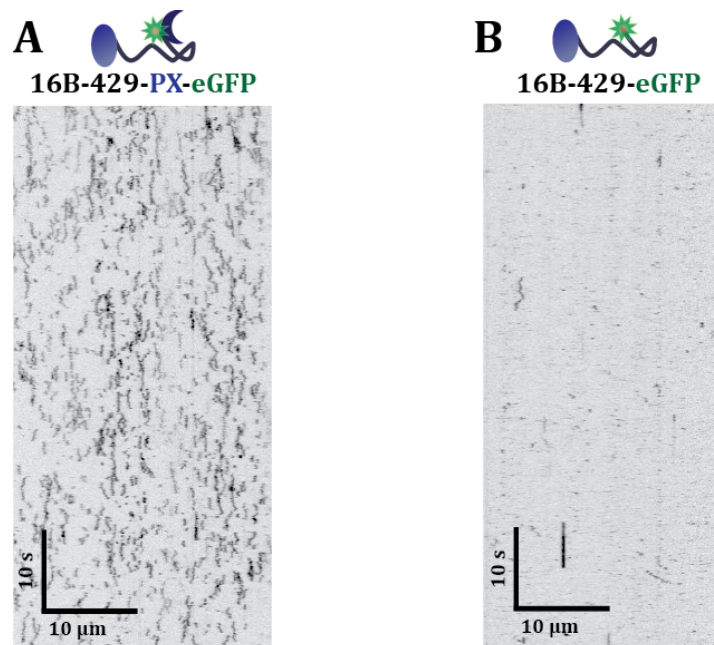


Figure 3.6 | 16B-429 and 16B-429-PX interact diffusively with microtubules. Representative kymograph showing interactions of short KIF16B constructs with a microtubule A) 16B-429 and B) chimeric construct 16B-429-PX.

16B-400 motor domain was processive while 16B-429 was not processive suggests that the amino acids from 400-429 inhibit the dimerization of shorter motor construct. This observation is consistent with the recently reported findings from (Soppina et al., 2014) where they show that the CC1 region (400-450 a.a.) of KIF16B motor interacts with NC region (380-400 a.a) such that the KIF16B motor construct with (1-400 a.a) is a dimer whereas (1-455 a.a) is a monomer. In addition, our results confirm that the NC region of the motor domain is sufficient to form a dimeric minimal construct of KIF16B motor.

The interaction of 16B-429 motor construct with a microtubule is of very short duration (see fig. 3.6A), which is expected for a monomeric motor head, because a single motor head would dissociate from a microtubule after one ATPase cycle. However, 16B-429-PX motor construct diffused on a microtubule, which indicates an additional microtubule interaction site independent from the motor head. Because the only difference between the two constructs was PX domain at the tail, we hypothesized that the PX domain might have affinity for microtubules. To test this hypothesis we performed sliding microtubule assays (Braun et al., 2011; Lansky et al., 2015), where a protein having two independent microtubule binding sites can crosslink two microtubules relative to each other to form microtubule bundles. We didn't observe any microtubule – microtubule interaction in sliding assays with 16B-429-PX. Furthermore, we did not observe any interaction of just PX domain with microtubules when affinity of PX-eGFP monomers with microtubules was investigated in independent experiments. Therefore, the mechanism of increased interaction of 16B-429-PX with a microtubule as compared to 16B-429 couldn't be determined. A possible reason could be an altered conformation due to introduction of PX domain that influences its interaction with a microtubule, which was also observed for shorter dimeric motor domain construct with PX domain at the tail (16B-400-PX).

In their study on kinesin-3 using cell extracts, Soppina et al. reported 16B-400 motor construct steps on a microtubule with an average velocity of 0.95 $\mu\text{m/s}$, which matches well with our findings. However, they showed that the 16B-400 is

highly processive with an average run length of $\sim 9.5 \mu\text{m}$ which is 12 times greater than the average run length, $0.79 \mu\text{m}$, observed in our experiments with purified 16B-400 construct. Furthermore, in our experiments with purified FL KIF16B, we obtained an average run length of $1.66 \mu\text{m}$ that is higher than the run length of conventional kinesin-1 ($\sim 1 \mu\text{m}$), but still does not classify as highly processive. The reason for such high processivity of 16B-400 in cell-extract studies as compared to purified proteins is perplexing.

To investigate if the nucleotide state of microtubule and its conformation affected the interaction of motor with microtubules we performed the stepping assays with three differently prepared microtubules a) GDP microtubules stabilized with taxol (Tx-MT), b) GMPCPP microtubules and c) Double-stabilized microtubules (DS-MT), which are GMPCPP-MT stabilized with taxol. We didn't observe significant difference in the velocity as well as the run length of KIF16B moving on differently prepared microtubules (Table 3.1). Therefore, we can exclude the factor that microtubule architecture might result into superprocessivity of KIF16B motor.

Table 3.1 | Velocity and run length of FL KIF16B for different microtubule preparations.

Microtubule	Velocity ($\mu\text{m/s}$) mean \pm s.d.	Run length (μm) mean \pm 95% c.i.	Number of molecules
Tx-MT	0.915 ± 0.108	1.59 ± 0.12	670
GMPCPP-MT	0.928 ± 0.109	1.69 ± 0.14	553
DS-MT	0.925 ± 0.169	1.49 ± 0.26	185

To determine the oligomeric state of FL KIF16B motors in our SM experiments, we performed bleaching experiments of GFP labeled FL KIF16B. The bleaching experiments were performed by incubating motors with microtubule, in a stepping assay geometry, in presence of 0.1 mM AMP-PNP, a non-hydrolysable analogue of ATP, which arrest the motors on microtubule in a strongly bound state. From a total of 310 randomly picked molecules in bleaching experiments, 42 % exhibited two-step bleaching (fig. 3.7) and 37 % of the events, the

molecules exhibited one-step bleaching. One step bleaching events could have occurred due to various reasons such as only one of the GFP molecules got bleached during the duration of imaging, in-activation of one of the GFPs and non-functional GFPs. Moreover, part of these events might have originated from the rapid bleaching of two GFPs after each other that couldn't be resolved. Only 5 % of the events showed bleaching with more than two-step and in rest of the molecules the bleaching steps couldn't be detected.

The bleaching experiments confirmed that the FL KIF16B molecule were in dimeric state under our experimental conditions. Our results show that a FL KIF16B motor protein is dimeric without attaching to a cargo and exhibit processive motility on a microtubule.

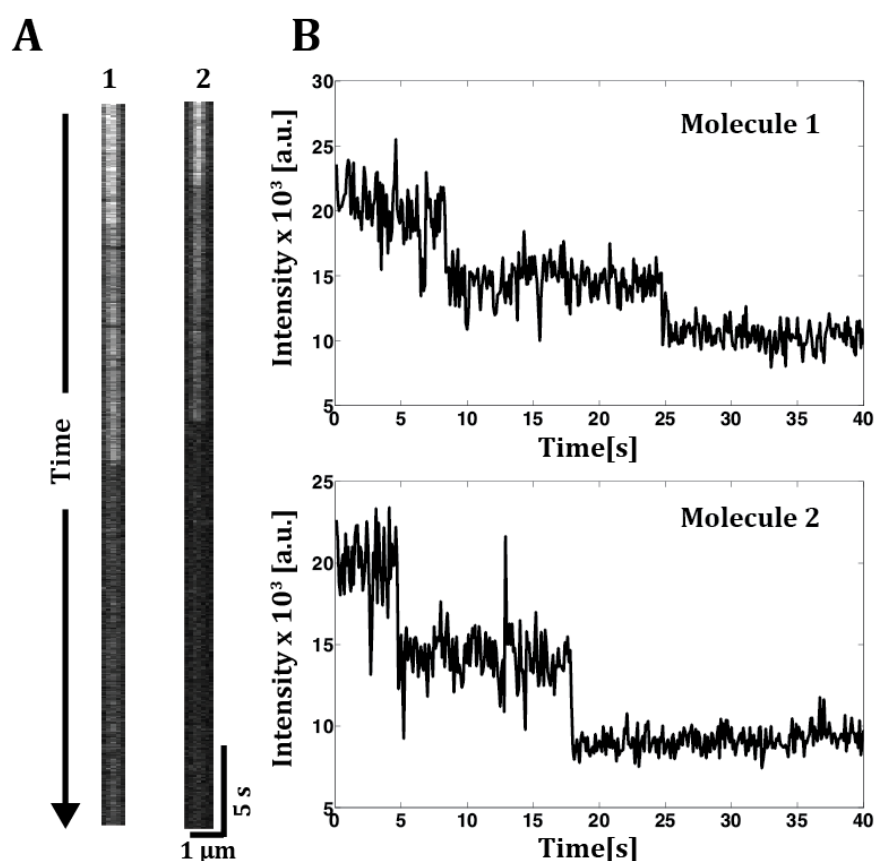


Figure 3.7 | FL KIF16B forms a dimer without attaching to a cargo.

A) Representative kymographs of two individual KIF16B molecules bound rigidly to a microtubule in presence of AMP-PNP bleaching over time B) Intensity profile of single KIF16B molecules (shown in kymographs) over time exhibiting two-step photo bleaching.

Gliding motility assays on surface immobilized KIF16B

To investigate the multi-motor transport characteristics of KIF16B motors, conventional gliding motility assays were performed. The motors were immobilized on a glass substrate via GFP antibodies and the translocation of fluorescently labeled microtubules, on the substrate coated with motors, was monitored. The microtubules were then tracked and the mean gliding velocity was obtained by fitting the distribution of frame-to-frame velocities of microtubule center (see Data analysis, chapter 5, page 121). All gliding assays were done under saturating ATP concentrations in H20S150 buffer at room temperature.

The average microtubule gliding velocities for 16B-400 and FL KIF16B were calculated to be $0.489 \pm 0.167 \mu\text{m/s}$ and $0.634 \pm 0.133 \mu\text{m/s}$ (mean \pm s.d.), respectively. Microtubule gliding velocity is lower than the stepping velocities of individual motors on microtubule for both the constructs. This can be attributed to the fact that in a stepping geometry a single motor only experiences hydrodynamic drag force, which is very low and under these no load conditions motors walk at their maximal velocity. However, in a gliding geometry where multiple processive motors are rigidly attached to the surface hinder each other due to negative interference, as the motors step asynchronously on microtubule (Bieling et al., 2008). The effect is more pronounced for the shorter construct 16B-400 as it is less flexible as compared to the FL KIF16B, which has coiled-coil regions interspersed with unstructured regions. Furthermore, the interaction with antibodies might cause clustering of motors or inactivation of a few motors causing them to bind rigidly to a microtubule, which would enhance the negative interference between multiple motors. The long trailing tail of the velocity distributions (fig. 3.8B) for the FL KIF16B suggests a hindered microtubule gliding motility. We observed the same effect for kinesin-1 constructs rKin430-SBP where the microtubule gliding velocity on motors rigidly bound to the surface is slower than the stepping velocity of individual motors moving on a microtubule. In conclusion, multiple KIF16B motors rigidly attached to a glass substrate showed hindered motility of microtubules, where the microtubule gliding velocities were lower than the single motor stepping velocities.

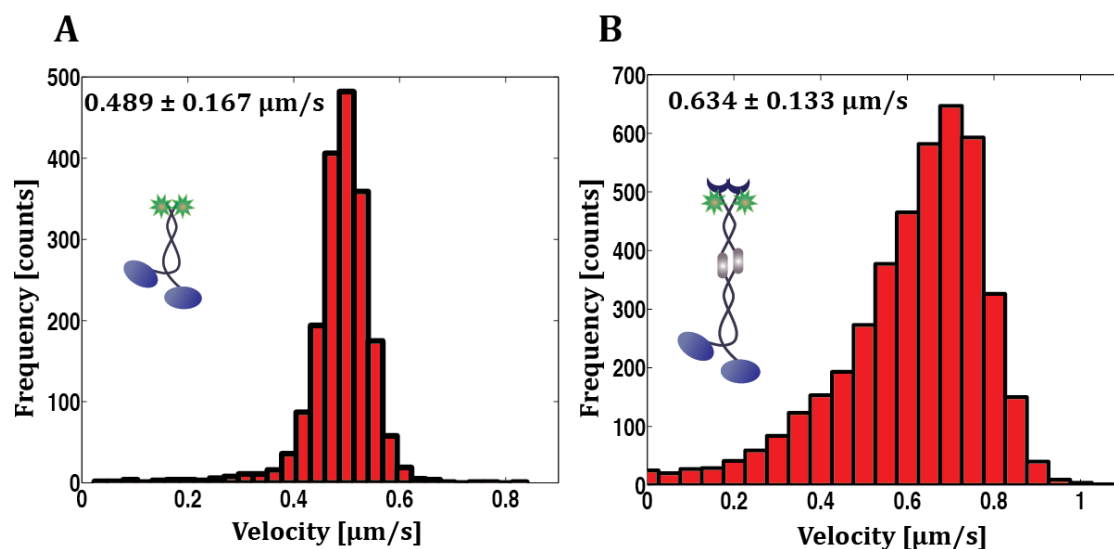


Figure 3.8 | Surface-immobilized FL KIF16B and 16B-400 propel microtubules at velocity lower than the SM stepping velocities. Histograms of the instantaneous velocity of gliding microtubules on A) 16B-400 B) FL KIF16B. The distributions were fitted to the ‘t-location scale’ to yield the indicated velocities (mean \pm s.d.). Data are averages from at least 2 independent experiments. The number of microtubules analyzed for both constructs is more than 70.

3.3 Gliding motility of microtubules by KIF16B linked to SLBs

To investigate the transport characteristics of multiple KIF16B motors in conjunction with membranous cargo, we attached the KIF16B motors, with its inherent lipid-binding domain, to planar PI(3)P SLBs.

Formation and characterization of PI(3)P SLBs

The first step to that effect was to prepare SLBs consisting of PI(3)P. We used the lipids DOPC:DOPE:PI(3)P:DOPE-Atto647n in the molar ratio of 77:20:3:0.01, which was also used in previously reported studies to investigate the binding kinetics of PX domain and PI(3)P (Blatner et al., 2007). We followed the same approach as described for the formation of 1 % biotinylated SLBs (see SLB formation, chapter 5, page 114), however, the PI(3)P containing SUVs adsorbed on the plasma-cleaned glass surface did not fuse to form SLB in H2OS150 buffer. This could be due to PI(3)P, which is a highly polar phospholipid with a negatively charged head group. It has been reported that PI(3)P forms microdomains in the pH range 7 - 9.5 and is not uniformly distributed in the vesicles. But at slightly acidic pH \sim 4 these domains are disintegrated (Redfern et al.,

2004). The negative charge of PIPs leads to electrostatic repulsion between the vesicles and the negatively charged glass substrate, which hampers the process of adsorption, rupture and spreading of vesicles. However, at pH below the pKa values of the phosphate group of PIPs net negative charge of PI(3)P head group is reduced and homogenous PIP SLBs can be formed. Therefore, the buffer conditions during the adsorption and spreading of PI(3)P vesicles on substrate are critical for the formation of SLBs. We searched in the literature for different buffers that are used for the formation of PIP containing SLBs and found out that in one of the recent study by (Braunger et al., 2013) it was shown that 20 mM citrate buffer at pH 4.8 works best for the formation of SLBs containing PIP₂ on glass substrate. Furthermore, it was reported that the acidic buffer required only for the formation of SLBs, and once the SLBs are formed it could be exchanged with physiological buffer to investigate the protein-membrane interaction. Therefore, 3% PI(3)P SLBs were formed on glass surface in C20S150 buffer (20 mM citrate, 150 mM NaCl, pH4.8). In C20S150 buffer we obtained diffusive SLBs on hydrophilic glass surface (see PI(3)P SLB formation, chapter 5, page 116) but there were still a lot of unfused vesicles on SLB surface that couldn't be removed even after rigorous washing with this buffer (fig. 3.8A).

To remove the SUVs that did not fuse and were tightly bound to the 3% PI(3)P SLBs we performed an additional step of treatment with Pluronic F127. It is a non-ionic triblock copolymer consisting of polypropylene oxide (PPO) hydrophobic core and polyethylene glycol (PEG) hydrophilic chains. Because of its amphiphilic nature the copolymer is used as surfactant in industries to dissolve fatty residues. A lot of studies have been done in the last decade to understand the interaction of pluronic F127 with liposomes as drug delivery agent. (Chandaroy et al., 2002; Liang et al., 2005; Feitosa et al., 2010). Liang et al., in their study found that the hydrophilic chains of F127 form a shell like structure around the vesicles composed of eggPC and made these vesicles more rigid. These surrounding F127 molecules screens the hydrophilic head groups of lipids and block the adhesion of lamellar lipid vesicles to other lipids. We utilized this property of pluronic F127 to remove the unfused vesicles from of 3% PI(3)P SLBs. We incubated the 3% PI(3)P SLBs with 0.5 % F127 solution in C20S150

buffer for 60 minutes, after formation of SLBs. Thereafter, the sample was washed rigorously to remove unfused vesicles and F127 from the system and the buffer in the reaction chamber was exchanged to H₂O/S150, by repeated washing, before addition of KIF16B. F127 treated PI(3)P SLBs looked more homogenous under the microscope (fig. 3.9C).

To quantitatively determine the quality of 3% PI(3)P SLBs, doped 0.05 % DOPE-Atto647n as a fluorescent lipid marker, we performed FRAP experiments to obtain the diffusivity and mobile fraction of lipids in SLBs (see FRAP analysis chapter 5, page 118). The diffusion coefficient calculated for 3 % PI(3)P SLBs with and without F127 incubation steps were similar with the values $2.62 \pm 0.21 \mu\text{m}^2/\text{s}$ and $2.74 \pm 0.33 \mu\text{m}^2/\text{s}$ (mean \pm s.d.) respectively. These values of diffusion coefficient are comparable to what were obtained for 1% biotinylated SLBs, with DOPC as major constituent and also the values reported in literature for DOPC SLBs on glass substrate (Braunger et al., 2013). However, we did not observe complete fluorescence recovery in the bleached spot for 3 % PI(3)P SLBs, the boundaries of bleached region were visible even after considerable time (fig. 3.9A,C). The mobile fraction determined from the fit was $\sim 75\%$ for both F127 treated and untreated 3% PI(3)P SLBs. The reason for this could be that the lower leaflet of lipid bilayer, interacting with the substrate, is immobile and partial recovery is achieved only from the upper leaflet. In conclusion, addition of even small amount of PI(3)P affects the formation of lipid bilayer on a glass substrate causing a reduction in the mobile fraction of lipids. To ensure that the PI(3)P is uniformly incorporated in the 3% PI(3)P SLBs. We tested the interaction of SLBs with a protein which specifically binds to the PI(3)P. FYVE domain of early endosome antigen 1 (EEA1) is one such protein domain which has very high specificity to PI(3)P with nano-molar affinities (Stenmark, 2009). We incubated the 3 % PI(3)P SLBs with GFP labeled FYVE domain of the protein EEA1 (1256-1401 a.a.), a gift from Enrico, Zerial lab, MPI-CBG. We observed a uniform distribution of FYVE domain throughout the SLB indicating that the PI(3)P was uniformly distributed over the SLB (fig. 3.9 E). The motility of lipids in the mobile fraction was not inhibited as indicated by the diffusion coefficient obtained and PI(3)P was homogeneously distributed in SLBs, therefore we used

the 3% PI(3)P SLBs, thus formed, for membrane-anchored gliding assays with KIF16B.

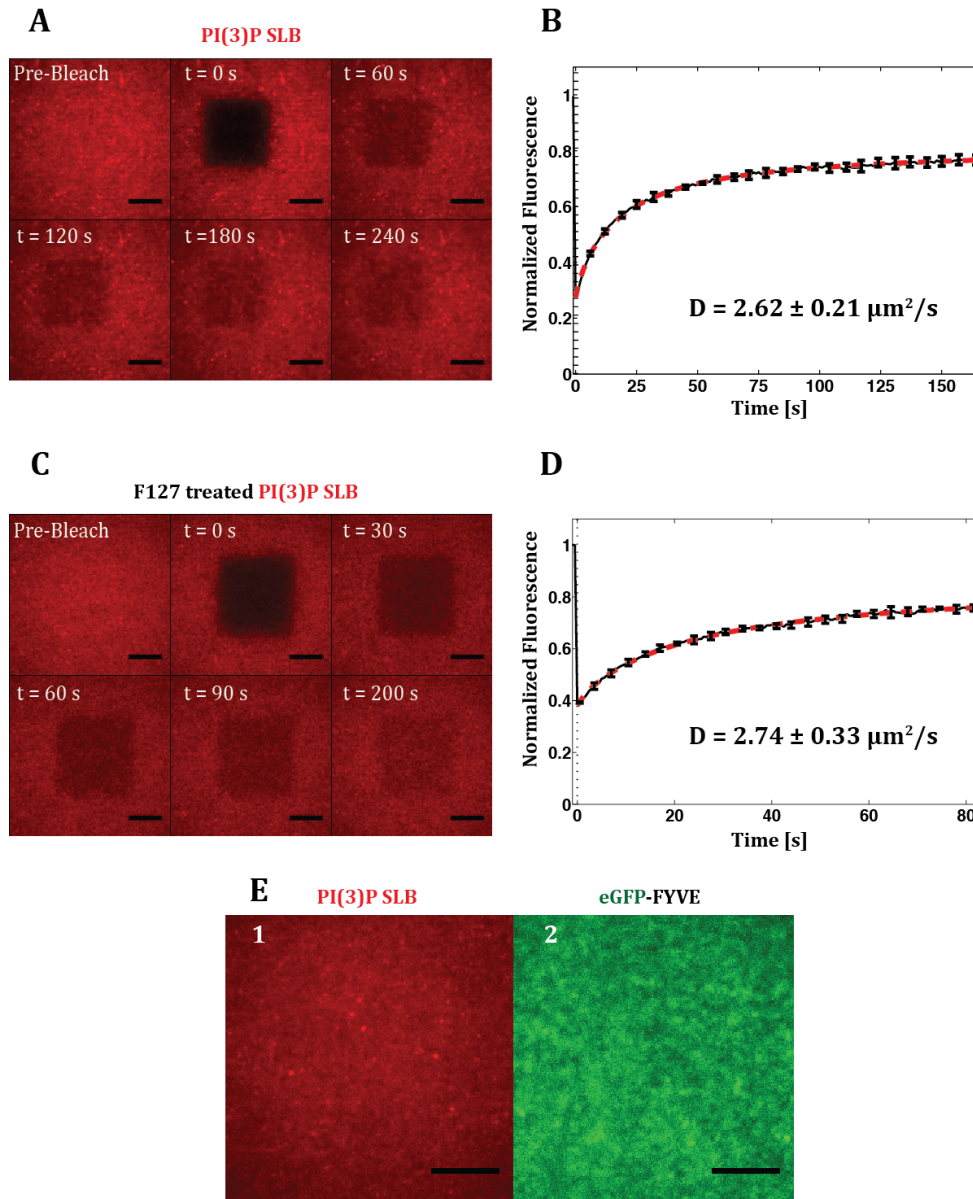


Figure 3.9 | 3% PI(3)P SLBs formed on glass were diffusive with uniformly distribution of PI(3)P. Time lapse fluorescence images of FRAP for A) 3% PI(3)P and C) F127 treated 3% PI(3)P are shown. Representative normalized intensity plots vs time for a set of photobleached regions are displayed adjacent to the time-lapse images. Mean FRAP recovery curves (black line \pm s.d.) are shown along with the best fit (dashed red line) for both the cases (B,D). 4 different regions on a SLBs were bleached to get the mean FRAP recovery curve. Mean diffusion coefficient (mean \pm s.d.) is obtained from 3 independent SLB preparations. E1) Fluorescence image of Atto647-N doped 3% PI(3)P SLB in red along with E2) the distribution of GFP labeled FYVE domain in green (E2) on the SLB. Scale bars: 10 μm .

Anchoring KIF16B motors to PI(3)P SLBs

The next step was to investigate the interaction of FL KIF16B with the PI(3)P SLBs thus formed. GFP labeled FL KIF16B was incubated with the SLBs. Interaction of KIF16B-eGFP with the SLBs were recorded using TIRF microscopy and KIF16B-eGFP molecules diffusing on a SLB, were tracked using FIESTA software (fig. 3.10A). Mean diffusion coefficient D_{KIF16B} of single motors was calculated to be $1.35 \pm 0.08 \mu\text{m}^2/\text{s}$ (mean \pm 95% c.i., fig. 3.10B) from SPT analysis (see Data analysis, chapter 5, page 123)

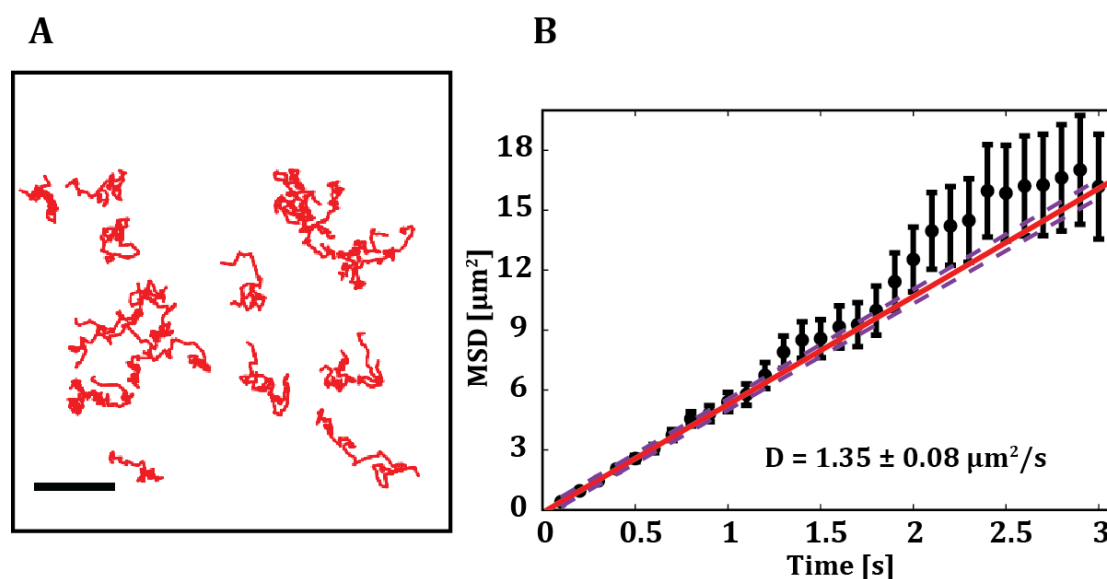


Figure 3.10 | FL KIF16B motors anchored to PI(3)P SLBs were diffusive.

A) Trajectories of freely diffusing GFP labeled FL KIF16B anchored to 3% PI(3)P SLBs. B) Cumulative mean squared displacement (MSD) data (black, mean \pm s.d.) of diffusing KIF16B molecules with a linear fit (red line), and 95 % confidence interval (dashed magenta line), to first six points to obtain the diffusion coefficient (mean with 95 % CI, n=21) of KIF16B motors on lipid bilayer is shown. Scale bar: 10 μm .

The diffusion coefficient of motors D_{KIF16B} from the SPT analysis is approximately half of the D_{Lipids} of SLB from the FRAP analysis. The slow diffusion of KIF16B as compared to SLB can be explained considering KIF16B motors bind to two PI(3)P lipid molecules. This would imply that instead of diffusing in SLB as a single lipid molecule PI(3)P bound to KIF16B would be diffusing in SLB as a pair resulting in twice the frictional force and hence half the diffusivity as compared to a single freely diffusing molecule of PI(3)P. The similar effects have also been reported for PH domain, which binds specifically to PIP₂ (Knight et al., 2010;

Ziemba et al., 2013). In this study it was shown that the diffusivity of oligomers of PH domain is inversely proportional to the number of PH domains in oligomers. The observation that the diffusivity of KIF16B is half of the SLB provides further evidence that the KIF16B motor is a dimer when interacting with PI(3)P SLB.

Membrane-anchored gliding motility assays with KIF16B

To investigate if KIF16B motors also display the similar cooperative behavior at increasing surface motor density as observed for membrane-anchored kinesin-1 motors, the motor density on PI(3)P SLBs was varied by changing the bulk concentration of KIF16B motors in the chambers. KIF16B motors, at different concentrations, was applied to the PI(3)P SLBs for 10 minutes, followed by a washing step to remove the unbound motors. Rhodamine labeled microtubules were then added to the chamber, and their translocation was monitored with fluorescence microscopy (fig. 3.11A). The gliding velocity was determined by MSD analysis of microtubule center, as described in the previous chapter (see Data analysis, chapter 5, page 121). As expected, the number of microtubules landing on the SLBs increased with increasing KIF16B motor density on SLBs. Microtubules did not attach to PI(3)P SLBs in absence of motors, confirming that the landing of microtubules on SLBs were only due to the interaction between KIF16B and microtubules (fig. 3.11B). We found out that the gliding velocities of microtubules increased with increasing KIF16B concentration reaching single motor stepping velocity of about 0.9 $\mu\text{m/s}$ (fig. 3.11C). Furthermore, membrane-anchored KIF16B could propel microtubules at velocities higher than the microtubule gliding velocities obtained for surface immobilized KIF16B motors. These results further strengthen our previous findings that anchoring of motor to a diffusive lipid-bilayer provides flexibility to the transport system such that the multiple-motors transporting a cargo do not hinder each other.

We observed similar qualitative trend of gliding velocities on F127 treated PI(3)P SLBs i.e. increasing velocities with increasing motor concentration. However, the microtubule gliding velocity was much lower as compared to untreated SLBs at same bulk motor concentration. This could be explained by lower motor densities on F127 treated SLBs as compared to untreated SLBs,

even at the same bulk concentration of motors. The average integrated GFP intensities on the F127 treated SLBs were less than the untreated SLBs, for same bulk motor concentration. However, further experiments are required to measure the actual surface density at different bulk concentration for F127 treated as well as untreated PI(3)P SLBs using spiking assays. Although, the SLBs were rigorously washed after F127 treatment to remove all the F127 molecules from the solution but F127 incorporated in the PI(3)P SLBs could not be removed. This might impede the attachment of KIF16B motors to PI(3)P resulting in a lower motor density as compared to untreated SLBs even for same bulk concentration. Thus, even though the treatment with F127 helps in the formation of homogenous PI(3)P SLBs, it interferes with the interaction of motors with PI(3)P.

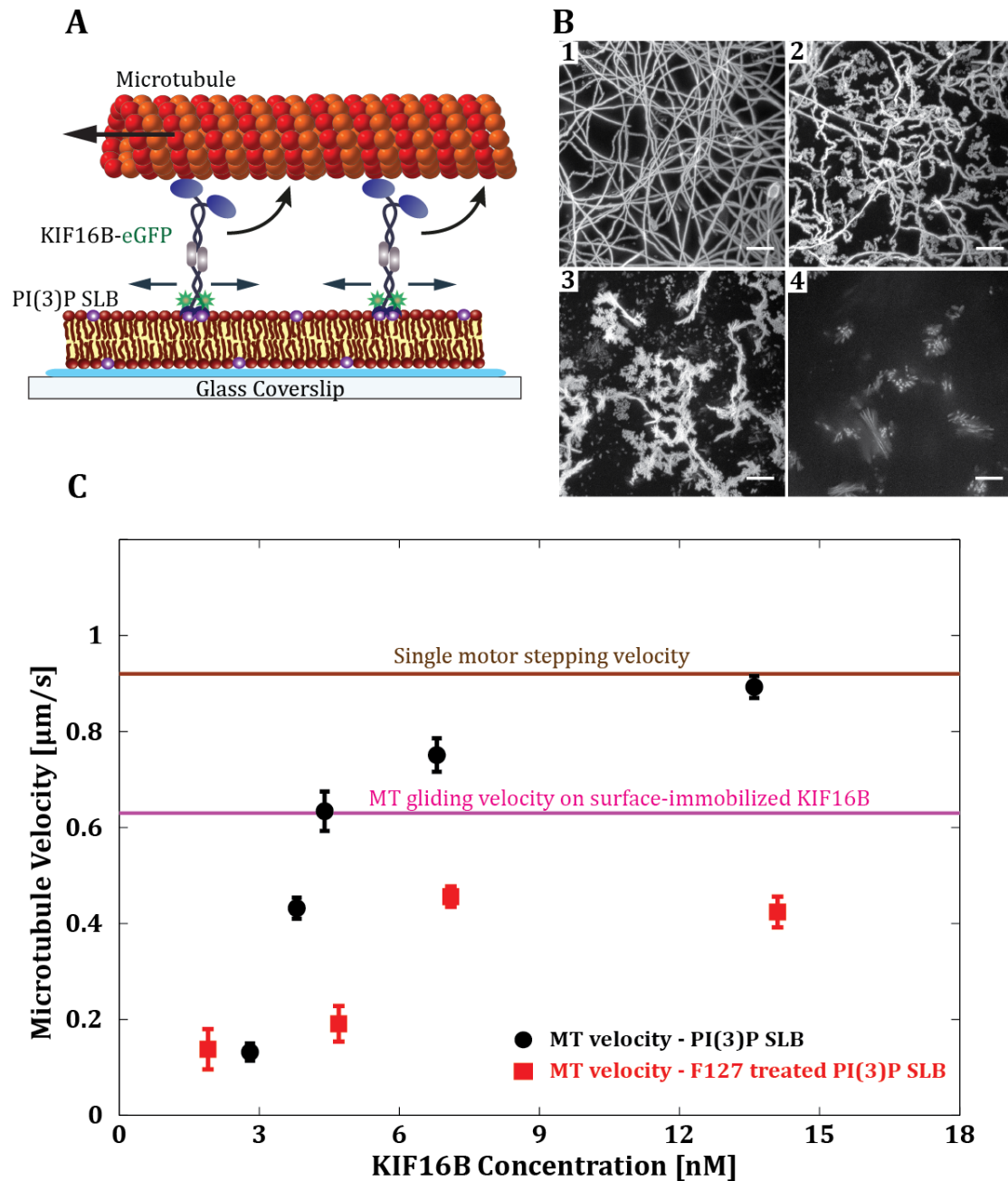


Figure 3.11 | Microtubule gliding velocity, for membrane-anchored KIF16B, increased with increasing motor densities attaining velocities higher than for the surface-immobilized motors.

A) Schematic drawing of the experimental setup, FL KIF16B motors, attached to 3% PI(3)P SLBs via its PX domain, propel microtubules. B (1-4) Maximum projections of 150 frames, 1 s/frame time lapse movies for microtubules gliding on KIF16B motors, attached to a SLB, at different motor concentration (1) 13.6 nM (2) 4.8 nM (3) 2.8 nM (4) no motors. Scale bar: 10 μm . C) Microtubule gliding velocity as a function of bulk concentration of KIF16B motors attached to untreated SLBs (black, mean with 95% C.I.) and with F127 incubation (red, mean with 95% C.I.). Solid lines represent the mean velocity of single motors moving on a microtubule (brown) and mean velocity of microtubules propelled by KIF16B motors immobilized on glass substrate (magenta).

To gain mechanistic insights into the working of a diffusive KIF16B motors we imaged GFP labeled membrane-anchored KIF16B motors while propelling microtubules. We observed that FL KIF16B motors, attached to a diffusive substrate, slips backwards while propelling a microtubule forward (fig. 3.12). Furthermore, the motors accumulated at the trailing end of a microtubule before detaching from a microtubule. However, these accumulated KIF16B motors did not disaggregate upon detachment from microtubules but rather stayed as clusters. Therefore, the number of clusters as well as their size increased with time owing to the fact that any passing microtubule in the vicinity of already formed cluster adds more motors to it.

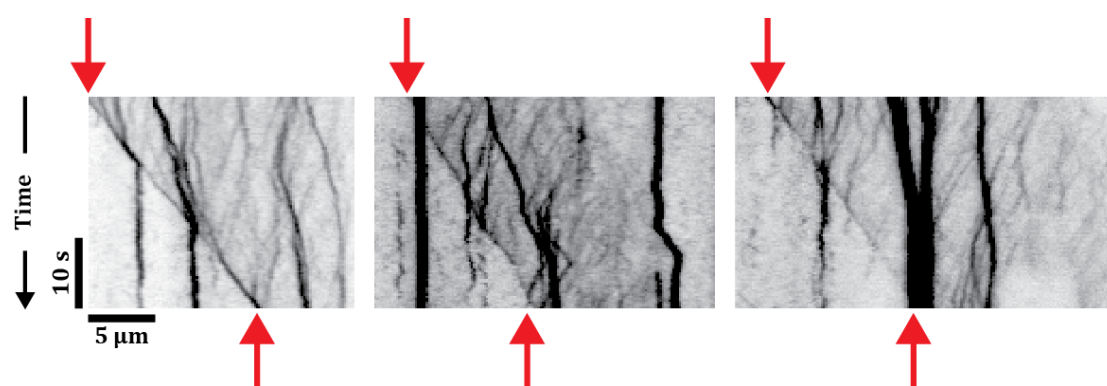


Figure 3.12 | Membrane-anchored KIF16B motors slip under gliding microtubules while propelling them forward. Representative kymographs of KIF16B motors (dark signals) while propelling a microtubule forward on a SLB. Time is progressing from top to bottom. Microtubules move from left to right, red arrows mark the trailing end of a microtubule. Broad dark vertical lines on kymographs are clusters of motors that are formed over time by fusion of small clusters; one such fusion event is visible in the rightmost kymograph.

In summary, we could show that KIF16B motors attached to lipid bilayer were functional and propelled microtubules. Membrane-anchored KIF16B motors, similar to membrane-anchored kinesin-1, displayed the cooperative effects where the microtubule gliding velocity increased with increasing motor density.

3.4 Transport of SUVs and lipid-coated beads attached to KIF16B

Planar SLBs provide us with a great system to study the transport properties of multiple-motors in a diffusive environment, where the motor density can be measured by directly observing diffusing motors. However, inside a cell motor proteins transport vesicular cargo and organelles having a range of geometries, shapes and sizes. To investigate the effect of cargo size and curvature on the transport characteristics of membrane-anchored KIF16B, we performed preliminary experiments with spherical cargo in form of PI(3)P SUVs and lipid-coated silica beads, (see chapter5, page 117 for details) to which FL KIF16b motors were directly attached. The following experiments were performed with the help of Tim Rehfeldt, a former HiWi student in our lab.

Transport of SUV by KIF16B

3 % PI(3)P SUVs were formed by ultra sonication of MLVs, and incubated with very low concentration of motors ~ 1 nM KIF16B-GFP. The attachment of motors to the 3% PI(3)P SUVs was observed by fluorescence microscopy. The fluorescent signal (red) of SUVs doped with Atto647n as lipid marker dye and GFP labeled KIF16B motors (green) always co-localized. SUVs bound to the motors when flushed into the channel, with surface-immobilized rhodamine microtubules. In this system we could image the microtubule, FL KIF16B-GFP motors and the SUVs, all labeled with different fluorescent markers with non-overlapping emission profiles, simultaneously. We found out that once the PI(3)P SUVs attached to the microtubule network on the surface, they were unidirectionally transported by KIF16B motors till the end of microtubule track (fig. 3.13A). We observed some infrequent pauses, for relatively big vesicular cargo, at the microtubule crossings, indicating that the attached diffusive motors can simultaneously interact with different microtubules. The transport distances were always much longer than the measured run length of individual single KIF16B motors. These finding can be explained by considering that multiple processive motors would be diffusing on the surface of cargo and at any instance at least one motor would engage with a microtubule, actively transporting the

cargo. Longer transport distance of cargo, attached to multiple processive motors such as kinesin-1, has been observed previously in different systems (Derr et al., 2012; Herold et al., 2012; Furuta et al., 2013). The mean velocity of the SUVs transported by KIF16B motors on a bed of immobilized microtubules, calculated from the slope of kymographs, was $0.725 \pm 0.067 \mu\text{m/s}$, (mean \pm s.d., $n = 14$), which is a bit lower than the single molecule stepping velocity ($0.95 \mu\text{m/s}$) of FL KIF16B. The lower velocities observed for the spherical cargo could be due to inter-motor interference as several membrane-anchored motors interacting with microtubules are in close proximity due to small size of the cargo and would compete for the limited number of binding sites on a microtubule track, thus inhibiting each other. Furthermore, in the diffusive environment of SUVs motors would move their membrane-anchor points in the cargo while stepping on the microtubule, thus the net movement of SUVs center of mass would be reduced, resulting in lower velocities. These preliminary experiments show that multiple KIF16B motors exhibit long-range transport of the SUVs. Moreover, PI(3)P SUVs can be used to mimic vesicular cargo to which KIF16B motor attaches directly. By varying the cargo size and the motor density in a systematic way, the effect of cargo geometry and size on the collective motor dynamics can be investigated.

Transport of lipid coated silica beads (LCBs) by KIF16B

To measure the maximum force output of KIF16B motors, which have thus far not been reported, we performed optical trapping experiments whereby $1 \mu\text{m}$ silica beads were coated with lipids having same lipid composition as of 3% PI(3)P SUVs. FL KIF16B motors attached directly to PI(3)P LCBs, which was trapped with optical tweezers (NanoTracker, JPK) to measure the forces generated by membrane-anchored KIF16B motors, while stepping on a surface-immobilized microtubule. We found out that the GFP labeled KIF16B motors co-localized with LCBs having 3% PI(3)P and did not attach to the beads coated with only DOPC. Therefore, KIF16B motors specifically attach to PI(3)P and do not interact with the beads in the absence of PI(3)P. We observed that the PI(3)P LCBs, attached to KIF16B, when positioned on top of a microtubule moved till the end of microtubule under no trap condition, indicating that there were several active motors involved in the transport (fig. 3.13B). From the

preliminary optical tweezers experiment we measured forces upto 25 pN (data not shown). This again confirms the presence of several motors, as the stall force of a single motor is not expected to be higher than 10 pN (Mallik et al., 2013). However, further experiments are required to first determine the stall force of a single KIF16B motor that can then be compared to the forces generated by multiple membrane-anchored motors. It would be interesting to investigate how does the forces scale up with motor density, when motors are bound to diffusive cargo. The *in vivo* stall force reported for kinesin-1 motors when attached to membranous cargo is ~2.6 pN (Shubeita et al., 2008) which is less than half of the reported *in vitro* values of 5-8 pN. It's speculated that the cofactors present inside the cell could modulate the force output, however the effect of diffusive cargo on the motor transport system has not yet been explored. Our preliminary experiments with PI(3)P LCBs showcase a promising experimental approach to study the force output of multiple membrane-anchored KIF16B motors, where the motor density can be tuned by the amount of PI(3)P.

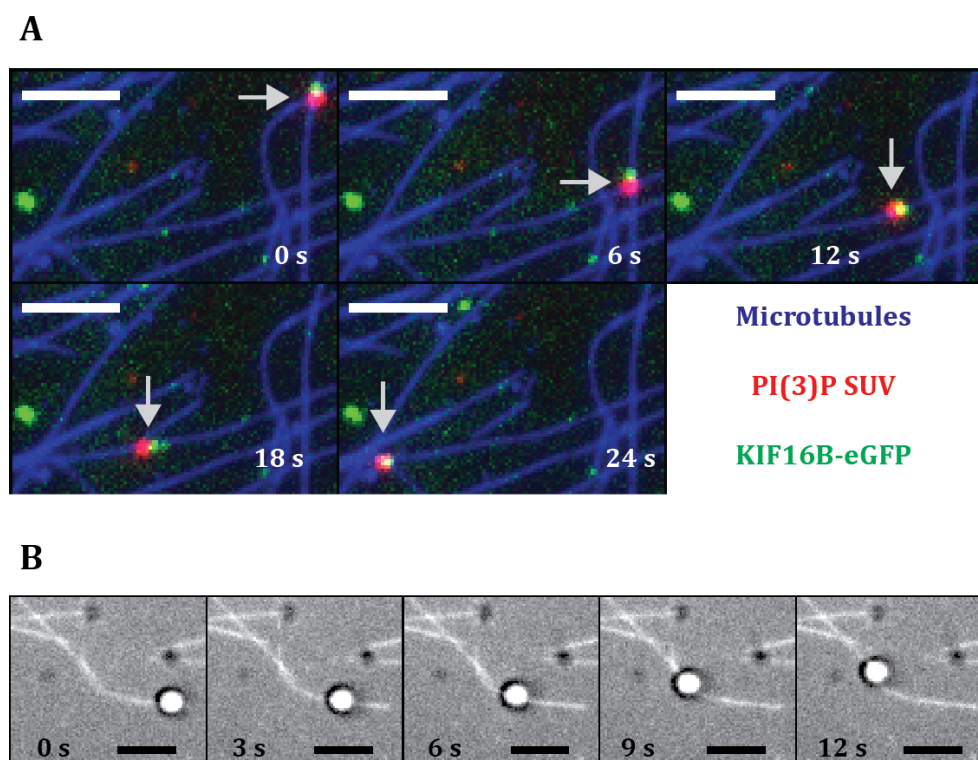


Figure 3.12 | KIF16B motors localized to the PI(3)P vesicular cargo *in vitro* and exhibited long-range transport. A) Triple-color time lapse images showing SUV (red, marked with Atto647n) being transported by KIF16B motors (green, labeled with eGFP) on a bed of immobilized microtubules (blue, labeled with rhodamine). White arrow points to the transported SUV and is shown to guide the eye. B) Time lapse images showing 1 μm sized lipid coated silica bead transported by KIF16B motors on a microtubule. Microtubules were labeled with Cy5 and LCB are marked with Atto647n. Scale bar: 5 μm .

3.5 Discussion

The results presented in this chapter provide insight into the functioning mechanism of KIF16B motor protein, which has been recently discovered. We used a ‘bottom up’ approach to study the biophysical characteristics of KIF16B whereby we reconstituted the transport motility *in vitro* using purified KIF16B. We determined the biophysical parameters such as velocity, run length and dwell time for different KIF16B motor constructs to study the role of different domains of KIF16B on its motility. Furthermore, we investigated how is the transport by multiple KIF16B coordinated when attached to cargo, by means of

membrane-anchored gliding motility assays as well as transport of spherical cargo such as SUVs and LCBs.

Functional FL human KIF16B was obtained by purifying it as a fusion partner with MBP tag. We obtained only one band in the SDS PAGE, in addition, western blot analysis confirmed that the KIF16B purification was free of any residue proteins. Purified FL KIF16B was active as elicited by single motor stepping motility assays and multiple motors gliding motility assays. We could show active and functional KIF16B FL motor moving on a microtubule track with a velocity of about 0.92 $\mu\text{m}/\text{s}$ and a run length of 1.66 μm . This is in contradiction with the claims from (Soppina et al., 2014) where they postulated that the dimerization of kinesin-3 family members is mediated by cargo binding and the dimeric motors are highly processive with run lengths greater than 10 μm .

Mechanism of FL KIF16B dimerization

The molecular mechanism for dimerization of members of kinesin-3 family is not well understood. KIF1A, the most extensively studied kinesin-3 family member, has been reported as a monomer in *in vitro* studies but as a dimer in an autoinhibited state in *in vivo* studies (Okada et al., 2003; Hammond et al., 2009). In the *in vitro* studies, it was shown that the KIF1A motors can dimerize at higher motor concentrations (Klopfenstein et al., 2002). Furthermore, it has been shown that the artificially induced dimerization of KIF1A motors makes it processive, which can walk on microtubules in hand-over-hand mechanism similar to kinesin-1 (Tomishige et al., 2002). The CC1-FHA domains of KIF1A have a strong propensity to form a dimer, which might play a crucial role in its dimerization (Huo et al., 2012). In a recent study Soppina et al. postulated that in many kinesin-3 family members motors, including KIF16B and KIF1A, the interaction between NC region and the CC1 region holds the motor into monomeric form, which is disrupted upon binding to the cargo and eventually leads to concentration driven dimerization. The cargo mediated dimerization hypothesis was based on the *in vivo* experiments where KIF16B motors with a mutation in PX domain, that interferes with the binding of PX domain to PI(3)P, was expressed. Mutated KIF16B motors, which could not bind to a cargo were

monomeric, which was confirmed by *in vivo* FRET studies. The NC and CC1 interactions were investigated by expression of shorter KIF16B constructs, KIF16B motors truncated after NC were processive and reached the axonal tip whereas KIF16B motor truncated after CC1 region were distributed throughout the cell cytosol (Soppina et al., 2014). In our *in vitro* studies with purified KIF16B constructs, we also found out that 16B-429 (1-429 a.a) having the NC and the CC1 region were not processive, indicative of monomers whereas 16B-400 (1-400 a.a.) were processive. This confirms the previous finding that the NC and CC1 interact in the truncated KIF16B constructs, and prevents dimerization. However, we cannot extrapolate the findings from truncated KIF16B constructs to FL KIF16B motors because the FL KIF16B has three additional coiled-coil regions following the CC1 (fig. 3.14A), which can lead to dimerization of FL KIF16B, in spite of NC-CC1 interaction. This is in contrast to KIF1A motor that lacks extra coiled-coil regions, thus the NC-CC1 interaction could be dominant resulting in its monomeric conformation (fig. 3.14B). In comparison, the FL KIF16B has much higher coiled-coiled propensity in its stalk, which is missing in the truncated KIF16B regions. CC2-CC4 in the downstream of CC1 can lead to opening of NC-CC1 interaction in KIF16B and formation of dimer, which was not tested in the study by Soppina et al.

In this thesis we provide three independent lines of experimental results (gel filtration, SM motility and photobleaching) to demonstrate that the recombinant FL KIF16B proteins are sufficient to form a dimer without the presence of cargo or auxiliary proteins. Our results complement the recent findings of the *in vivo* study of KIF16B motors by Farkhondeh et al., where it was shown that longer KIF16B constructs lacking PX domain, but having all the coiled-coil regions were localized at the tip of axon indicating that the longer constructs can dimerize and are processive even without binding to a cargo (Farkhondeh et al., 2015).

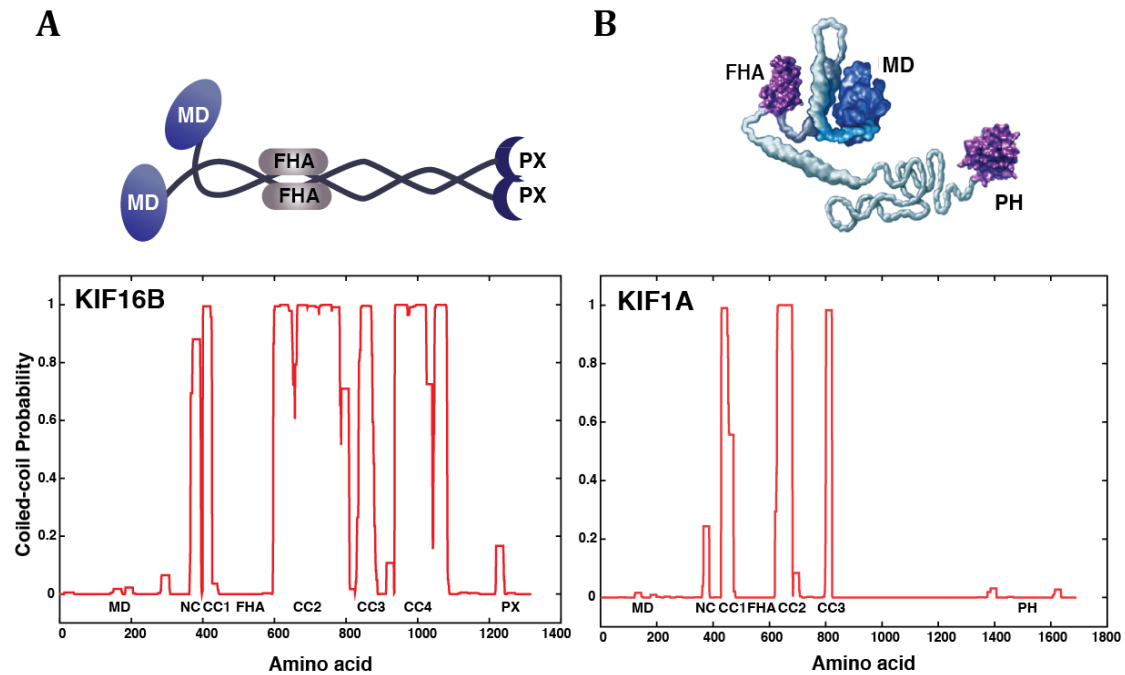


Figure 3.13 | Comparison of the conformational state of kinesin-3 motors, KIF16B and KIF1A. A) Schematic of KIF16B conformation, which exhibit properties of a dimer in our *in vitro* assays. B) Conformation of KIF1A, which exhibit properties of monomer, adapted from (Vale, 2003). The probability of coiled-coil formation of FL KIF16B and FL KIF1A determined using the COILS program (Lupas et al., 1991) (21 a.a window), is shown below the schematic conformations.

Previously reported findings that the mutation in PX domain of FL KIF16B motors that interferes with the binding of motor to a cargo, results into monomeric conformation is intriguing. Our findings, in this thesis, from the chimeras of KIF16B motors with PX domain reveal that the PX domain is critical for fully active conformation state. We observed longer interaction with microtubules for 16B-400-PX, and 16B-429-PX and slower motility of 16B-400-PX as compared to FL KIF16B and 16B-400. From SM studies we confirmed that the PX domain itself doesn't interact with microtubules. Therefore, we speculate that the PX domain can interact with internal domains of the FL KIF16B motor and alter the structure of motor. As a consequence, the mutation in PX domain might result into structural changes in the FL KIF16B conformation that impedes its dimerization.

Regulation of KIF16B activity and superprocessivity

The activity of motor proteins inside a cell is tightly regulated; they remain inactive when not bound to cargo to prevent squandering of ATP for example

kinesin-1 motors are auto-inhibited by their tail domain. The mechanism of underlying the KIF16B activation is not yet fully understood. Two recent *in vivo* studies have postulated different mechanism for KIF16B activation; Soppina et al., proposed that the activation of kinesin-3 motors, including KIF16B, is linked to the cargo binding, where the intramolecular interaction between NC-CC1 domains maintains the monomeric conformation of the motors. This interaction is released by binding to cargo, resulting into dimerization of motors and highly processive motility (Soppina et al., 2014). In contrast in another recent study, Farkondeh et al., have proposed a stalk inhibition mechanism, where they show that CC3-CC4 region (a.a. sequence 810-1074) of KIF16B motor binds to the motor domain of KIF16B to inhibit motor activity, in an ATP dependent manner. This interaction is released by some additional factor inside the cell, which is not known (Farkondeh et al., 2015).

In this thesis, we show that purified FL KIF16B motors are dimeric and active without the presence of cargo or additional factors. Our data for FL KIF16B motor velocity ($\sim 0.95 \mu\text{m/s}$) moving on a microtubule matches well with the reported velocities for KIF16B motor head by Soppinna et al. However, high processivity for FL KIF16B motor as well as auto-inhibition was not observed for purified constructs. A reasonable explanation could be that both the above-mentioned mechanisms are derived from either *in vivo* studies or with the whole cell lysate, so there could be many additional factors other than just motors contributing towards the observed behavior of KIF16B. However, in our *in vitro* system with the purified FL KIF16B such behavior is not observed due to absence of these additional factors. Moreover, *in vitro* stepping motility assay with purified KIF16B motors can be used as a quick screen method to look for potential molecules that might be regulating the transport behavior of KIF16B. Rab14, a small molecular G protein that found on the endosomes carrying FGFR2 receptor (Ueno et al., 2011) is a potential candidate which could be responsible for altering the transport behavior of KIF16B motors. It has been demonstrated by yeast two hybrid studies that KIF16B binds directly to Rab14-GTP, through its PX domain. Thus, Rab14 is an attractive candidate to investigate the effect on KIF16B mediated transport.

Cooperativity in transport driven by membrane-anchored KIF16B motors

Microtubule gliding velocity increased with motor density, for gliding motility assays on KIF16B motors attached to PI(3)P SLBs. Furthermore, we showed that the KIF16B motors attached to a SLB slip backwards while propelling microtubule forward. These observations are consistent with our finding from gliding motility on kinesin-1 attached to SLBs as well as our theoretical model. This confirms that in spite of different mechanism to attach to a cargo, the motors move their anchor point in the membrane while pushing a microtubule forward, thus high density of motors is required to propel a microtubule efficiently. Microtubule gliding velocity as high as the single motor stepping velocity were reached for motility on KIF16B motors attached to SLBs but not for surface immobilized motors. Our experimental results provide evidence that the anchoring of motors in diffusive lipid bilayer provides flexibility to transport system and induces cooperative effects, where higher motor densities are required for the efficient transport by multiple-motors.

4 Conclusion and outlook

In this thesis, we established ‘membrane-anchored’ gliding motility assays, which involved anchoring of molecular motors to a diffusive SLB and monitoring the translocation of microtubules propelled by diffusive motors. We demonstrate that the processive kinesin motors anchored to diffusive lipid bilayer show cooperative transport behavior such that the microtubule gliding velocity increases, to a maximum of single-motor stepping velocity, with increasing motor density. The flatness of SLBs enabled us to obtain the motor density directly by single-molecule fluorescence microscopy, which has thus far been calculated indirectly in multi-motor assays for example motors attaches to spherical beads or liposomes. In addition, we found that the fluidity of the lipid bilayer play a significant role in determining the gliding velocity of microtubules. Motors anchored to gel-like lipid bilayers propelled microtubules at higher velocities as compared to motors anchored to fluid lipid bilayer. Furthermore, we show that coupling of motors to a lipid-bilayer provide flexibility to the transport system to prevent negative interference between multiple processive motors when collectively transporting a cargo. The negative interference has been observed when motors rigidly attached to surface or DNA scaffold (Bieling et al., 2008; A. R. Rogers et al., 2009).

In vitro studies on multiple kinesin-1 transport show that the cargo velocities are insensitive to motor density (Howard et al., 1989; Derr et al., 2012; Furuta et al., 2013). In these systems the rigid cargo doesn’t allow slippage of motors, in contrast the membranous vesicles or organelles are fluid and hence the motors while stepping on microtubule would slip back in the cargo, depending on the fluidity of cargo lipid-bilayer. This would result in a reduced transport velocity, and thus more motors would be required to move the cargo at high speeds. *In vivo* cargo transport velocities determined by tracking vesicles or organelles, in various cells, have quite large spread and the velocity histograms contain multiple regularly spaced peaks (Hill et al., 2004; Zahn et al., 2004; Kural et al., 2005; Levi et al., 2006; Shtridelman et al., 2008). In the complex environment of

cell there could be many factors that influence the cargo transport, such as various cargo binding partners or the movement of cytoskeletal filaments itself, to produce faster or slower speeds (Kulic et al., 2008). However, one of the possible explanations for the difference observed in transport behavior for *in vitro* and *in vivo* experiments could be regulation of motor density in cargo by addition or removal of active motors, which would allow them to be transported faster or slower. Inside a cell this could be achieved by tuning the motor binding receptors on cargo or by modulating the lipid-composition, where the signaling lipids such as PIPs which when mixed with other lipids in cellular membrane cluster (Redfern et al., 2004; Stahelin et al., 2014; Wang et al., 2014), to increase the motor density and decrease their diffusivity. In our membrane-anchored gliding assays with FL KIF16B motor bound to PI(3)P containing SLBs, we observed clustering of motors while transporting microtubule, indicating that either PI(3)P can cluster in presence of KIF16B or the attachment to a microtubule increases the local concentration of motors which leads to clustering. Further experiments using labeled PI(3)P can help to characterize and quantify the localization of KIF16B and PI(3)P lipids, which could reveal the clustering behavior of KIF16B. The influence of motor density and lipid-bilayer properties has also been shown in *in vitro* studies performed to reconstitute tubular transport intermediates between organelles, by extraction of nano-vesicular tube from GUVs with kinesin-1 motors (Leduc et al., 2004), where it was shown that the motors cluster at the tip of tube and minimum motor density is required for pulling the tube which is a function of membrane tension. In addition, the spherical or irregular geometry of physiological cargo, which was not explored in our flat system, could also play a significant role by putting constraints on the motor-microtubule interaction thus influencing the stepping kinetics of motors (Nelson et al., 2014).

In this thesis, we show that the purified recombinant FL KIF16B is active, dimeric and moderately processive. The inhibition of KIF16B, when not bound to cargo, observed inside cells and the superprocessivity observed in *in vitro* experiments with cell extract (Soppina et al., 2014; Farkhondeh et al., 2015), thus could be due to additional factors present in the system. Biochemical and

genetic studies could be used to identify different binding partners of KIF16B, which might be influencing its transport characteristics. A potential candidate is RAB14, a small molecular G protein, which has been shown to bind directly to KIF16B on fibroblast growth factor receptor (FGFR) vesicles. Using membrane-anchored gliding motility assays we can investigate the influence of RAB14 on KIF16B transport characteristics, in the future.

Inside a cell, when motors are attached to membranous cargo, the diffusivity of the lipid allows the motors to explore its environment to engage with a microtubule, on which they walk to transport the cargo. At the same time, relatively big size of a cargo doesn't let the bound motors diffuse away in the cytoplasm. In addition, the fluidity of membrane attributes more compliance to the system, such that multiple processive motors do not inhibit each other and the cargo is transported efficiently. Moreover, our results show that the physical properties of cargo can regulate their transport mediated by multiple motors.

Defects in intracellular cargo transport have been shown to initiate and aggravate many diseases such as neurodegenerative disorders for example Alzheimer's disease, Huntington's disease (HD) and Parkinson's disease (PD) reviewed in (Hirokawa et al., 2015). Thus, it is of extreme interest to understand the role of different components involved in the complex intracellular process, to find new targets for therapeutic approaches. In the last decade, functional mechanism of various molecular motors has been extensively studied. However, the understanding of motor recruitment to specific cargo via different adaptor proteins or directly and the influence of cargo itself on the transport behavior is lacking. Our membrane-anchored gliding motility assays provide a useful tool to gain mechanistic insights into collective transport by molecular motors and their regulation by various adaptor proteins and cargo properties.

5 Materials and methods

5.1 Reagents and solutions

The chemicals used in this thesis were purchased from Sigma-Aldrich, St. Louis, MO, USA or Merck KGaA, Darmstadt, Germany, unless otherwise stated. The lipids used in this thesis were purchased from Avanti Polar Lipids, Inc., Alabaster, AL, USA. The DNA oligomers were purchased from biomers.net GMBH, Ulm, Germany. The restriction enzymes used were purchased from New England Biolabs Inc., Ipswich, MA, USA

Buffer solutions

TBE: 89 mM Tris base, 89 mM Boric acid, 2 mM EDTA, pH 8.3

H2OS75: 20 mM HEPES, 75 mM NaCl, pH 7.2

H2OS150: 20 mM HEPES, 150 mM NaCl, pH 7.2

Buffer A: 50 mM sodium phosphate buffer, 300 mM KCl, 5 % Glycerol, 1 mM MgCl₂, 10 mM β-mercaptoethanol, 0.1 mM ATP, pH 7.4

Buffer B: 20 mM HEPES, 150 mM NaCl, 0.1 mM ATP, 5 % Glycerol, 1 mM DTT, pH 7.2

Buffer C: 1 M NaCl, 25 mM HEPES, 5% Glycerol, 5 mM MgCl₂, 0.25% CHAPS, 10 mM βME, 0.1 mM ATP, 0.5 M Arginine, pH 7.2

C2OS150: 20 mM Citrate buffer, 150 mM NaCl, pH 4.8

BRB80: 80 mM PIPES, 1 mM MgCl₂, 1 mM EGTA

Dilution buffer: 0.2 mg/ml Casein, 1mM DTT, 1 mM MgATP, 0.1% Tween 20, 10 μM Taxol in H2OS75

SM buffer: 0.2 mg/ml Casein, 40 mM Glucose, 130 μg/ml Glucose Oxidase, 24 μg/ml Catalase, 0.1% Tween 20, 1mM DTT, 1 mM MgATP, 10 μM Taxol in H2OS75

SLB motor buffer: 1 mM ATP, 1 mM DTT, 20 mM Glucose in H2OS75

SLB imaging buffer: 40 mM Glucose, 13 μg/ml Glucose Oxidase, 10 μg/ml Catalase, 1 mM DTT, 1 mM MgATP, 1 μM Taxol in H2OS75

5.2 Molecular biology

Polymerase chain reaction (PCR): The reactions was set up as follows: 50 ng of DNA template, 25 pM of each primer, 0.5 µl of polymerase (# 11732641001 Expand High Fidelity, PCR system, Sigma-Aldrich), 5 µl of 10x PCR buffer, 1.5 µl of 10 mM dNTPs (# 39053 Biotline) were mixed with ddH₂O to a total volume of 50 µl. The PCR reaction was carried out in Mastercycler pro, with the following conditions: denaturation for 5 min at 95 °C, followed by 20 cycles of denaturation (95 °C, 0.5 min), annealing (60 °C, 0.5 min), and elongation (68 °C, 2 min for each kb of GoI). The reaction was terminated by a final elongation at 72 °C for 7 min. The product of the reaction was then run on an agarose gel and the band of the correct size was cut and the DNA from the agarose gel cuts were extracted using Qiagen gel extraction kit and protocol. The DNA was eluted with ddH₂O.

Agarose gel electrophoresis: 0.8 % (w/v) agarose solution in Tris/Borate/EDTA (TBE) buffer was prepared by dissolving 4 g of agarose (electrophoresis grade Invitrogen) in 500 ml of TBE buffer. The agarose was dissolved in the buffer by bringing the solution to boil in a microwave with intermittent swirling until a clear solution was formed; usually it took about 2-3 minutes at 900 W. Once agarose was dissolved in the buffer the solution was cooled to less than 60 °C before casting the gel. 60 ml of the solution was taken in a beaker to which 3 µl of RedSafe dye (# 21141, iNtRON Biotechnology, Inc) was added and gently mixed. The agarose solution was then poured into a gel tray (Bio Rad) and a comb was inserted to about half the thickness of the gel to form sample wells. The gel was allowed to cool until it solidified after which it was immersed in the TBE buffer. 5x loading dye (# 239901, Qiagen Gel pilot loading dye) was added to the samples and DNA marker, which were then loaded in the wells. The gel was run for 40 min at 120 V. Afterwards, the gel was placed under UV trans-illuminator at 355 nm, wavelength to visualize and analyze the DNA bands.

Restriction: All restriction digests were carried out using NEB (New England Biolabs Inc.) restriction enzymes, and buffer. 30 μ l of gel purified PCR product was mixed with 5 μ l of 10x NEB buffer 4, 13 μ l of ddH₂O, and 1 μ l each of restriction enzyme NotI-HF and AscI were added to the mix. The mix was then incubated overnight at 37 °C and cleaned next day with Qiagen PCR purification kit and eluted with 30 μ l of ddH₂O.

Ligation: DNA ligation was setup using T4 DNA ligase from Promega Fast ligation kit (# M8221, LigaFast™ Rapid DNA Ligation System, Promega). The ligation reaction was set up by mixing 5 μ l of 2x ligation buffer, 0.5 μ l of pre-cut destination vector, 2 μ l of cut PCR product and 1 μ l of ligase adding ddH₂O to a total volume of 10 μ l. The mix was then incubated overnight in a standing fridge at 10 °C – 12 °C.

Transformation: Plasmid-DNA was transformed into chemically competent *E. coli* XL10 gold cells (Agilent Technologies) for plasmid DNA amplification. Ligation mix was added to, at least, 60 μ l of cell suspension and mixed gently by tapping on the tube. A negative control without any plasmid added to the cell suspension was also prepared. The mix was incubated on ice for 30 minutes. The cells were heat shocked for 45 s at 42 °C and moved back to ice. 1 ml of rich media (SOC) was added to the tubes and incubated at 37 °C for 1 hour. The cells were spun down in a tabletop centrifuge (Heraeus Biofuge Pico-tabletop centrifuge) at 3000 rpm for 5 min. Supernatant is decanted and cell pellet was re-suspended in 100-150 μ l of media and spread on the pre-warmed dry Luria-Broth (LB) agar plate with appropriate antibiotic. The plates were then incubated overnight at 37 °C.

Plasmid mini-prep: 6 colonies were picked from each plate using 1 μ l inoculation loop and inoculated into 4 ml of LB media with appropriate antibiotics. The cells were grown overnight and the DNA was extracted from the cells using Qiagen mini-prep kit. The plasmid DNA was eluted in 50 μ l ddH₂O and the final concentration of DNA is measured using nanodrop spectrophotometer. To determine whether the plasmid contains the GoI, digestion was set up with 2 μ l of plasmid prep, 1 μ l of NEB buffer 4, 6 μ l of water and 0.3 μ l each of

restriction enzymes NotI-HF and Ascl. The digestion mix was incubated for 3 hours at 37 °C and the samples were run on a 0.8% agarose gel to analyze whether they have the correct size. The plasmid prep which had the correct size were then sequenced using standard primers such as T7, eGFP, pFastBac both in forward and reverse directions, at the sequencing facility of the MPI-CBG, Dresden, Germany.

Kinesin-1 constructs: Two kinesin-1 constructs were created for this thesis, rKin430-SBP and rKin430-SBP-GFP

For preparation of rKin430-SBP, a codon optimized gene sequence of rat kif5C, truncated to first 430 amino acid with the tags 8xHis, mCherry and SBP, was purchased from Invitrogen (GeneArt, gene synthesis, Invitrogen). Two restriction sites, PacI and Ascl, were introduced in pET24d vector (#69752-3, Addgene) and rKin430-mCherry-SBP sequence was inserted in the vector using PacI and Ascl restriction enzymes. mCherry sequence was cut out using the restriction enzyme NgoMIV and the cut plasmid was ligated to get the rKin430-SBP plasmid.

rKin430-SBP-GFP construct was prepared by inserting a multifunctional green fluorescent protein (mfGFP) tag (Takuya Kobayashi) having octa-histidine (8xHis), SBP, and c-Myc tag, in tandem in a loop of GFP sequence. The sequence was a gift from Murayama Lab, JUSM, Tokyo, Japan, which was inserted into rKin430 construct (K. R. Rogers et al., 2001), a gift from Rob Cross Lab, Warwick Medical School, UK in pET17 vector (# 69663-3, Addgene). Briefly, mfGFP sequence was amplified and restriction sites KpnI and MfeI were added at the 5' and 3' end of the complementary sequence, respectively. mfGFP sequence was inserted into rKin430 plasmid using restriction enzymes KpnI and MfeI.

Both the constructs were expressed and purified from *E. coli*.

Kif16B constructs: FL KIF16b gene sequence in pFastBac vector was a gift from Zerial lab, MPI-CBG, Dresden, Germany. NotI and Ascl restriction sites were introduced in the gene of interest (GoI) for different constructs, listed in (Table 5.1), and amplified using PCR. The GoIs were inserted into different pOCC

vectors, which were developed by Aliona Bogdanova at the PEP facility at MPI-CBG by modifying pOET transfer plasmids, (Oxford Expression Technologies). FL KIF16B insert was shuffled into different pOCC destination vectors with the restriction sites NotI and Ascl. The chimeric construct with PX domain after the motor head 16B400-PX and 16B429-PX, were prepared by first amplifying the motor head sequence using primers with restriction sites NotI and BamHI and PX domain with restriction site BamH1 and Ascl, gel purified PCR products were then ligated together with cut pOCC16 vector. Purified plasmid DNA and modified parts including inserted genes were sequenced at the sequencing facility, MPI-CBG Dresden. Sequences were analyzed using A plasmid editor software (APE).

Table 5.1 | Plasmids used in this study. Insert gives the name of the protein encoded on the expression vector.

S. No.	Insert	Vector backbone	N-terminal tag	C-terminal tag	Resistance	Expression System
1	rKin430	pET24d	-	8xHis, SBP	Kanamycin	Bacteria
2	rKin430	pET17b	-	mfGFP	Ampicillin	Bacteria
3	FL KIF16B	pFastBac	6xHis, eGFP	-	Ampicillin	Baculovirus
4	FL KIF16B	pOCC16	6xHis	eGFP	Ampicillin	Baculovirus
5	FL KIF16B	pOCC112	-	eGFP, MBP	Ampicillin	Baculovirus
6	16B-400	pOCC16	6xHis	eGFP	Ampicillin	Baculovirus
7	16B-400-PX	pOCC16	6xHis	eGFP	Ampicillin	Baculovirus
8	16B-429	pOCC16	6xHis	eGFP	Ampicillin	Baculovirus
9	16B-429-PX	pOCC16	6xHis	eGFP	Ampicillin	Baculovirus
10	PX	pET24d	-	eGFP	Kanamycin	Bacteria

FL KIF16b, FL KIF16b-GFP, 16B-400-GFP, 16B-400-PX-GFP, 16B-429-GFP, 16B-429-PX-GFP, were expressed in the insect cells using baculovirus expression plasmids (pOCC). PX domain 1185-1318 a.a, was expressed and purified from *E. coli*.

5.3 Protein expression and purification

Bacterial system

Plasmid DNA, with a gene of interest, was transformed into *E. coli* Bl21 pRare competent cells, modified from (# 230280, Stratagene) to have rare codons. 1 μ l (~200ng/ μ l) of plasmid DNA was added to, at least, 60 μ l of cell suspension and mixed gently by tapping on the tube. A negative control without any plasmid added to the cell suspension was also prepared. The mix was incubated on ice for 30 minutes. The cells were heat shocked for 45 s at 42 °C and moved back to ice. 1 ml of rich media (SOC) was added to the tubes and incubated at 37 °C for 1 hour. The cell suspension was spun down in a tabletop centrifuge at 3000 rpm for 5 min. Supernatant was decanted and cell pellet was re-suspended in 100-150 μ l of media and spread on pre-warmed dry LB agar plate with appropriate antibiotic. The plates are then incubated overnight at 37 °C. Individual colonies were then picked and transferred to separate 15 ml air exchanging Falcon tube with 5 ml LB media and incubated overnight in a shaker at 200 rpm, 37 °C to prepare a pre-culture. All media used contained the appropriate selective antibiotics: Ampicillin 100 μ g/ml, Kanamycin 30 μ g/ml and Chloramphenicol 34 μ g/ml respectively. 5 ml of pre-culture was transferred into 750 ml of 37 °C pre-warmed LB media with appropriate antibiotics in a sterile 2.8 L flask. The cells were grown on a shaker at 200rpm, 37 °C until the optical density at 600 nm reached ~ 0.5 (1 cm path length cuvette, UV-Spec Agilent). 2 or 3 glycerol cell stocks were prepared at this time point, by adding 0.6 ml of cells to 0.4 ml of 60 % glycerol in a fume hood and flash freezing them in liquid nitrogen. These stocks were then stored at -80 °C to be used later to prepare fresh pre-cultures. Remaining cell culture was cooled to 18 °C by keeping the flask on a bed of ice in a 4 °C cold room. The protein expression was induced by adding IPTG to a final concentration of 0.5 mM. The cells were incubated overnight in a shaker at 200 rpm, 18 °C. Cells were harvested the next day by centrifuging the cell culture at 7500x g for 10 minutes at 4 °C in a centrifuge (Beckman Coulter Avanti J-20 centrifuge with JLA8.1000 rotor). The supernatant is discarded and the cells are

re-suspended in equal amount of PBS buffer with 10 % Glycerol. All the purification steps were performed at 4 °C.

Cell Lysis: Harvested *E. coli* cells were re-suspended in 40 ml in buffer A supplemented with 30 mM Imidazole, and 1 Protease inhibitor cocktail tablet (cOmplete, EDTA free, Roche). The cell suspension was lysed by passing through 4-5 times in an Emulsiflux french press. The lysate was poured in a cold Beckman centrifuge bottles (# 355622, 70 ml) cleared of cell debris by centrifuging at 40,000 rpm for 1 hour at 4 °C in a Beckman optima LE80K Ultracentrifuge.

Histadine affinity purification: Supernatant containing the soluble protein was purified using the nickel-sepharose affinity chromatography. His-trap column (GE Healthcare 1 ml # 17-5247-01) is equilibrated with 10 column volume (CV) of buffer A. The protein was loaded on to the column by flowing the supernatant through the column at a flow rate 1ml/min. The column was washed with buffer A supplemented with 60 mM Imidazole. After the first wash step, the column was washed with high ATP buffer to get rid of heat shock proteins (buffer A supplemented with 5 mM ATP, 2 mg/ml of any denatured protein). Protein of interest was eluted by flowing elution buffer (buffer A + 300 mM Imidazole) and 0.5 ml fractions were collected. The eluted fractions were quickly checked qualitatively for protein concentration using Bradford reagent (10 µl eluted fraction + 200 µl 1x Bradford reagent). The fraction that gave the most intense blue color was desalted in buffer B using desalting column (PD 10 desalting column, # 17-0851-01). The desalted fraction were then dispensed into eppendorf tubes as 5 µl aliquots flash frozen in liquid nitrogen and stored at – 80 °C.

Baculovirus system

Recombinant baculovirus were prepared by co-transfecting *Spodoptera fugiperda* (SF+) cells with a defective bacmid plus a rescue bacmid with the gene of interest. Recombinant virus DNA, for all the constructs were made by Régis Lemaitre, at the PEP facility, MPI-CBG. The protocol is outlined below:

Generation of recombinant baculovirus: In a 24 well plate, 2 μ l of bacmid DNA + 2 μ l of pOEM construct were diluted in 800 μ l of serum free medium for each transfection reaction. 12 μ l of homogenized Escort IV reagent (# L3287, Sigma-Aldrich) was then added to the mix. The mix is incubated for 45 min at room temperature to allow DNA complex formation. All transfections were done in duplicates. Negative controls with “no pOEM construct” as well as “serum free medium” were also set up. Afterwards, 200 μ l of SF+ cells (5×10^6 /ml) were added to each transfection well. The plate was covered with BreathEasy tape (Z380059, Sigma-Aldrich) and the edges were sealed with parafilm (Bemis NA, USA). The plate was put on a shaker overnight at 200 rpm, 27 °C. 1 ml of complete medium was added the next day to each transfection well. The cells were checked under microscope after 48-72h – baculovirus infected cells stop growing compared to the negative controls and have larger diameter (~22 vs. 18 μ m) with a rough cell outline. The viruses were collected after shaking for ~ 80 hours. Cells in the 24 well plates were centrifuged (Heraeus Multifuge 3 SR) at 300x g for 5 minutes. The supernatant was passed through 0.45 μ m filter and stored in 2 ml eppendorf tube. The stock is referred to as first passage or P1, which can be stored in dark at 4 °C for short-term usage. 10% glycerol was added to the P1 stock and stored at -80 °C for long-term storage.

Virus stocks were expanded by another passage for increasing the amount of virus titer to be used for protein expression. 25 μ l of P1 virus stock was added to 100 ml of SF+ cells at 0.5×10^6 /ml with 2% of Fetal Brain Serum. The cells are incubated in a shaker for 4-5 days, at 180 rpm and 27 °C. The cells are pelleted in a centrifuge (Beckman JA12) at 4500x g for 15 minutes. The supernatant is collected and passed through 0.45 μ m filters. P2 or passage 2 stock can be used for up to 6 months if stored in dark at 4 °C.

Time course: To check the optimal expression time for different constructs, time course was performed to obtain the peak protein expression. P2 stock was added to 50 ml of 1×10^6 /ml of SF+ cells in a ratio 1:100. The cells were incubated in a shaker at 180 rpm and 27 °C. 200 μ l samples were collected every 24 hours post infection. Samples were centrifuged at 500x g for 5 min, in the tabletop centrifuge (Heraeus Biofuge Pico-tabletop centrifuge). The cell pellet was then

re-suspended in 200 μ l of Phosphate Buffer Saline (PBS). The amount of protein expressed in the cells at different time points was determined by running a SDS PAGE, and analyzing the band intensity. Thus, the optimal time for peak protein expression was obtained, which was then used for large-scale protein expression.

MBP affinity purification: MBP tagged proteins were expressed by adding 5 ml of appropriate P2 virus stock 1×10^6 /ml of SF+ cells and incubating in shaker at 180 rpm, 27 °C for the time period obtained from the time course experiments, usually around 60-65 hours. The cells were then harvested by centrifugation (Heraeus Multifuge 3 SR) at 300 x g for 12 minutes. The supernatant was discarded and the cell pellet was re-suspended in equal amount of PBS buffer with 10 % Glycerol. The cell suspension at this time was either used for purification straight away or stored at - 80 °C as cell pearls, the suspension was poured drop wise in liquid nitrogen to form pearls, to be purified later.

All the purification steps were performed at 4 °C. The cells were thawed on ice and suspended in 25 ml buffer C supplemented with 50 μ l PI cocktail (# 535140, Calbiochem, Merck) and 1ul Benzonase. The cell suspension was then homogenized in a dounce homogenizer for cell lysis. The lysate was then cleared of cell debris by centrifuging at 40,000 rpm for 1 hour at 4 °C in a Beckman optima LE80K Ultracentrifuge. The supernatant containing protein of interest, was then incubated with 3 ml of pre-washed amylose resin (# E8021S, NEB) for 3 hours in cold room. The solution was then passed through an empty gravity flow column (# 732 1010, Econo-Pac chromatography columns, Biorad) to separate the beads from buffer. The beads, loaded with protein of interest, were then washed twice with 10 ml of buffer C. The protein was eluted from the resin by incubating the beads with 3 ml of buffer C supplemented with 20 mM Maltose, for 10 min by closing the end of column after which 1ml protein fractions were collected.

MBP tag cleavage: MBP tag of FL KIF16B was cleaved using His-PreScission protease (Protein expression and purification facility, MPI-CBG, Dresden). Eluted protein fractions were diluted to 10 ml with buffer C and incubated with 50 μ l of

protease (1 mg/ml) overnight. To remove the His-PreScisson protease, cleaved His tag from the cleaved fractions, they were incubated with 1 ml of pre-washed Ni-NTA resin (# 30210, Qiagen) for one hour. The solution was passed through empty gravity flow column to separate the resin. The flow through was concentrated to 1 ml by spinning through 30K Amicon Ultra centrifugal concentrator units (Millipore). The concentrated protein were then dispensed into eppendorf tubes as 5 μ l aliquots flash frozen in liquid nitrogen and stored at -80°C .

Gel filtration chromatography: For analytical size-exclusion chromatography, 0.5 ml of MBP affinity purified FL KIF16b fraction after cleavage reaction was applied to a 24 ml Superose 6 column (# 17-5172-01, GE healthcare life sciences) on an AKTA Ettan liquid chromatography system. The column was pre-equilibrated in the equilibration buffer. The samples were run with a flow rate of 0.4 ml/min at room temperature and 0.5 ml fractions were collected. For calculation of apparent molecular weight a standard with tyroglobulin 660 kDa and BSA 67 kDa were applied at same conditions. Absorbance at 280 nm and 488 nm for eGFP constructs were recorded and the fractions under the peak were analyzed with an SDS-PAGE.

His tag cleavage: His tag of shorted KIF16B constructs, purified with Histadine affinity purification (see page 105), was cleaved using His-PreScisson protease. Eluted protein fractions were diluted to 10 ml in buffer C and incubated with 50 μ l of protease (1 mg/ml) overnight. The solution was incubated with 1 ml of pre-washed Ni-NTA resin for one hour to remove His- PreScisson protease and the His tags. The protease, cleaved His tag and other unspecific proteins, which were co-eluted in the first step bind to the resin. The resin was separated from the solution by passing it through empty gravity flow column and the flow through was concentrated to 1 ml by spinning through 30K Amicon Ultra centrifugal concentrator units (Millipore). The concentrated protein were then dispensed into eppendorf tubes as 5 μ l aliquots, flash frozen in liquid nitrogen and stored at -80°C .

Sodium dodecyl sulphate - Poly acrylamide gel electrophoresis (SDS-PAGE): Purified protein fractions were analyzed with SDS_PAGE for purity and concentration measurement. 5 μ l of SDS loading buffer (1 ml 3.75 M Tris pH 6.8, 1.2 ml 25% SDS, 5 ml Glycerol, 1.5 ml β -mercaptoethanol and 0.45 mg bromophenol blue in 10 ml) supplemented with 0.1 M DTT was added to 20 μ l of sample. The samples were boiled for 10 min at 95 °C to denature all the proteins. 10 μ l of the denatured sample was loaded on the gel either 4-12 % bis-tris gel (#NPO322BOX, life technologies) for kinesin-1 construct and shorter KIF16B constructs or 3-7% Tris acetate gel (#EA03555BOX, life technologies) for FL KIF16B constructs. Appropriate protein marker was always added to at least one of the wells to compare the molecular weight.

Running condition for 4-12% bis-tris gel

1x MOPS buffer (Invitrogen); 200 V constant for 45-50 minutes

Running condition for 3-7% tris acetate gel

1x Tris acetate buffer (Invitrogen); 150 V constant for 60 minutes

Gels were stained with SimplyBlue SafeStain (Invitrogen # LC6065)

Western blot analysis: Proteins from SDS PAGE were transferred on to a nitrocellulose membrane (# IB3010-02, Invitrogen) using an iBlot gel transfer device (Invitrogen). iBlot Western detection, Chromogenic kit (Anti-mouse) (#IB7310-02, Invitrogen) was then used to develop a western blot using the iBlot gel transfer device. Mouse anti-GFP (# 11814460001, Roche) or anti-His (# A00186-100, Genscript) was used as primary antibody.

Protein concentration measurement

Protein concentration was determined by Bradford assay and by analyzing the protein bands intensity on a SDS PAGE using ImageJ.

Bradford assay: 10 μ l of protein sample in elution buffer was added to 1 ml 1x Advance Protein Assay reagent (# ADV01-A, Cytoskelton) and the optical density recorded at 570 nm. Calibration curve was obtained by fitting a linear curve to the OD₅₇₀ of BSA samples at different concentrations ranging from 0 to 1 mg/ml in the elution buffer. Average background was calculated from the blank samples and subtracted from the protein sample raw data. Protein

concentrations were then calculated for each dilution and averaged to get mean protein concentration.

Quantifying protein bands in an SDS Page: BSA or His-eGFP standards with a known protein concentration along with different dilutions of protein samples were run on a SDS PAGE gel. The gels were scanned with a high quality scanner (Espon Perfection V750-M Pro scanner) and the integrated intensity of protein bands was quantified using ImageJ. A rectangular area was selected covering the first lane and then subsequent lanes were selected with the same rectangular selection. The intensity profile plots of selected lanes were drawn using the 'analyze gel' function of ImageJ and the integrated intensities were recorded by calculating the area under the peaks. Calibration curve was then obtained from the linear fit to the integrated intensity for different concentration of standard. Protein sample concentration were then calculated for each dilution and averaged to get mean protein concentration.

5.4 *In vitro* motility assays

Flow Cells Preparation: Stepping motility assays and surface-immobilized gliding motility assays for kinesin motors were performed in 1.5 to 2 mm wide flow cells. Flowcells were prepared by cutting four parafilm stripes of about 25x2 mm² and sandwiching them in between the 22x22 mm² at the bottom and 18x18 mm² glass coverslips (#1.5, Gerhard Menzel Glasbearbeitungswerk GmbH & Co. KG, Braunschweig, Germany) on top. The parafilm was heated for 10 seconds at 60 °C and two slides were gently pressed together to form 3 leak proof channels of area ~ 2x18 mm². Overhanging parafilm was cut using a scalpel. Depending on the requirements of the respective experiments, glass coverslips were either made hydrophobic by silanization or made hydrophilic by the easy clean procedure followed by plasma cleaning. The methods followed are described in the following sections.

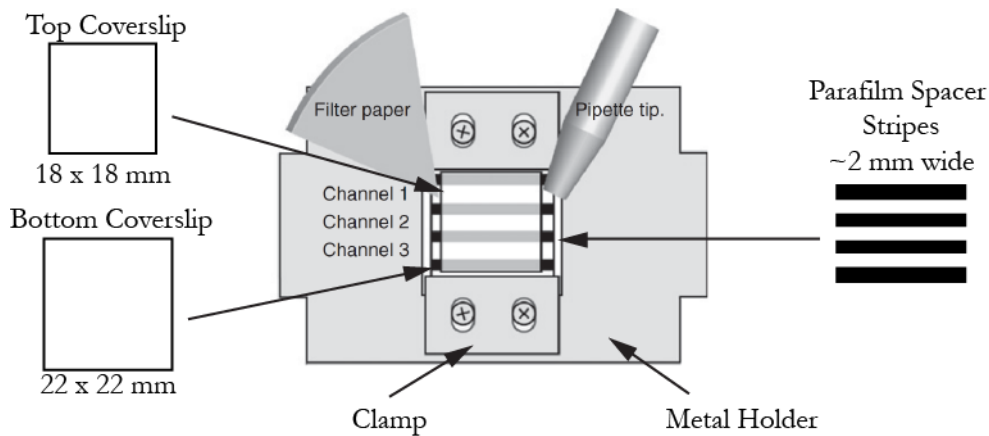


Figure 5.1 | Schematic of flow cells used for stepping motility assays and conventional gliding motility assays. The top and bottom coverslips with parafilm spacer stripes in between to form channels and placed into a custom-made holder. The solutions are flushed in the channels via pipetting and perfusion with filter paper as shown. Adapted from (Gell et al., 2010)

Dichlorodimethylsilane (DDS) coating of coverslips: Glass coverslips were soaked in acetone solution for 30 min followed by 20 min sonication. The coverslips were then rinsed with deionized water and thereafter treated with piranha solution, 75 ml hydrogen peroxide (30%) + 175 ml sulphuric acid (70%), at 60 °C for an hour. The coverslips were then thoroughly rinsed with nanopure water and soaked in 0.1 M potassium hydroxide for 15 minutes. The coverslips were then again rinsed with nanopure water and dried completely with pressurized air. The coverslips were then put in a solution of 250 ml Trichloroethylene (Merck) with 125 μ l of DDS for an hour. The coverslips were then sonicated in methanol first for 5 min and then 15 min exchanging methanol solution in between. Finally the coverslips were thoroughly rinsed with nanopure water, dried with pressurized air and stored in an airtight glass box. The coverslips were then used within a month period.

Preparation of microtubules: Tubulin was purified from porcine brain according to protocol as described in the publication (Gell et al., 2011). To obtain fluorescent microtubules tetramethyl rhodamine (TAMRA) labeled tubulin heterodimers were mixed with unlabeled tubulin heterodimers in 1:3 molar ratio. Taxol stabilized GTP microtubules were prepared by polymerizing 32 μ M

tubulin mix in 1 mM GTP, 5 % DMSO, 5 mM MgCl₂ at 37 °C for 30 min in BRB80 buffer. The polymerization was carried out in a total volume of 6.25 µl. After incubating for 30 min, the microtubules were stabilized with taxol by adding 10 µM of taxol in BRB80 to a final volume of 200 µl. To get rid of free tubulin taxol stabilized microtubules were spun down, with 60 % glycerol cushion at the bottom of the centrifuge tube, in an airfuge (Air driven ultracentrifuge, Beckman Coulter) at 100,000 x g for 10 min. The supernatant was discarded and the pellet was re-suspended in BRB80 supplemented with 10 µM taxol.

Taxol stabilized GMP-CPP microtubules (DS-MT) were prepared by polymerizing 2.5 µM tubulin mix (1:3/TAMRA tubulin: unlabeled tubulin) in BRB80 buffer supplemented with 1.25 mM GMP-CPP, and 1.25 mM MgCl₂. The polymerization was carried out at 37 °C for 2 hours in 80 µl BRB80. Free tubulin was removed by ultracentrifugation. The pellet was re-suspended in BRB80 supplemented with 10 µM taxol.

Stepping motility assay: Experiments to obtain the stepping velocity of kinesin motors (kinesin-1 and KIF16B constructs) at single-molecule level were performed in flow cells made of silanized coverslips. The channels formed in the flow cells were washed with a sequence of buffers to allow fluorescent MTs to bind to glass substrate and subsequently motors were flushed in to observe their interaction with the MTs. First, a solution of 10,000x diluted 0.1 µm Tetraspeck beads (# T-7279, Invitrogen) were flushed into a channel using vacuum suction and incubated for 2 min. The Tetraspeck beads adsorbed on the bottom of glass cover slip and later used for stage drift correction. Following that a solution of β-tubulin antibodies (0.5% SAP.4G5, Thermo Fisher Scientific) diluted in H2OS75 was incubated for 5 minutes, followed by a washing step with H2OS75. The channel was then incubated with 1% Pluronic F127 in H2OS75 for 45 minutes to block the surface from unspecific binding of proteins. Subsequently, the channels were washed with 80 µl of H2OS75 supplemented with 10 µM taxol (H2OS75T). A solution of MTs was flushed in and allowed to attach to the antibodies on coverslips for 5 minutes. Unbound MTs were removed from channel by washing

with 40 μ l of H2OS75T. Finally, 20 μ l of 100 pM GFP labeled rKin430-SBP in SM buffer were flushed into the channel.

Kinesin-1 pull-down assay: For gliding assays with kinesin-1 constructs additional purification step was carried out to remove motor clusters and inactive motors. 25 μ M of motors were incubated for 5 minutes with taxol stabilized microtubules (\sim 30 μ M) in presence of 0.1 mM AMP-PNP. As a result, all the active motors were rigidly bound to microtubules, which were pulled down by ultracentrifugation at 100,000 x g for 5 minutes. The microtubule pellet was then re-suspended in H2OS75 buffer with 1 mM DTT and 1 mM ATP for 10 minutes. This releases all the active motors, rigidly bound to the microtubules. The microtubules then were spun down and the supernatant containing active motors was used for gliding assay. The protein concentration in supernatant was measured by quantifying the band intensity in a SDS PAGE.

Gliding motility assay on surface-immobilized kinesin motors: Experiments to obtain the multi-motor transport velocity of rigidly bound kinesin motors were performed in flow cells as described above. After flushing in tetra speck beads (diameter 0.1 μ m) with vacuum suction, a solution consisting of 20-22 μ g/ml antigen binding fragments of antibodies (FABs) from anti-mouse IgG (Fc Specific) Antibody (Sigma Aldrich) in H2OS75 was flushed in the channel. The solution was washed out of the channel with buffer after 5 min incubation. The channel was then incubated with 1% Pluronic F127 in H2OS75 for 20 minutes to block the surface from unspecific binding of proteins. Subsequently the channel was washed with 80 μ l of H2OS75 with 10 μ M taxol. 20 μ l of His tag antibodies (10 μ g/ml) were then flushed into the channel. His tag antibodies bind specifically to the Fc region of the Fab fragments. After 10 min incubation the channel was washed with 40 μ l of dilution buffer and the motor solution (1 – 100 μ M) in dilution buffer was flushed into the channel. After 5 min incubation and subsequent washing with the SM buffer double stabilized microtubules were flushed into the channel. After 5 min of incubation the channel was flushed with the imaging buffer to remove the microtubules, which didn't attach to the surface-immobilized motors to reduce the background while imaging.

Membrane-anchored gliding motility assays

Reaction chambers: Membrane-anchored gliding motility assays were performed in chambers, prepared by attaching a cut PCR eppendorf tube to the plasma-cleaned coverslip using UV adhesive (NOA 83, Norland products). The reaction chamber was then put under a UV lamp for 10 min to cure the adhesive. This ensured that the chambers formed were leak-proof.

Cleaning of coverslips: 24 x 60 mm Glass coverslips (#BB024060A1, 1.5, Gerhard Menzel GmbH, Germany) were cleaned by sonicating in 2% Mucosol for 15 min followed by 10 min sonication in pure ethanol with an intermediate rinsing of coverslip with ultrapure water. Finally the coverslips were rinsed with ultrapure water and dried completely under stream of nitrogen. These coverslips were then placed in an airtight container and used with in two weeks.

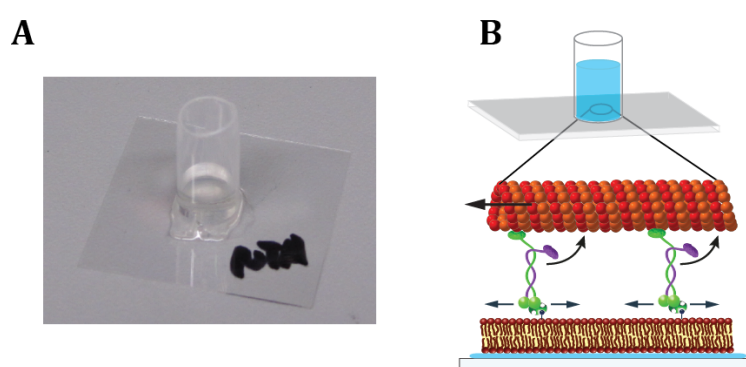


Figure 5.2 | Reaction chambers used for the membrane-anchored gliding motility

A) Photograph of a reaction chamber, prepared by attaching the cut eppendorf on a plasma-cleaned cover slip using UV adhesive. B) Schematic of membrane-anchored gliding motility assay in a reaction chamber.

Supported Lipid Bilayer (SLB) formation: The formation of SLBs is divided into three steps

- a) Preparation of multi-lamellar vesicles (MLVs)
- b) Preparation of small uni-lamellar vesicles (SUVs)
- c) Deposition of SUVs on coverslips to form SLBs

The composition of SLB used for the experiments with rkin430-SBP constructs was DOPC: DSPE-PEG (2000) Biotin: DOPE Atto647n (# AD647N-16, Atto-Tec fluorescent labels and dyes) in the molar ratio 99:1:0.005 referred to as 1% SLB.

The composition of phase separated SLB used for the experiments with rkin430-SBP constructs were DOPC: DSPE-PEG (2000) Biotin: bSM: Chol: DOPE Atto647n in molar ratio 37:1:36:26:0.005 referred to as 1% phase separated SLB.

Preparation of MLVs: Lipid dissolved in chloroform were transferred to glass vial, in the required molar ratio, with a total of 7.5 μ g total lipids for preparation of a single 1% SLB. The solvent was evaporated under a gentle stream of nitrogen while rotating the glass vial to form a uniformly thin lipid film on the wall of a glass vial. Any residual solvent was further removed by drying the lipid film in a vacuum overnight. The lipids were then rehydrated in H2OS75 buffer to a lipid concentration of 1.5 mg/ml. MLVs thus formed were stored at -20 °C as 20 μ l aliquots and used within a month.

Preparation of SUVs: SUVs were prepared by diluting a MLV aliquot to 0.2 mg/ml and sonicating it in a bath ultra-sonicator (# 142-6002, VWR USC300TH) for 20 min, this causes repetitive breaking of MLVs and formation of SUVs due to shear forces. The size of SUVs thus formed is in the range of 40-70 nm, checked with dynamic light scattering.

Deposition of SUVs on coverslips to form SLBs: Before deposition of SUVs, easy cleaned glass coverslips were plasma cleaned, to make surface hydrophilic, in plasma cleaner (FEMTO plasma cleaner, diener electronic), in presence of oxygen for 6 min. SUV dispersion was then added to the reaction chamber and CaCl₂ was added to a final concentration of 3 mM to induce fusion of SUVs and the formation of supported lipid bilayer on the glass surface. After 45 min of incubation at room temperature, the sample was washed with 1 ml of H2OS75 buffer in steps of 50 μ l to remove the unfused vesicles.

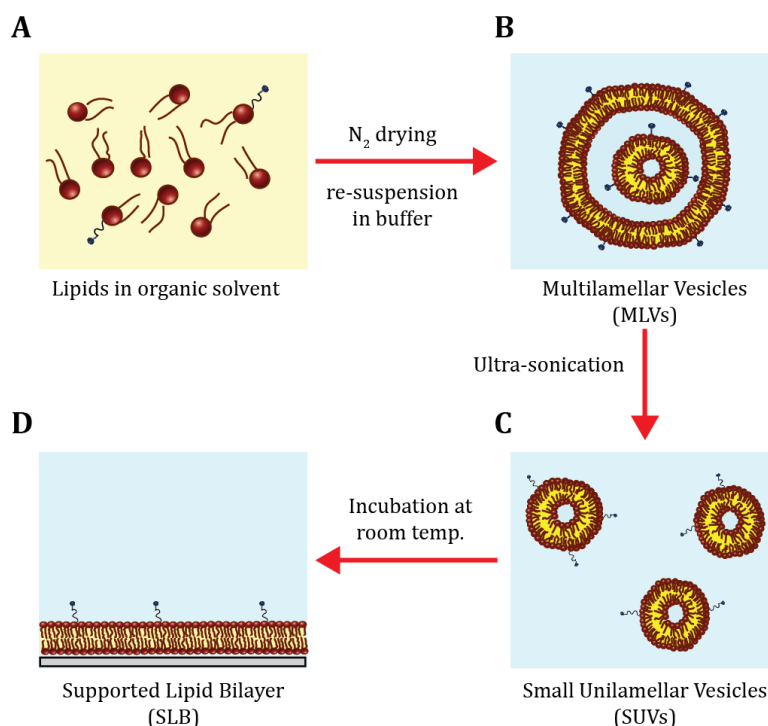


Figure 5.3 | Schematic of steps involved in SLB formation. A) The lipid mix in chloroform is completely dried to remove the solvent and B) rehydrated in H₂O/S75 for the formation of MLVs. C) SUVs are formed by ultrasonication of the MLVs which are then deposited on a hydrophilic glass cover slip for the formation of D) SLBs. Adapted from (Fischer, 2010)

Phase separated SLBs: For preparation of 1% phase separated SLBs the above mentioned steps were performed with following changes.

- The lipid were rehydrated with pre-warmed H₂O/S75 buffer at 65 °C.
- SUVs were formed from MLVs suspension by bath sonicating them at 65 °C for 20 minutes.
- The reaction chamber was placed on the heat block at 65 °C before adding the SUV suspension to the chamber. Washing steps were performed on the heat block and then the chamber was slowly cooled, until it reached room temperature, by removing the metal block from the heater and placing it on the bench.

PI(3)P SLB formation: The composition of SLB used in experiments with FL KIF16B were DOPC: DOPE: C18-1 PI(3)P: DOPE Atto647n in the molar ratio 77:20:3:0.005 referred to as 3% PI(3)P SLB. All the steps for formation of 3%

PI(3)P SLB were performed in C20S150 buffer. The same procedure as described for 1% SLBs was performed with one change which was no calcium ions were added for the formation of PI(3)P SLBs as they interfered with the rupture of PI(3)P SUVs on the substrate (Braunger et al., 2013).

F127 treatment: After the formation of PI(3)P SLBs they were incubated with 0.5 % F127 for 60 minutes at room temperature and washed with 1 ml of citrate buffer in steps of 50 μ l to remove the unfused SUVs. Prior to addition of motor protein KIF16B the buffer in the reaction chamber, with SLBs, was exchanged by washing with 1 ml of H20S75 buffer in steps of 50 μ l.

Membrane-anchored gliding motility assays with kinesin-1

After checking for homogeneity and diffusivity of 1% SLBs. The SLBs were incubated with 1 μ g streptavidin (SA) in 100 μ l total volume for 10 min followed by washing with 1 ml of H20S75 buffer in steps of 50 μ l, to remove the unbound SA and 3 wash steps with 50 μ l of SLB motor buffer, to equilibrate SLBs with the buffer in which motors were added to the system. 50 μ l of buffer in the reaction chamber was then replaced with 50 μ l of motor solution, consisting of motors in SLB motor buffer. The experiments were performed for different concentration of motors in different reaction chambers. The motors were always incubated, with SA loaded 1% SLB, for 6 min after which the chamber was washed 4 times with 50 μ l SLB imaging buffer to remove unbound motors. Finally, 4 μ l of fluorescent microtubules were added to the reaction chamber.

Lipid coating of silica beads: 3% PI(3)P SUVs were prepared as described earlier with a final lipid concentration of 0.25 mg/ml. 50 μ l of 1 μ m or 2 μ m diameter silica beads stock solution were washed rigorously with H20S75 buffer and re-suspended in 150 μ l H20S75 buffer. The beads were then passed ten times through a 22G needle and sonicated in an ultra sonicator for 5 minutes to dissolve the silica beads aggregates. 40 μ l of beads were then incubated with 10 μ l of SUVs, in 100 μ l H20S75 buffer, on a shaker at 850 rpm for 60 minutes. The suspension was then washed four times with H20S75 buffer by centrifuging the beads at 2000 rpm on a tabletop centrifuge and re-suspending the pellet in the

buffer. The suspension was passed ten times through a 22G needle after each step to reverse the aggregation of silica beads. The silica beads were imaged under the microscope to check for the lipid coating and incubated with an appropriate dilution of KIF16B motor for experiments.

5.5 Image acquisition and data analysis

Fluorescence images were obtained using a Nikon Eclipse Ti microscope equipped with Perfect Focus System (PFS) and a FRAP module, with a 1.49 PlanApo 100x oil immersion objective lens. (i) Gliding motility assays were observed by epi-fluorescence where rhodamine labeled microtubules were excited with a metal arc lamp (Intensilight, Nikon) and filter sets for rhodamine was used (exec: 555/25. Dichroic LP 561, em: 609/54). For gliding motility assays images were recorded for 200 frames at a rate of 1 frame per second with an exposure time of 100ms using electron multiplying charge-couple device (EMCCD) camera (iXon ultra EMCCD, DU-897U, Andor) in conjunction with NIS-Elements (Nikon) software. (ii) SM imaging for stepping assays, and SPT were performed using TIRF microscopy and monolithic laser combiner (Agilent MLC 400) which has the dual out for FRAP and fluorescence imaging. SLBs were imaged with Cy5 filter set (exec: 642/20. Dichroic LP 647, em: 700/75) and GFP molecules were imaged with filter set (exec: 475/35. Dichroic LP 491, em: 525/45). Images were acquired in continuous streaming mode with 100 ms exposure for stepping assays and 50 ms for SPT, to record the interaction of motors with SLBs. For obtaining motor density on SLBs, GFP labeled motors were imaged for 150 frames (256 x 256 px) with 100 ms exposure time.

FRAP imaging and analysis: Supported lipid bilayers were doped with 0.05 % Atto647n DOPE (# AD647N-16, Atto-Tec fluorescent labels and dyes) fluorescent lipid marker to visualize the homogeneity SLBs prepared on glass substrate. FRAP experiments were performed on a Nikon Eclipse Ti microscope equipped with Perfect Focus System (PFS) and a FRAP module, using which an area of defined geometry and size could be bleached. 100x/1.49 NA PlanApo TIRF oil immersion objective lens was used for imaging. A 512 x 512 pixel image was

captured at 0.1 s interval using 647-nm laser line at 10mW. 10 frames were acquired before bleaching, following which a 150 x 150 pixel region in the center of the field of view was bleached using a 647-nm laser at full power for 4.2 s (5 scan iterations). Time-lapse images were then recorded at an interval of 0.5 s for 200-250 frames to monitor the recovered fluorescence in the bleached area.

Images were then analyzed to get the diffusion coefficient of the lipids in a SLB using an algorithm described in the publication (Goehring et al., 2010). The MATLAB script was modified to correct for the fixed pattern noise arising due to non-uniform illumination and TIRF imaging. To correct for the fixed noise, all the images before bleaching were averaged to get a mean image. Mean of 1% of total pixels with lowest intensities was calculated as a normalization factor. And all the images in the stack were then corrected by multiplying by the normalization factor and dividing by the mean image so that the overall intensities of all the pixels in images are uniform.

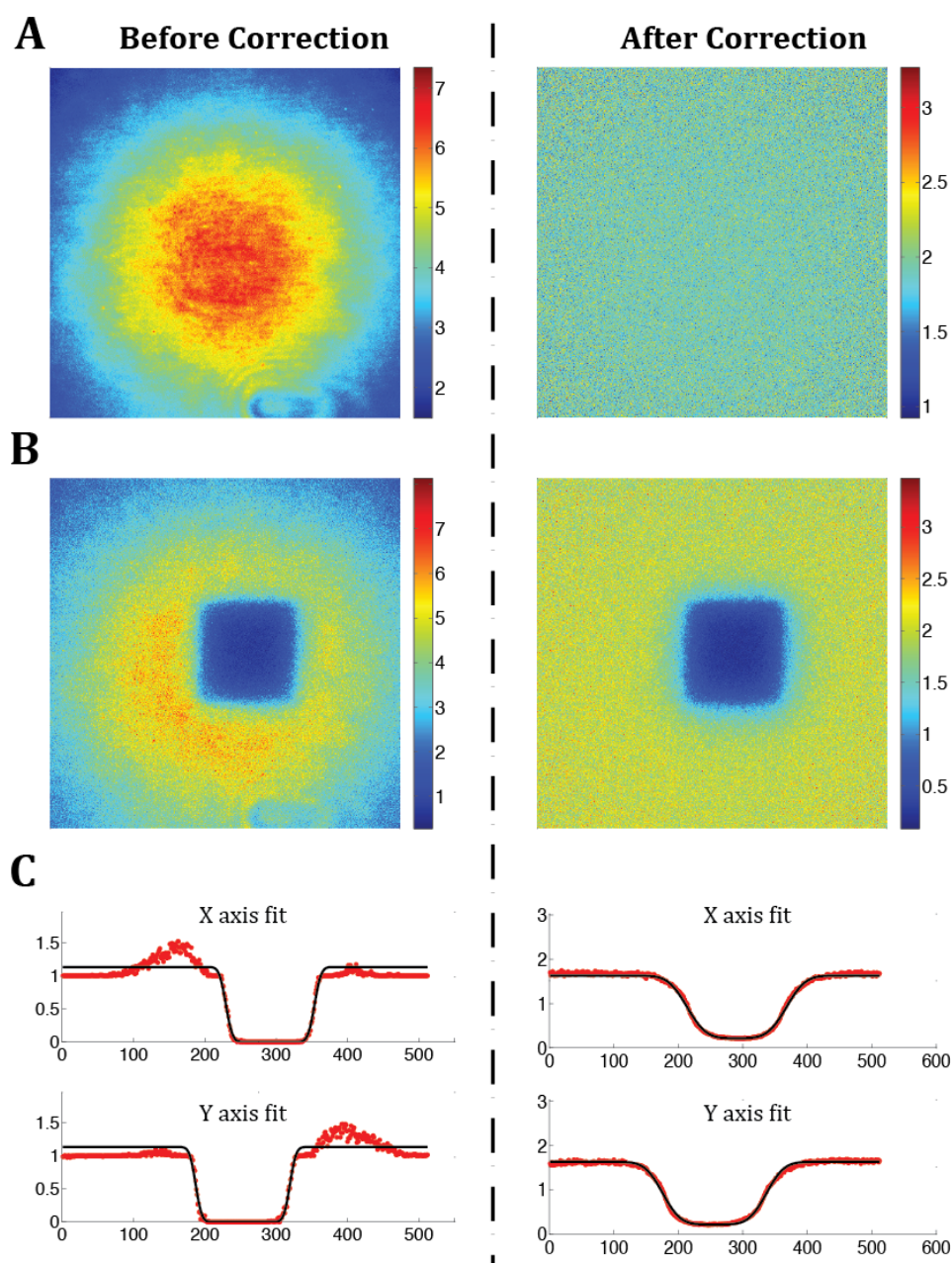


Figure 5.4 | Background noise correction for FRAP analysis. Images and fit without any correction shown in left, and after correction in right. A) Mean image of all the frames before photobleaching, B) First frame after photobleaching C) Error function fit to obtain parameters, center of bleached spot, width of bleach area, and slope of fluorescence intensity, used for fitting FRAP intensity curves.

After the background correction, images stack were loaded and the center of the bleached region and an appropriate unbleached reference were manually selected. The center of the bleached spot, m_x , m_y , d_x , d_y , were obtained by fitting the x- and y- directions individually, where m_x and m_y describe the slope of fluorescence intensity at the edges of the bleached region and, d_x and d_y describe

the extent of the bleached area. Fitting parameters were saved for selected fits, discarding the fits that were erroneous. These parameters were then used to define a 2-D error function that specified the boundaries of the bleached region to be analyzed. Mean fluorescence intensity in the bleached region is normalized with the reference fluorescence intensity and then to pre bleach intensity. The fluorescence recovery over time was then fitted with the mathematical solution described in the publication mentioned above to calculate diffusion coefficient. The mean of all individual recovery curves from different ROIs (region of interest) were then fitted again to reduce the effect of random fluctuations. Mean diffusion coefficient for lipids in a SLB was thus obtained. The error was estimated by calculating the standard error of mean of all the individual fits.

Data analysis gliding motility assays

The Fluorescence Image Evaluation Software for Tracking and Analysis (FIESTA) software package (Ruhnow et al., 2011) was used for microtubule tracking. All the connected tracks obtained from the software were visualized to exclude erroneous tracks from further analysis. Erroneous tracking could be due to for example microtubules crossing, sample drift or microtubule fragmentation. Length of microtubule was used as a control parameter for post-processing of tracks as the length is expected to remain constant over the period of experiment.

For microtubule gliding motility assays on surface-immobilized motors, the ensemble average velocity was calculated by taking mean of all the point-to-point velocities for every microtubule center position. The error was estimated by the standard deviation of point-to-point velocities.

For membrane-anchored gliding motility assays, the ensemble average velocity was obtained by calculating the mean square displacement (MSD) of the microtubule center (x, y) as a function of time. Due to the imaging of discrete frames the time t is given as multiples n of the acquisition time interval such that $t = n\Delta t$. The MSD is calculated for the non-overlapping time intervals with the following equation as explained in (Michalet, 2010)

$$MSD(n) = \frac{1}{[N/n]} \sum_{i=1}^{[N/n]-1} \underbrace{(x_{n(i+1)} - x_{ni})^2 + (y_{n(i+1)} - y_{ni})^2}_{= (r_{ni,n(i+1)})^2}, \quad n = 1, \dots, N-1 \quad (5.1)$$

where $r_{ni,n(i+1)}$ is the displacement of microtubule center over n acquisition time intervals and $[N/n]$ is the integer value of at a given n . The MSD for a microtubule center was calculated from its corresponding trajectory. Since the measured displacements for any fixed time interval $t = n\Delta t$ will be gaussian distributed (Chandrasekhar, 1943), the error of the MSD is given by:

$$\delta MSD(n) = \frac{MSD(n)}{\sqrt{[N/n]}} \quad (5.2)$$

The microtubule translocation while propelled by membrane-anchored motors can be separated into two components (i) translational component due to motor activity and (ii) diffusional component as the microtubules are pinned to a fluid lipid bilayer by motors. We quantified these two components of the microtubule translocation by fitting the MSD of a microtubule center with the following model as explained in (Qian et al., 1991)

$$MSD(n\Delta t) = (v \cdot n\Delta t)^2 + 4D \cdot n\Delta t + c \quad (5.3)$$

where v is the translational velocity of a microtubule, D is the diffusion component and c is the offset accounting for the localization uncertainty and the dynamic error due to finite camera acquisition time of 100 ms (Michalet, 2010)

Mean translational velocity and the diffusion coefficient for an individual microtubule was calculated by fitting the first 25 points of the MSD time plot with equation (3). The MSD data for the fit was weighted by the inverse of error. Only that microtubule for which the fit was good was considered for calculating the ensemble average velocity.

To calculate the mean velocity of an ensemble of microtubules at a particular motor density, we calculated cumulated MSD for all the microtubules in an image

stack. For this the displacement data $r_{ni,n(i+1)}$ of all the individual microtubule was cumulated for each discrete time and then MSD is calculated. The first 25 data points of the MSD data thus obtained was fitted with equation (3), to get an average microtubule gliding velocity. The MSD data for the fit was weighted by the inverse of error. The error for the fit was estimated by performing a bootstrapping analysis (Blainey et al., 2009). The MSD data for different microtubules was randomly picked with replacement keeping the total number of microtubule tracks analyzed same as in the initial dataset. The standard deviation of the mean velocity obtained from the bootstrap analysis, gave the standard error of the mean of the initial dataset.

Single particle tracking analysis: To obtain the diffusion coefficient of motors diffusing on a SLB similar MSD analysis as for the microtubules was performed. Single fluorescent particle, motors tagged with GFP, were localized using FIESTA software. The trajectory of a single particle was then obtained by manually connecting the center of localized particle in subsequent images in the stack based on its intensity and position. As in the case for microtubules, MSD was calculated for the non-overlapping time intervals with the equation (1)

First six points of the MSD was then fitted with the following equation (4) to get the diffusion coefficient of individual particles. The data for the fit was weighted by inverse of error.

$$MSD(n\Delta t) = 4D \cdot n\Delta t + c \quad (5.4)$$

To calculate the diffusion coefficient of ensemble of motors, we calculated cumulated MSD. For this the displacement data $r_{ni,n(i+1)}$ of all the individual motors was cumulated for each discrete time and then MSD was calculated. The MSD data as function of time thus obtained was fitted with equation (4) to get a mean D . The error for the mean D was estimated by performing a bootstrapping analysis in a same way as described earlier for the microtubules.

Data analysis for stepping motility assay: The mean velocity for individual molecules was determined by calculating the slope of trajectories in a

kymograph, space-time plot of intensity over a specified area, space dimension was chosen by a line drawn over a microtubule. The kymograph evaluation was done using FIESTA software. The mean velocity and standard deviation of the population of all the single molecules was obtained by fitting the velocity distribution with a t-location scale in MATLAB.

Motors are poisson steppers, meaning there is a certain probability for a motor to detach from microtubule after taking a step. For processive motors taking more than 50 steps before detaching from a microtubule the poisson distribution can be estimated by a gaussian distribution. The mean velocity for a single molecule is calculated by the relation

$$v_{mean} = \frac{n \times ss}{t}$$

where n is the no. of steps taken by motors before detaching, ss is step size 8 nm for kinesin motors moving on microtubules and t is the time taken for taking n steps.

The mean velocity of different individual motors walking on a microtubule would be similar, but the error associated with the mean or the width of gaussian would be inversely proportional to the square root of n, no. of steps taken. Hence it would be different for all the single molecules, as each motor would take certain number of steps on a microtubule, which might or might not be equal to other motors. Therefore, to calculate the mean velocity of population from the distribution of mean velocity of individual motors we fitted a 't-location scale' distribution in MATLAB that gave the mean and the standard deviation of the distribution as output.

The run length and the dwell time for individual molecules were determined from the individual trajectories obtained from kymographs. The mean run length and dwell time of motors were determined by evaluating the empirical cumulative distribution function (ECDF) of single motors in MATLAB and fitting them with a single exponential function. For the exponential distribution, fitting ECDF is advantageous over histograms as we avoid the fitting errors due to binning of data. The error on the fit was calculated using bootstrapping analysis

(Efron et al., 1986). The error on the fit was calculated by performing the bootstrapping analysis as described earlier.

Determination of motor density: Kinesin-1 motor density, at different bulk motor concentration, on biotinylated SLBs was determined by incubating the SLBs with unlabeled motor spiked with eGFP labeled motors in a molar ratio 1:150. The eGFP labeled motors diffusing on SLBs were then imaged with TIRF microscopy. To avoid aberrations in counting due to photobleaching, the sample was focused by imaging Atto 647n doped SLB. After focusing the perfect-focus mechanism of the Nikon TE 2000 Eclipse microscope was activated. Movie streams with 150 frames at 100 ms exposure were then recorded at five different FoVs, by exciting the sample with 488 nm lasers. Number of diffusing rKin430-SBP-GFP in the first 3 frames of the image stacks was then counted using the cell counter plug-in of image processing and analysis software Fiji. The mean, s.d. and s.e.m of the measurements were then calculated. Gliding motility assays were then performed to record the microtubule gliding velocity at that particular motor density.

Bleaching steps evaluation for FL KIF16B: Bleaching experiments were performed by incubating GFP labeled motors with surface-immobilized MTs in presence of 0.1 mM AMP-PNP, such that the motors are strongly bound to MTs . A continuous stream of images were then recorded by exciting GFP with 488 nm laser in TIRF for 500 frames with an exposure time of 100 ms. Single molecules were then tracked and analyzed for bleaching steps using the bleaching evaluation tool of FIESTA software.

References

- Akhmanova, A., & Hammer, J. a. (2010). Linking molecular motors to membrane cargo. *Current Opinion in Cell Biology*, 22(4), 479–487.
- Alberts, B., Johnson, A., Lewis, J., Raff, M., Roberts, K., & Walter, P. (2002). *Molecular Biology of the Cell*. Garland Science.
- Allen, C., Dos Santos, N., Gallagher, R., Chiu, G. N. C., Shu, Y., Li, W. M., ... Bally, M. B. (2002). Controlling the physical behavior and biological performance of liposome formulations through use of surface grafted poly(ethylene glycol). *Bioscience Reports*, 22(2), 225–250.
- Allen, R. D., Metzals, J., Tasaki, I., Brady, S. T., & Gilbert, S. P. (1982). Fast axonal transport in squid giant axon. *Science*, 218(4577), 1127–9.
- Ally, S., Larson, A. G., Barlan, K., Rice, S. E., & Gelfand, V. I. (2009). Opposite-polarity motors activate one another to trigger cargo transport in live cells. *The Journal of Cell Biology*, 187(7), 1071–82.
- Arakawa, T., Ejima, D., Tsumoto, K., Obeyama, N., Tanaka, Y., Kita, Y., & Timasheff, S. N. (2007). Suppression of protein interactions by arginine: a proposed mechanism of the arginine effects. *Biophysical Chemistry*, 127(1-2), 1–8.
- Arimura, N., Kimura, T., Nakamuta, S., Taya, S., Funahashi, Y., Hattori, A., ... Kaibuchi, K. (2009). Anterograde transport of TrkB in axons is mediated by direct interaction with Slp1 and Rab27. *Developmental Cell*, 16(5), 675–86.
- Asbury, C. L. (2005). Kinesin: World's tiniest biped. *Current Opinion in Cell Biology*, 17(1), 89–97.
- Ashkin, A., Dziedzic, J. M., Bjorkholm, J. E., & Chu, S. (1986). Observation of a single-beam gradient force optical trap for dielectric particles. *Optics Letters*, 11(5), 288.
- Barrette-Ng, I. H., Wu, S. C., Tjia, W. M., Wong, S. L., & Ng, K. K. S. (2013). The structure of the SBP-Tag-streptavidin complex reveals a novel helical scaffold bridging binding pockets on separate subunits. *Acta Crystallographica Section D: Biological Crystallography*, 69(5), 879–887.
- Berg, J. S., Derfler, B. H., Pennisi, C. M., Corey, D. P., & Cheney, R. E. (2000). Myosin-X, a novel myosin with pleckstrin homology domains, associates with regions of dynamic actin. *Journal of Cell Science*, 113 Pt 19, 3439–51.
- Bieling, P., Telley, I. A., Piehler, J., & Surrey, T. (2008). Processive kinesins require loose mechanical coupling for efficient collective motility. *EMBO Reports*, 9(11),

1121–7.

Blainey, P. C., Luo, G., Kou, S. C., Mangel, W. F., Verdine, G. L., Bagchi, B., & Xie, X. S. (2009). Nonspecifically bound proteins spin while diffusing along DNA. *Nature Structural & Molecular Biology*, *16*(12), 1224–9.

Blatner, N. R., Wilson, M. I., Lei, C., Hong, W., Murray, D., Williams, R. L., & Cho, W. (2007). The structural basis of novel endosome anchoring activity of KIF16B kinesin. *The EMBO Journal*, *26*(15), 3709–19.

Block, S. M., Goldstein, L. S., & Schnapp, B. J. (1990). Bead movement by single kinesin molecules studied with optical tweezers. *Nature*, *348*(6299), 348–52.

Böhm, K. J., Stracke, R., & Unger, E. (2000). Speeding up kinesin-driven microtubule gliding in vitro by variation of cofactor composition and physicochemical parameters. *Cell Biology International*, *24*(6), 335–41.

Brady, S. T. (1985). A novel brain ATPase with properties expected for the fast axonal transport motor. *Nature*, *317*(6032), 73–75.

Braun, M., Lansky, Z., Fink, G., Ruhnnow, F., Diez, S., & Janson, M. E. (2011). Adaptive braking by Ase1 prevents overlapping microtubules from sliding completely apart. *Nature Cell Biology*, *13*(10), 1259–64.

Braunger, J. A., Kramer, C., Morick, D., & Steinem, C. (2013). Solid supported membranes doped with PIP2: influence of ionic strength and pH on bilayer formation and membrane organization. *Langmuir: The ACS Journal of Surfaces and Colloids*, *29*(46), 14204–13.

Brouhard, G. J. (2015). Dynamic instability 30 years later: complexities in microtubule growth and catastrophe. *Molecular Biology of the Cell*, *26*(7), 1207–1210.

Capitanio, M., & Pavone, F. S. (2013). Interrogating biology with force: Single molecule high-resolution measurements with optical tweezers. *Biophysical Journal*, *105*(6), 1293–1303.

Caplow, M., & Shanks, J. (1996). Evidence that a single monolayer tubulin-GTP cap is both necessary and sufficient to stabilize microtubules. *Molecular Biology of the Cell*, *7*(4), 663–75.

Carter, A., Cho, C., Jin, L., & Vale, R. D. (2011). Crystal structure of the dynein motor domain. *Science*, *331*(6021), 1159–65.

Carter, N. J., & Cross, R. (2005). Mechanics of the kinesin step. *Nature*, *435*(7040), 308–12.

Chan, Y.-H. M., & Boxer, S. G. (2007). Model membrane systems and their applications. *Current Opinion in Chemical Biology*, *11*(6), 581–7.

- Chandaroy, P., Sen, A., Alexandridis, P., & Hui, S. W. (2002). Utilizing temperature-sensitive association of Pluronic F-127 with lipid bilayers to control liposome-cell adhesion. *Biochimica et Biophysica Acta (BBA) - Biomembranes*, 1559(1), 32–42.
- Chandrasekhar, S. (1943). Stochastic Problems in Physics and Astronomy. *Reviews of Modern Physics*, 15(1), 1–89.
- Cheney, R. E., O’Shea, M. K., Heuser, J. E., Coelho, M. V, Wolenski, J. S., Espreafico, E. M., ... Mooseker, M. S. (1993). Brain myosin-V is a two-headed unconventional myosin with motor activity. *Cell*, 75(1), 13–23.
- Chiantia, S., Ries, J., Kahya, N., & Schwille, P. (2006). Combined AFM and two-focus SFCS study of raft-exhibiting model membranes. *ChemPhysChem*, 7(11), 2409–2418.
- Chrétien, D., Fuller, S. D., & Karsenti, E. (1995). Structure of growing microtubule ends: two-dimensional sheets close into tubes at variable rates. *The Journal of Cell Biology*, 129(5), 1311–28.
- Clemmens, J., Hess, H., Lipscomb, R., Hanein, Y., Böhringer, K. F., Matzke, C. M., ... Vogel, V. (2003). Mechanisms of Microtubule Guiding on Microfabricated Kinesin-Coated Surfaces: Chemical and Topographic Surface Patterns. *Langmuir*, 19(26), 10967–10974.
- Conway, L., Wood, D., Tüzel, E., & Ross, J. L. (2012). Motor transport of self-assembled cargos in crowded environments. *Proceedings of the National Academy of Sciences*, 109(51), 20814–9.
- Coy, D. L., Hancock, W. O., Wagenbach, M., & Howard, J. (1999). Kinesin’s tail domain is an inhibitory regulator of the motor domain. *Nature Cell Biology*, 1(5), 288–292.
- Crevel, I., Lockhart, A., & Cross, R. (1996). Weak and strong states of kinesin and ncd. *Journal of Molecular Biology*, 257(1), 66–76.
- Crevenna, A. H., Madathil, S., Cohen, D. N., Wagenbach, M., Fahmy, K., & Howard, J. (2008). Secondary structure and compliance of a predicted flexible domain in kinesin-1 necessary for cooperation of motors. *Biophysical Journal*, 95(11), 5216–27.
- Derr, N. D., Goodman, B. S., Jungmann, R., Leschziner, a. E., Shih, W. M., & Reck-Peterson, S. L. (2012). Tug-of-War in Motor Protein Ensembles Revealed with a Programmable DNA Origami Scaffold. *Science*, 338(6107), 662–665.
- Desai, A., & Mitchison, T. J. (1997). Microtubule polymerization dynamics. *Annual Review of Cell and Developmental Biology*, 13, 83–117.

- Dorner, C., Ullrich, A., Haring, H.-U., & Lammers, R. (1999). The Kinesin-like Motor Protein KIF1C Occurs in Intact Cells as a Dimer and Associates with Proteins of the 14-3-3 Family. *Journal of Biological Chemistry*, 274(47), 33654–33660.
- Drechsel, D. N., & Kirschner, M. W. (1994). The minimum GTP cap required to stabilize microtubules. *Current Biology : CB*, 4(12), 1053–61.
- Duke, T., Holy, T. E., & Leibler, S. (1995). “Gliding assays” for motor proteins: A theoretical analysis. *Physical Review Letters*, 74(2), 330–333.
- Durocher, D., & Jackson, S. P. (2002). The FHA domain. *FEBS Letters*, 513(1), 58–66.
- Efron, B., & Tibshirani, R. (1986). [Bootstrap Methods for Standard Errors, Confidence Intervals, and Other Measures of Statistical Accuracy]: Rejoinder. *Statistical Science*, 1(1), 77–77.
- Endow, S. A., Kull, F. J., & Liu, H. (2010). Kinesins at a glance. *Journal of Cell Science*, 123(Pt 20), 3420–3424.
- Erickson, H. P. (2009). Size and shape of protein molecules at the nanometer level determined by sedimentation, gel filtration, and electron microscopy. *Biological Procedures Online*, 11, 32–51.
- Farkhondeh, a., Niwa, S., Takei, Y., & Hirokawa, N. (2015). Characterizing KIF16B in Neurons Reveals a Novel Intramolecular “Stalk Inhibition” Mechanism That Regulates Its Capacity to Potentiate the Selective Somatodendritic Localization of Early Endosomes. *Journal of Neuroscience*, 35(12), 5067–5086.
- Feitosa, E., & Winnik, F. M. (2010). Interaction between Pluronic F127 and dioctadecyldimethylammonium bromide (DODAB) vesicles studied by differential scanning Calorimetry. *Langmuir*, 26(23), 17852–17857.
- Fischer, J. (2010). *Investigation of Microtubule Motility Driven by Membrane-Anchored Motor Proteins*. Technische Universität Dresden.
- Fu, M. M., & Holzbaur, E. L. F. (2014). Integrated regulation of motor-driven organelle transport by scaffolding proteins. *Trends in Cell Biology*, 1–11.
- Furuta, K., Furuta, A., Toyoshima, Y. Y., Amino, M., Oiwa, K., & Kojima, H. (2013). Measuring collective transport by defined numbers of processive and nonprocessive kinesin motors. *Proceedings of the National Academy of Sciences*, 110(2), 501–6.
- Gagliano, J., Walb, M., Blaker, B., Macosko, J. C., & Holzwarth, G. (2010). Kinesin velocity increases with the number of motors pulling against viscoelastic drag. *European Biophysics Journal : EBJ*, 39(5), 801–13.

Gell, C., Bormuth, V., Brouhard, G. J., Cohen, D. N., Diez, S., Friel, C. T., ... Howard, J. (2010). Microtubule dynamics reconstituted in vitro and imaged by single-molecule fluorescence microscopy. *Methods in Cell Biology*, *95*(C), 221–245.

Gell, C., Friel, C. T., Borgonovo, B., Drechsel, D. N., Hyman, A. A., & Howard, J. (2011). Purification of tubulin from porcine brain. *Methods in Molecular Biology (Clifton, N.J.)*, *777*, 15–28.

Gelles, J., Schnapp, B. J., & SHEETZ, M. (1988). Tracking kinesin-driven movements with nanometre-scale precision. *Nature*, *331*(6155), 450–3.

Gho, M., McDonald, K., Ganetzky, B., & Saxton, W. M. (1992). Effects of kinesin mutations on neuronal functions. *Science*, *258*(5080), 313–6.

Gittes, F., Meyhöfer, E., Baek, S., & Howard, J. (1996). Directional loading of the kinesin motor molecule as it buckles a microtubule. *Biophysical Journal*, *70*(1), 418–429.

Glater, E. E., Megeath, L. J., Stowers, R. S., & Schwarz, T. L. (2006). Axonal transport of mitochondria requires mlt1 to recruit kinesin heavy chain and is light chain independent. *The Journal of Cell Biology*, *173*(4), 545–57.

Goehring, N. W., Chowdhury, D., Hyman, A. a., & Grill, S. W. (2010). FRAP analysis of membrane-associated proteins: Lateral diffusion and membrane-cytoplasmic exchange. *Biophysical Journal*, *99*(8), 2443–2452.

Granger, E., McNee, G., Allan, V., & Woodman, P. (2014). The role of the cytoskeleton and molecular motors in endosomal dynamics. *Seminars in Cell & Developmental Biology*, *31*, 20–9.

Gunawardena, S., & Goldstein, L. S. (2004). Cargo-carrying motor vehicles on the neuronal highway: transport pathways and neurodegenerative disease. *Journal of Neurobiology*, *58*(2), 258–71.

Gundelfinger, E. D., Kessels, M. M., & Qualmann, B. (2003). Temporal and spatial coordination of exocytosis and endocytosis. *Nature Reviews. Molecular Cell Biology*, *4*(2), 127–39.

Hackney, D. D., Baek, N., & Snyder, A. C. (2009). Half-site inhibition of dimeric kinesin head domains by monomeric tail domains. *Biochemistry*, *48*(15), 3448–56.

Hall, D. H., & Hedgecock, E. M. (1991). Kinesin-related gene unc-104 is required for axonal transport of synaptic vesicles in *C. elegans*. *Cell*, *65*(5), 837–47.

Hammond, J. W., Cai, D., Blasius, T. L., Li, Z., Jiang, Y., Jih, G. T., ... Verhey, K. J. (2009). Mammalian Kinesin-3 motors are dimeric in vivo and move by processive motility upon release of autoinhibition. *PLoS Biology*, *7*(3), e72.

- Hancock, W. O., & Howard, J. (1998). Processivity of the Motor Protein Kinesin Requires Two Heads. *The Journal of Cell Biology*, *140*(6), 1395–1405.
- Hancock, W. O., & Howard, J. (1999). Kinesin's processivity results from mechanical and chemical coordination between the ATP hydrolysis cycles of the two motor domains. *Proceedings of the National Academy of Sciences*, *96*(23), 13147–13152.
- Hartman, M. A., & Spudich, J. A. (2012). The myosin superfamily at a glance. *Journal of Cell Science*, *125*(Pt 7), 1627–32.
- Haucke, V., Neher, E., & Sigrist, S. J. (2011). Protein scaffolds in the coupling of synaptic exocytosis and endocytosis. *Nature Reviews. Neuroscience*, *12*(3), 127–138.
- Hawkins, T. L., Sept, D., Mogessie, B., Straube, A., & Ross, J. L. (2013). Mechanical properties of doubly stabilized microtubule filaments. *Biophysical Journal*, *104*(7), 1517–1528.
- Hendricks, a. G., Holzbaur, E. L. F., & Goldman, Y. E. (2012). Force measurements on cargoes in living cells reveal collective dynamics of microtubule motors. *Proceedings of the National Academy of Sciences*, *2012*(12), 1–6.
- Herold, C., Leduc, C., Stock, R., Diez, S., & Schwille, P. (2012). Long-range transport of giant vesicles along microtubule networks. *ChemPhysChem*, *13*(4), 1001–1006.
- Hill, D. B., Plaza, M. J., Bonin, K., & Holzwarth, G. (2004). Fast vesicle transport in PC12 neurites: velocities and forces. *European Biophysics Journal: EBJ*, *33*(7), 623–32.
- Hirokawa, N. (1998). Kinesin and Dynein Superfamily Proteins and the Mechanism of Organelle Transport. *Science*, *279*(5350), 519–526.
- Hirokawa, N., Niwa, S., & Tanaka, Y. (2010). Molecular motors in neurons: Transport mechanisms and roles in brain function, development, and disease. *Neuron*, *68*(4), 610–638.
- Hirokawa, N., Noda, Y., Tanaka, Y., & Niwa, S. (2009). Kinesin superfamily motor proteins and intracellular transport. *Nature Reviews. Molecular Cell Biology*, *10*(10), 682–696.
- Hirokawa, N., & Tanaka, Y. (2015). Kinesin superfamily proteins (KIFs): Various functions and their relevance for important phenomena in life and diseases. *Experimental Cell Research*, *334*(1), 16–25.
- Hoepfner, S., Severin, F., Cabezas, A., Habermann, B., Runge, A., Gillooly, D., ... Zerial, M. (2005). Modulation of receptor recycling and degradation by the endosomal kinesin KIF16B. *Cell*, *121*(3), 437–50.

- Hokanson, D. E., Laakso, J. M., Lin, T., Sept, D., & Ostap, E. M. (2006). Myo1c binds phosphoinositides through a putative pleckstrin homology domain. *Molecular Biology of the Cell*, 17(11), 4856–65.
- Holthuis, J. C. M., Meer, G. van, & Huitema, K. (2009). Lipid microdomains, lipid translocation and the organization of intracellular membrane transport (Review).
- Howard, J. (2001). *Mechanics of Motor Proteins and the Cytoskeleton*. Sinauer Associates, Inc.; Sunderland Massachusetts. Sinauer Associates, Inc.; Sunderland Massachusetts.
- Howard, J., Hudspeth, A. J., & Vale, R. D. (1989). Movement of microtubules by single kinesin molecules. *Nature*, 342(6246), 154–158.
- Hua, W., Young, E. C., Fleming, M. L., & Gelles, J. (1997). Coupling of kinesin steps to ATP hydrolysis, 388(6640), 390–393.
- Huckaba, T. M., Gennerich, A., Wilhelm, J. E., Chishti, A. H., & Vale, R. D. (2011). Kinesin-73 is a processive motor that localizes to Rab5-containing organelles. *The Journal of Biological Chemistry*, 286(9), 7457–67.
- Hunt, A. J., Gittes, F., & Howard, J. (1994). The force exerted by a single kinesin molecule against a viscous load. *Biophysical Journal*, 67(2), 766–781.
- Huo, L., Yue, Y., Ren, J., Yu, J., Liu, J., Yu, Y., ... Feng, W. (2012). The CC1-FHA tandem as a central hub for controlling the dimerization and activation of kinesin-3 KIF1A. *Structure (London, England : 1993)*, 20(9), 1550–61.
- Hurd, D. D., & Saxton, W. M. (1996). Kinesin mutations cause motor neuron disease phenotypes by disrupting fast axonal transport in *Drosophila*. *Genetics*, 144(3), 1075–85.
- Johnson, K. A., & Gilbert, S. P. (1995). Pathway of the microtubule-kinesin ATPase. *Biophysical Journal*, 68(4 Suppl), 173S–176S; discussion 176S–179S.
- Kaan, H. Y. K., Hackney, D. D., & Kozielski, F. (2011). The structure of the kinesin-1 motor-tail complex reveals the mechanism of autoinhibition. *Science*, 333(6044), 883–5.
- Kamal, A., Stokin, G. B., Yang, Z., Xia, C. H., & Goldstein, L. S. (2000). Axonal transport of amyloid precursor protein is mediated by direct binding to the kinesin light chain subunit of kinesin-I. *Neuron*, 28(2), 449–59.
- Kapust, R. B., & Waugh, D. S. (1999). *Escherichia coli* maltose-binding protein is uncommonly effective at promoting the solubility of polypeptides to which it is fused. *Protein Science : A Publication of the Protein Society*, 8(8), 1668–74.

- Kawaguchi, K. (2008). Energetics of kinesin-1 stepping mechanism. *FEBS Letters*, *582*(27), 3719–22.
- Kerssemakers, J., Howard, J., Hess, H., & Diez, S. (2006). The distance that kinesin-1 holds its cargo from the microtubule surface measured by fluorescence interference contrast microscopy. *Proceedings of the National Academy of Sciences*, *103*(43), 15812–15817.
- Kerssemakers, J., Ionov, L., Queitsch, U., Luna, S., Hess, H., & Diez, S. (2009). 3D nanometer tracking of motile microtubules on reflective surfaces. *Small*, *5*(15), 1732–1737.
- Kikkawa, M. (2008). The role of microtubules in processive kinesin movement. *Trends in Cell Biology*, *18*(3), 128–35.
- Klopfenstein, D. R., Tomishige, M., Stuurman, N., & Vale, R. D. (2002). Role of phosphatidylinositol(4,5)bisphosphate organization in membrane transport by the Unc104 kinesin motor. *Cell*, *109*(3), 347–58.
- Knight, J. D., Lerner, M. G., Marcano-Velázquez, J. G., Pastor, R. W., & Falke, J. J. (2010). Single molecule diffusion of membrane-bound proteins: window into lipid contacts and bilayer dynamics. *Biophysical Journal*, *99*(9), 2879–87.
- Kobayashi, T., Morone, N., Kashiyama, T., Oyamada, H., Kurebayashi, N., & Murayama, T. (2008). Engineering a novel multifunctional green fluorescent protein tag for a wide variety of protein research. *PloS One*, *3*(12), e3822.
- Kulic, I. M., Brown, A. E. X., Kim, H., Kural, C., Blehm, B., Selvin, P. R., ... Gelfand, V. I. (2008). The role of microtubule movement in bidirectional organelle transport. *Proceedings of the National Academy of Sciences*, *105*(29), 10011–10016.
- Kull, F. J., Sablin, E. P., Lau, R., Fletterick, R. J., & Vale, R. D. (1996). Crystal structure of the kinesin motor domain reveals a structural similarity to myosin. *Nature*, *380*(6574), 550–5.
- Kural, C., Kim, H., Syed, S., Goshima, G., Gelfand, V. I., & Selvin, P. R. (2005). Kinesin and dynein move a peroxisome in vivo: a tug-of-war or coordinated movement? *Science*, *308*(5727), 1469–72.
- Kuzuya, A., Numajiri, K., Kimura, M., & Komiyama, M. (2008). Single-molecule accommodation of streptavidin in nanometer-scale wells formed in DNA nanostructures. *Nucleic Acids Symposium Series (2004)*, (52), 681–2.
- Lansky, Z., Braun, M., Lüdecke, A., Schlierf, M., ten Wolde, P. R., Janson, M. E., & Diez, S. (2015). Diffusible Crosslinkers Generate Directed Forces in Microtubule Networks. *Cell*, *160*(6), 1159–68.
- Leduc, C., Campàs, O., Zeldovich, K. B., Roux, A., Jolimaitre, P., Bourel-Bonnet, L., ... Prost, J. (2004). Cooperative extraction of membrane nanotubes by molecular

motors. *Proceedings of the National Academy of Sciences*, 101(49), 17096–101.

Leduc, C., Ruhnnow, F., Howard, J., & Diez, S. (2007). Detection of fractional steps in cargo movement by the collective operation of kinesin-1 motors. *Proceedings of the National Academy of Sciences*, 104(26), 10847–10852.

Lee, J.-R., Shin, H.-W., Choi, J., Ko, J., Kim, S., Lee, H. W., ... Kim, E. (2004). An intramolecular interaction between the FHA domain and a coiled coil negatively regulates the kinesin motor KIF1A. *The EMBO Journal*, 23(7), 1506–15.

Levi, V., Serpinskaya, A. S., Gratton, E., & Gelfand, V. I. (2006). Organelle transport along microtubules in *Xenopus melanophores*: evidence for cooperation between multiple motors. *Biophysical Journal*, 90(1), 318–27.

Liang, X., Mao, G., & Ng, K. Y. S. (2005). Effect of chain lengths of PEO-PPO-PEO on small unilamellar liposome morphology and stability: an AFM investigation. *Journal of Colloid and Interface Science*, 285(1), 360–72.

Lodish, H., Berk, A., Zipursky, S. L., Matsudaira, P., Baltimore, D., & Darnell, J. (2000). *Molecular Cell Biology*. W. H. Freeman.

Lupas, A., Van Dyke, M., & Stock, J. (1991). Predicting coiled coils from protein sequences. *Science*, 252(5009), 1162–4.

Macaskill, A. F., Rinholm, J. E., Twelvetrees, A. E., Arancibia-Carcamo, I. L., Muir, J., Fransson, A., ... Kittler, J. T. (2009). Miro1 is a calcium sensor for glutamate receptor-dependent localization of mitochondria at synapses. *Neuron*, 61(4), 541–55.

Machan, R., & Hof, M. (2010). Lipid diffusion in planar membranes investigated by fluorescence correlation spectroscopy. *Biochimica et Biophysica Acta*, 1798(7), 1377–91.

Mallik, R., Rai, A. K., Barak, P., Rai, A., & Kunwar, a. (2013). Teamwork in microtubule motors. *Trends in Cell Biology*, 23(11), 575–582.

McKenney, R. J., Huynh, W., Tanenbaum, M. E., Bhabha, G., & Vale, R. D. (2014). Activation of cytoplasmic dynein motility by dynactin-cargo adapter complexes. *Science*, 345(6194), 337–341.

McLaughlin, S., & Murray, D. (2005). Plasma membrane phosphoinositide organization by protein electrostatics. *Nature*, 438(7068), 605–11.

Michalet, X. (2010). Mean square displacement analysis of single-particle trajectories with localization error: Brownian motion in an isotropic medium. *Physical Review E*, 82(4 Pt 1), 041914.

Miki, H., Okada, Y., & Hirokawa, N. (2005). Analysis of the kinesin superfamily: insights into structure and function. *Trends in Cell Biology*, 15(9), 467–76.

- Miki, H., Setou, M., Kaneshiro, K., & Hirokawa, N. (2001). All kinesin superfamily protein, KIF, genes in mouse and human. *Proceedings of the National Academy of Sciences*, *98*(13), 7004–7011.
- Milic, B., Andreasson, J. O. L., Hancock, W. O., & Block, S. M. (2014). Kinesin processivity is gated by phosphate release. *Proceedings of the National Academy of Sciences*.
- Moyer, M. L., Gilbert, S. P., & Johnson, K. A. (1998). Pathway of ATP hydrolysis by monomeric and dimeric kinesin. *Biochemistry*, *37*(3), 800–13.
- Nagle, J. F., & Tristram-Nagle, S. (2000). Structure of lipid bilayers. *Biochimica et Biophysica Acta*, *1469*(3), 159–95.
- Nelson, S. R., Trybus, K. M., & Warshaw, D. M. (2014). Motor coupling through lipid membranes enhances transport velocities for ensembles of myosin Va. *Proceedings of the National Academy of Sciences*, *111*(38), E3986–E3995.
- Nitta, T., & Hess, H. (2005). Dispersion in Active Transport by Kinesin-Powered Molecular Shuttles. *Nano Letters*, *5*(7), 1337–1342.
- Niwa, S., Tanaka, Y., & Hirokawa, N. (2008). KIF1Bbeta- and KIF1A-mediated axonal transport of presynaptic regulator Rab3 occurs in a GTP-dependent manner through DENN/MADD. *Nature Cell Biology*, *10*(11), 1269–79.
- Nogales, E., & Wang, H. W. (2006). Structural intermediates in microtubule assembly and disassembly: How and why? *Current Opinion in Cell Biology*, *18*(2), 179–184.
- Nye, J. A., & Groves, J. T. (2008). Kinetic control of histidine-tagged protein surface density on supported lipid bilayers. *Langmuir: The ACS Journal of Surfaces and Colloids*, *24*(8), 4145–9.
- Okada, Y., Higuchi, H., & Hirokawa, N. (2003). Processivity of the single-headed kinesin KIF1A through biased binding to tubulin. *Nature*, *424*(6948), 574–7.
- Okada, Y., & Hirokawa, N. (2000). Mechanism of the single-headed processivity: diffusional anchoring between the K-loop of kinesin and the C terminus of tubulin. *Proceedings of the National Academy of Sciences*, *97*(2), 640–5.
- Okada, Y., Yamazaki, H., Sekine-Aizawa, Y., & Hirokawa, N. (1995). The neuron-specific kinesin superfamily protein KIF1A is a unique monomeric motor for anterograde axonal transport of synaptic vesicle precursors. *Cell*, *81*(5), 769–780.
- Paschal, B. M., Shpetner, H. S., & Vallee, R. B. (1987). MAP 1C is a microtubule-activated ATPase which translocates microtubules in vitro and has dynein-like

properties. *The Journal of Cell Biology*, 105(3), 1273–82.

Perez Bay, A. E., Schreiner, R., Mazzoni, F., Carvajal-Gonzalez, J. M., Gravotta, D., Perret, E., ... Rodriguez-Boulan, E. J. (2013). The kinesin KIF16B mediates apical transcytosis of transferrin receptor in AP-1B-deficient epithelia. *The EMBO Journal*, 32(15), 2125–39.

Pyrpassopoulos, S., Feeser, E. a., Mazerik, J. N., Tyska, M. J., & Ostap, E. M. (2012). Membrane-bound Myo1c powers asymmetric motility of actin filaments. *Current Biology*, 22(18), 1688–1692.

Qian, H., SHEETZ, M., & Elson, E. L. (1991). Single particle Tracking. *Biophysical Journal*, 60(4), 910–921.

Redfern, D. A., & Gericke, A. (2004). Domain formation in phosphatidylinositol monophosphate/phosphatidylcholine mixed vesicles. *Biophysical Journal*, 86(5), 2980–92.

Richter, R. P., Bérat, R., & Brisson, A. R. (2006). Formation of solid-supported lipid bilayers: an integrated view. *Langmuir: The ACS Journal of Surfaces and Colloids*, 22(8), 3497–505.

Ries, J., Chiantia, S., & Schwille, P. (2009). Accurate determination of membrane dynamics with line-scan FCS. *Biophysical Journal*, 96(5), 1999–2008.

Roberts, A. J., Kon, T., Knight, P. J., Sutoh, K., & Burgess, S. A. (2013). Functions and mechanics of dynein motor proteins. *Nature Reviews. Molecular Cell Biology*, 14(11), 713–26.

Rocha, N., Kuijl, C., van der Kant, R., Janssen, L., Houben, D., Janssen, H., ... Neefjes, J. (2009). Cholesterol sensor ORP1L contacts the ER protein VAP to control Rab7-RILP-p150 Glued and late endosome positioning. *The Journal of Cell Biology*, 185(7), 1209–25.

Rogers, A. R., Driver, J. W., Constantinou, P. E., Kenneth Jamison, D., & Diehl, M. R. (2009). Negative interference dominates collective transport of kinesin motors in the absence of load. *Physical Chemistry Chemical Physics: PCCP*, 11(24), 4882–9.

Rogers, K. R., Weiss, S., Crevel, I., Brophy, P. J., Geeves, M., & Cross, R. (2001). KIF1D is a fast non-processive kinesin that demonstrates novel K-loop-dependent mechanochemistry. *The EMBO Journal*, 20(18), 5101–13.

Rosenfeld, S. S., Renner, B., Correia, J. J., Mayo, M. S., & Cheung, H. C. (1996). Equilibrium studies of kinesin-nucleotide intermediates. *The Journal of Biological Chemistry*, 271(16), 9473–82.

- Ruhnow, F., Zwicker, D., & Diez, S. (2011). Tracking single particles and elongated filaments with nanometer precision. *Biophysical Journal*, *100*(11), 2820–8.
- Sack, S., Müller, J., Marx, A., Thormählen, M., Mandelkow, E. M., Brady, S. T., & Mandelkow, E. (1997). X-ray structure of motor and neck domains from rat brain kinesin. *Biochemistry*, *36*(51), 16155–65.
- Saffman, P. G., & Delbruck, M. (1975). Brownian motion in biological membranes. *Proceedings of the National Academy of Sciences*, *72*(8), 3111–3113.
- Schiff, P. B., Fant, J., & Horwitz, S. B. (1979). Promotion of microtubule assembly in vitro by taxol. *Nature*.
- Schlager, M. A., Kapitein, L. C., Grigoriev, I., Burzynski, G. M., Wulf, P. S., Keijzer, N., ... Hoogenraad, C. C. (2010). Pericentrosomal targeting of Rab6 secretory vesicles by Bicaudal-D-related protein 1 (BICDR-1) regulates neuritogenesis. *The EMBO Journal*, *29*(10), 1637–51.
- Schmidt, M. R., Maritzen, T., Kukhtina, V., Higman, V. A., Doglio, L., Barak, N. N., ... Haucke, V. (2009). Regulation of endosomal membrane traffic by a Gadkin/AP-1/kinesin KIF5 complex. *Proceedings of the National Academy of Sciences*, *106*(36), 15344–9.
- Schneider, R., Korten, T., Walter, W. J., & Diez, S. (2015). Kinesin-1 motors can circumvent permanent roadblocks by side-shifting to neighboring protofilaments. *Biophysical Journal*, *108*(9), 2249–57.
- Schnitzer, M. J., & Block, S. M. (1997). Kinesin hydrolyses one ATP per 8-nm step. *Nature*, *388*(6640), 386–90.
- Setou, M., Seog, D.-H., Tanaka, Y., Kanai, Y., Takei, Y., Kawagishi, M., & Hirokawa, N. (2002). Glutamate-receptor-interacting protein GRIP1 directly steers kinesin to dendrites. *Nature*, *417*(6884), 83–7.
- Sharp, D. J., Rogers, G. C., & Scholey, J. M. (2000a). Microtubule motors in mitosis. *Nature*, *407*(6800), 41–47.
- Sharp, D. J., Rogers, G. C., & Scholey, J. M. (2000b). Roles of motor proteins in building microtubule-based structures: a basic principle of cellular design. *Biochimica et Biophysica Acta*, *1496*(1), 128–41.
- Shtridelman, Y., Cahyuti, T., Townsend, B., DeWitt, D., & Macosko, J. C. (2008). Force-velocity curves of motor proteins cooperating in vivo. *Cell Biochemistry and Biophysics*, *52*(1), 19–29.
- Shubeita, G. T., Tran, S. L., Xu, J., Vershinin, M., Cermelli, S., Cotton, S. L., ... Gross, S. P. (2008). Consequences of motor copy number on the intracellular transport of kinesin-1-driven lipid droplets. *Cell*, *135*(6), 1098–107.

- Skjeldal, F. M., Strunze, S., Bergeland, T., Walseng, E., Gregers, T. F., & Bakke, O. (2012). The fusion of early endosomes induces molecular-motor-driven tubule formation and fission. *Journal of Cell Science*, *125*(Pt 8), 1910–9.
- Soppina, V., Norris, S. R., Dizaji, a. S., Kortus, M., Veatch, S., Peckham, M., & Verhey, K. J. (2014). Dimerization of mammalian kinesin-3 motors results in superprocessive motion. *Proceedings of the National Academy of Sciences*, 1–6.
- Soppina, V., Rai, A. K., Ramaiya, A. J., Barak, P., & Mallik, R. (2009). Tug-of-war between dissimilar teams of microtubule motors regulates transport and fission of endosomes. *Proceedings of the National Academy of Sciences*, *106*(46), 19381–6.
- Spudich, J. A., Kron, S. J., & SHEETZ, M. (1985). Movement of myosin-coated beads on oriented filaments reconstituted from purified actin. *Nature*, *315*(6020), 584–586.
- Stahelin, R. V, Scott, J. L., & Frick, C. T. (2014). Cellular and molecular interactions of phosphoinositides and peripheral proteins. *Chemistry and Physics of Lipids*, *182*, 3–18.
- Stenmark, H. (2009). Rab GTPases as coordinators of vesicle traffic. *Nature Reviews. Molecular Cell Biology*, *10*(8), 513–25.
- Su, Q., Cai, Q., Gerwin, C., Smith, C. L., & Sheng, Z.-H. (2004). Syntabulin is a microtubule-associated protein implicated in syntaxin transport in neurons. *Nature Cell Biology*, *6*(10), 941–53.
- Su, X., Ohi, R., & Pellman, D. (2012). Move in for the kill: motile microtubule regulators. *Trends in Cell Biology*, *22*(11), 567–75.
- Sumino, Y., Nagai, K. H., Shitaka, Y., Tanaka, D., Yoshikawa, K., Chaté, H., & Oiwa, K. (2012). Large-scale vortex lattice emerging from collectively moving microtubules. *Nature*, *483*(7390), 448–52.
- Sun, F., Zhu, C., Dixit, R., & Cavalli, V. (2011). Sunday Driver/JIP3 binds kinesin heavy chain directly and enhances its motility. *The EMBO Journal*, *30*(16), 3416–3429.
- Sun, P., Tropea, J. E., & Waugh, D. S. (2011). Enhancing the solubility of recombinant proteins in Escherichia coli by using hexahistidine-tagged maltose-binding protein as a fusion partner. *Methods in Molecular Biology (Clifton, N.J.)*, *705*, 259–74.
- Svoboda, K., Schmidt, C. F., Schnapp, B. J., & Block, S. M. (1993). Direct observation of kinesin stepping by optical trapping interferometry. *Nature*, *365*(6448), 721–7.
- Szodorai, A., Kuan, Y.-H., Hunzelmann, S., Engel, U., Sakane, A., Sasaki, T., ... Kins,

S. (2009). APP anterograde transport requires Rab3A GTPase activity for assembly of the transport vesicle. *The Journal of Neuroscience: The Official Journal of the Society for Neuroscience*, 29(46), 14534–44.

Tomishige, M., Klopfenstein, D. R., & Vale, R. D. (2002). Conversion of Unc104/KIF1A kinesin into a processive motor after dimerization. *Science*, 297(5590), 2263–2267.

Twelvetrees, A. E., Yuen, E. Y., Arancibia-Carcamo, I. L., MacAskill, A. F., Rostaing, P., Lumb, M. J., ... Kittler, J. T. (2010). Delivery of GABAARs to synapses is mediated by HAP1-KIF5 and disrupted by mutant huntingtin. *Neuron*, 65(1), 53–65.

Ueno, H., Huang, X., Tanaka, Y., & Hirokawa, N. (2011). KIF16B/Rab14 molecular motor complex is critical for early embryonic development by transporting FGF receptor. *Developmental Cell*, 20(1), 60–71.

Vale, R. D. (2003). The molecular motor toolbox for intracellular transport. *Cell*, 112(4), 467–80.

Vale, R. D., & Fletterick, R. J. (2003). THE DESIGN PLAN OF KINESIN MOTORS.

Vale, R. D., REESE, T., & SHEETZ, M. (1985). Identification of a novel force-generating protein, kinesin, involved in microtubule-based motility. *Cell*, 42(1), 39–50.

Van den Heuvel, M. G. L., Bolhuis, S., & Dekker, C. (2007). Persistence length measurements from stochastic single-microtubule trajectories. *Nano Letters*, 7(10), 3138–3144.

van Mameren, J., Vermeulen, K. C., Gittes, F., & Schmidt, C. F. (2009). Leveraging single protein polymers to measure flexural rigidity. *The Journal of Physical Chemistry. B*, 113(12), 3837–44.

Venkateswarlu, K., Hanada, T., & Chishti, A. H. (2005). Centaurin-alpha1 interacts directly with kinesin motor protein KIF13B. *Journal of Cell Science*, 118(Pt 11), 2471–84.

Verhey, K. J., Meyer, D., Deehan, R., Blenis, J., Schnapp, B. J., Rapoport, T. A., & Margolis, B. (2001). Cargo of kinesin identified as JIP scaffolding proteins and associated signaling molecules. *The Journal of Cell Biology*, 152(5), 959–70.

Visscher, K., Schnitzer, M. J., & Block, S. M. (1999). Single kinesin molecules studied with a molecular force clamp. *Nature*, 400(6740), 184–9.

Wade, R. H., Chrétien, D., & Job, D. (1990). Characterization of microtubule protofilament numbers. How does the surface lattice accommodate? *Journal of Molecular Biology*, 212(4), 775–86.

Walczak, C. E., Gayek, S., & Ohi, R. (2013). Microtubule-Depolymerizing Kinesins. *Annual Review of Cell and Developmental Biology*, 29(1), 417–441.

Walker, R. A., Salmon, E. D., & Endow, S. A. (1990). The *Drosophila* claret segregation protein is a minus-end directed motor molecule. *Nature*, 347(6295), 780–2.

Wang, Y.-H., Slochower, D. R., & Janmey, P. A. (2014). Counterion-mediated cluster formation by polyphosphoinositides. *Chemistry and Physics of Lipids*, 182, 38–51.

Westerholm-Parvinen, A., Vernos, I., & Serrano, L. (2000). Kinesin subfamily UNC104 contains a FHA domain: boundaries and physicochemical characterization. *FEBS Letters*, 486(3), 285–90.

Woźniak, M. J., & Allan, V. (2006). Cargo selection by specific kinesin light chain 1 isoforms. *The EMBO Journal*, 25(23), 5457–68.

Yildiz, A., Tomishige, M., Gennerich, A., & Vale, R. D. (2008). Intramolecular strain coordinates kinesin stepping behavior along microtubules. *Cell*, 134(6), 1030–41.

Yildiz, A., Tomishige, M., Vale, R. D., & Selvin, P. R. (2004). Kinesin walks hand-over-hand. *Science*, 303(5658), 676–8.

Yonekawa, Y., Akihiro, H., Yasushi, O., Takeshi, Funakoshi, Yoshimitsu, K., Yosuke, T., Sumio, T., ... Hirokawa, N. (1998). Defect in Synaptic Vesicle Precursor Transport and Neuronal Cell Death in KIF1A Motor Protein-deficient Mice. *The Journal of Cell Biology*, 141(2), 431–441.

Zahn, T. R., Angleson, J. K., MacMorris, M. A., Domke, E., Hutton, J. F., Schwartz, C., & Hutton, J. C. (2004). Dense core vesicle dynamics in *Caenorhabditis elegans* neurons and the role of kinesin UNC-104. *Traffic (Copenhagen, Denmark)*, 5(7), 544–59.

Zhou, H. M., Brust-Mascher, I., & Scholey, J. M. (2001). Direct visualization of the movement of the monomeric axonal transport motor UNC-104 along neuronal processes in living *Caenorhabditis elegans*. *The Journal of Neuroscience: The Official Journal of the Society for Neuroscience*, 21(11), 3749–55.

Zhu, H., Lee, H. Y., Tong, Y., Hong, B. S., Kim, K. P., Shen, Y., ... Park, H. W. (2012). Crystal structures of the tetratricopeptide repeat domains of Kinesin light chains: Insight into cargo recognition mechanisms. *PLoS ONE*, 7(3), 1–10.

Ziemba, B. P., & Falke, J. J. (2013). Lateral diffusion of peripheral membrane proteins on supported lipid bilayers is controlled by the additive frictional drags of (1) bound lipids and (2) protein domains penetrating into the bilayer hydrocarbon core. *Chemistry and Physics of Lipids*, 172-17

List of figures

1.1	Cytoskeletal network in eukaryotic cell	3
1.2	Structure of a microtubule	4
1.3	Kinesin superfamily, structure and phylogeny of major mammalian kinesin	8
1.4	Structure of kinesin-1 dimer	10
1.5	Structure of kinesin-3 member, KIF1A and KIF16B	12
1.6	Kinesin-1 attachment to cargo via various adaptor proteins	14
1.7	<i>In vitro</i> motility assays	18
1.8	Mechanochemical cycle of kinesin-1	20
2.1	Biotinylated SLBs formed on glass were homogenous and diffusive.....	27
2.2	Truncated rat kinesin-1 constructs with SBP tag were purified with His tag affinity chromatography.....	28
2.3	SM stepping velocity of rKin430-SBP-GFP is higher than the MT gliding velocity on surface-immobilized motors.....	30
2.4	SBP tagged kinesin-1 constructs were diffusive, when anchored to biotinylated SLBs	33
2.5	Gliding MTs do not cross each other when propelled by membrane- anchored kinesin-1	35
2.6	Ensemble average MT velocity and diffusivity on SLBs were determined by fitting their MSD as a function of time.....	38
2.7	MT gliding velocity, for membrane-anchored kinesin-1, increase with increasing motor density.	39
2.8	Theoretical model for membrane-anchored gliding predicts dependence of MT gliding velocity on motor density and motor diffusivity	41
2.9	MT gliding velocities were independent of length and MT diffusivity decreased with increasing length, for all of the motor densities.....	47
2.10	Membrane-anchored kinesin-1 motors slip backwards, while propelling a MT forward	51
2.11	Theoretical model, based on the frictional forces on microtubule and membrane-anchored motors, fits the experimental data well	53
2.12	Microtubules are propelled faster on L_o phase as compared to L_d phase, by motors bound to a phase-separated SLB.....	54

2.13	Schematic diagram of membrane-anchored motor slipping while propelling a microtubule	57
3.1	Recombinant His tag FL KIF16B is degraded in the insect cell expression system	65
3.2	Truncated KIF16B constructs were purified via His tag but FL KIF16B with His tag has low solubility	66
3.3	Recombinant FL KIF16B was purified as a dimer by fusing it with a cleavable MBP tag	70
3.4	FL KIF16B is active and moves on a microtubule with a moderate processivity	71
3.5	16B-400 and 16B-400-PX are both processive, but show different motility behavior	72
3.6	16B-429 and 16B-429-PX interact diffusively with MTs	73
3.7	FL KIF16B forms a dimer without attaching to a cargo	76
3.8	Surface-immobilized FL KIF16B and 16B-400 propel MTs at velocity lower than the SM stepping velocities	78
3.9	3% PI(3)P SLBs formed on glass were diffusive with uniformly distribution of PI(3)P	81
3.10	FL KIF16B motors anchored to PI(3)P SLBs were diffusive.	82
3.11	MT gliding velocity, for membrane-anchored KIF16B, increased with increasing motor densities	85
3.12	KIF16B motors localized to the PI(3)P vesicular cargo in vitro and exhibited long-range transport	900
3.13	Comparison of the conformational state of kinesin-3 motors, KIF16B and KIF1A	93
5.1	Schematic of flow cells used for stepping motility assays and conventional gliding motility assays	111
5.2	Reaction chambers used for the membrane-anchored gliding motility .	114
5.3	Schematic of steps involved in SLB formation	116
5.4	Background noise correction for FRAP analysis	120

List of tables

1.1 Cargo complexes transported by kinesin-1 and kinesin-3	13
3.1 Velocity and run length of FL KIF16B for different MT preparations.	75
5.1 Plasmids used in this study	103

Abbreviations and symbols

Abbreviations

a.a	Amino acids
ADP	Adenosine-5'-diphosphate
AFM	Atomic Force Microscopy
AMPPNP	Adenosine 5'-(β,γ -imido)triphosphate
APP	Amyloid precursor protein
ATP	Adenosine-5'-triphosphate
BSA	Bovine Serum Albumin
C-terminal	Carboxy-terminal
c.i.	Confidence interval
CC	Coiled coil
CRMP	Collapsin response mediator protein
ddH ₂ O	Double-distilled water
DMSO	dimethyl sulfoxide
DNA	Deoxyribonucleic acid
dNTP	Deoxynucleotide
DOPC	1,2-dioleoyl- <i>sn</i> -glycero-3-phosphocholine
DOPE	1,2-dioleoyl- <i>sn</i> -glycero-3-phosphoethanolamine
DSPE-PEG(2000)Biotin	1,2-distearoyl- <i>sn</i> -glycero-3-phosphoethanolamine-N-[biotinyl(polyethylene glycol)-2000]
DTT	Dithiothreitol
<i>E. coli</i>	<i>Escherichia coli</i>
eGFP	enhanced Green fluorescent protein
EM CCD	Electron-multiplied charge-coupled device
Fab	Antigen binding fragment
FL	Full-length
fN	Femto Newton

FYVE	Fab1/YOTB/Vac1/EEA1 homology domain
GABA	Gamma-aminobutyric acid
GDP	Guanosine 5'-diphosphate
GMP-CPP	Guanosine 5'-[α,β -methylene] triphosphate
GoI	Gene of interest
GRIP	Glutamate receptor-interacting protein
GST	Glutathione S - transferase
GTP	Guanosine-5'-triphosphate
GUVs	Giant unilamellar vesicles
HAP	Huntington associated protein
HEPES	4-(2-hydroxyethyl)-1-piperazineethanesulfonic acid
IPTG	isopropyl- β -D-thiogalactopyranosid
IS	Ionic strength
JIP	JNK-interacting protein
JNK	Jun amino-terminal kinase
kDa	Kilo Dalton
KHC	Kinesin heavy chain
KLC	Kinesin light chain
LB	Lysogeny broth or luria-Bertani broth
LCB	Lipid Coated Silica Bead
LUVs	Large unilamellar vesicles
mfGFP	Multifunctional green fluorescent protein
MLVs	Multilamellar vesicles
MSD	Mean square displacement
MT	Microtubule
N-terminal	Amino-terminal
NC	Neck coil
PCR	Polymerase chain reaction
PH	Pleckstrin homology domain
P _i	Inorganic phosphate
PI(3)P	1,2-dioleoyl- <i>sn</i> -glycero-3-phospho-(1'-myo-inositol-3'-phosphate)
PIP ₂	Phosphatidylinositol – (4,5) bis phosphate

PIPES	4-piperazine-diethanesulfonic acid
pN	Pico Newton
PX	Phox homology domain
s.d.	Standard deviation
s.e.m.	Standard error of mean
S.O.C.	Super optimal broth with catabolite repression
SBP	Streptavidin binding peptide
SDS	Sodium-dodecyl-sulfate
SF	<i>Spodoptera fugiperda</i>
SLBs	Supported lipid bilayers
SM	Single-molecule
SUVs	Small unilamellar vesicles
TBE	Tris-borate + Na ₂ EDTA
TIRF	Total internal reflection fluorescence
TPR	Tetratricopeptide repeats
TrkB	Tropomyosin receptor kinase B
UV	Ultra violet light

Symbols

D	Diffusion coefficient in $\mu\text{m}^2/\text{s}$
k_B	Boltzmann constant, $1.38 \times 10^{-23} \text{ J/K}$
η	Viscosity of a solution Pa.S
T	Temperature in Kelvin
v	Velocity in $\mu\text{m/s}$
σ	Surface density in μm^{-2}
ρ	Linear density in μm^{-1}
Δt	Acquisition time interval in ms
F	Drag force in fN
K_d	Dissociation constant

Acknowledgements

I would like to take this opportunity to extend my sincere thanks to everyone who helped me accomplish this study in some way or the other, over the past four years.

First and foremost, I wholeheartedly thank my advisor *Prof. Dr. Stefan Diez*, who accepted my candidature to pursue doctoral thesis in his wonderful lab. His constant encouragement, support and positive attitude were a major source of inspiration through out the project. He has been a great mentor, the most polite critic and a very friendly person. It was a great experience to work with and learn from him. Furthermore, I would like to thank my thesis advisory committee members *Prof. Dr. Frank Jülicher* and *Prof. Dr. Ralf Seidel* for the valuable inputs and the constructive criticism they provided for the project.

I would like to specially mention a few people without whose support the project would not have reached the stage of thesis: *Corina Bräuer* for taking such good care of the daily lab requirements. *Wim Walter* for preparing the kinesin-1 constructs. *Aliona Bogdanova* for teaching me molecular biology techniques and developing a great plasmid toolbox which works like a charm. *Grzegorz Chwastek* for teaching me how to handle lipids. Everyone at the amazing protein purification facility of MPI-CBG - *David Drechsel*, and *Barbara Borgonovo*, for the insightful tips regarding protein purification and helping out with chromatography. *Regis Lemaitre* for making all the viruses used in the study. *Regina Wegner* for providing SF cells even at short notice. DNA sequencing facility of MPI-CBG, for promptly handling all the sequencing requests. *Janine Fischer* for developing the theoretical model. *Tim Rehfeldt* for working with me on KIF16B and for being my first mentee. *Friedrich Schwarz* who developed a fantastic MATLAB code for analyzing the tricky gliding data and teaching me the power of MSD analysis. *Felix Ruhnnow* the programming genius of the lab, for developing coolest tracking software FIESTA, without which the thesis would have taken much longer to complete. *Marcus Braun* and *Zdenek Lansky* for the

fruitful discussions and making me believe that the project would work. Also, Marcus for proofreading and commenting on the manuscript of thesis and making me remove at least fifty 'also' in this dissertation.

Throughout these years I have been fortunate to have a great bunch of fellow lab-mates, who were always friendly and helpful, making our lab one of the best places to work. First, I would like to thank the wise people of the lab *Till Korten* and *Cordula Reuther* for sharing their wisdom ranging from where things are to how things work in the lab. Second, I wish to thank the not so wise people *Juliane Beyer*, *Lara Scharrel*, *Annemarie Lüdecke*, *Samata Chaudhuri* and *Aniruddha Mitra* (God) for always being so helpful, caring and cheerful. I will always cherish the countless fun sessions with you guys at lunch breaks, coffee breaks and lab get together, which always ran until wee hours. I would like to thank some of the past members of the lab from whom I have learned a lot and shared many fun moments *René Schneider*, *Viktor Schroeder*, *Bert Nietzsche*, *Agata Szuba*, *Verena Puttrich*, *Marta Urbanska*, and *Emiliya Poghosyan*.

I would like to express my gratitude to *Carolyn Fritzsche* at the international office at MPI-CBG, who is an angel to all the expats working here, and *Barbara Lindemann* for taking care of all the administrative and bureaucratic stuff so that we can concentrate on science.

A very special thanks to my awesome wife *Neha Berlia*, to whom I am forever indebted and without whose immense love, unyielding support and continued patience I would not have been able to reach this stage.

Finally and most importantly, I would like to thank my family, relatives and friends who were always there for me when I needed them. My heartfelt thanks to my father *Sri O. P. Grover* and my mother *Smt. Shanta Grover* who always believed in me and encouraged me to pursue what I wanted. My brother *Hardik Grover* for his concern and support.